TÉCNICO LISBOA

Inverse Dynamics of a Swimmer Multibody Model: An Analysis of the Upper Limbs During Front Crawl

Francisca Tito de Carvalho Simões

Thesis to obtain the Master of Science Degree in

Mechanical Engineering

Supervisors: Prof. Jorge Alberto Cadete Ambrósio

Prof. João Paulo Villas-Boas Soares Campos

Examination Committee

Chairperson: Prof. Paulo Rui Alves Fernandes

Supervisor: Prof. João Paulo Villas-Boas Soares Campos

Member of the Committee: Prof. Carlos Miguel Fernandes Quental

October 2021

Acknowledgements

Aos Professores Carlos Quental, João Paulo Vilas-Boas e Jorge Ambrósio. Por uma orientação científica coordenada que foi para além disso, acabando por ser uma Escola de Pensamento. Ao Professor Carlos Quental, pela compreensão, acompanhamento e sensibilidade. Por saber sempre se percebemos ou não uma explicação, por não nos entregar a solução, questionando-nos até chegarmos às nossas respostas. Pelo seu olho clínico e rigor intelectual. Ao Professor João Paulo, pelas portas que me foi abrindo no mundo da biomecânica da natação. Pela sua curiosidade intelectual e por me mostrar a importância de perguntar sempre, com vista a ir mais rápido, mais alto, mais forte. Ao Professor Jorge Ambrósio, pelos seus ensinamentos que em muito transbordaram o âmbito da biomecânica. Por constantemente alertar para a importância de não me esquecer porque é que comecei; pelo seu pragmatismo e capacidade de filtrar o essencial; por extravasar para nós, alunos, a sua mundividência, que tanto nos enriquece.

À Mariana, que acompanhou esta tese desde o seu início e que, mesmo depois de terminar a dela, continuou a ser um pilar. Pelas conversas e por tudo o que fomos partilhando durante os meses mais críticos do último ano e meio. Aos amigos com quem partilhei a jornada e que foram fundamentais para sobreviver ao Técnico: a Alda, a Xana, o Miguel, a Pimentinha, o Cuco, o Guilherme, o Tomás, a Constança e o Rafa.

À Professora Raquel Aires Barros, pela sua visão e exemplo de liderança. Pela sua capacidade em identificar o talento de cada pessoa e em conjugar tudo no melhor produto final possível. Por acreditar que são as pessoas que trazem a mudança. Ao Professor António Rodrigues, pela sua generosidade e sensibilidade no contacto com os alunos. Pelas conversas estimulantes que tivemos e que foram desde Ovídio a cinema alemão dos anos 20. A ambos, pela dedicação à Escola, e por terem sido figuras absolutamente tutelares durante a minha passagem pelo Conselho Pedagógico. Aos meus colegas do Órgãos de Escola, em particular ao Pedro, à Margarida, ao Alexandre e ao Gonçalo, por todas as horas passadas em esplanadas do Técnico e em gabinetes do Pavilhão Central em debates estimulantes a discutir o novo modelo de Ensino e tantos outros assuntos académicos. Obrigada por me mostrarem o que significa ter um verdadeiro sentido de missão.

Ao NFI: Alice, Ana Lúcia e Joana, autênticos exemplos de força, inteligência e sensibilidade; por se mostrarem a inspiração para as coisas importantes dos nossos dias e que a Adília sintetizou: ler, escrever, ouvir música, andar a pé, brincar.

Aos meus pais, pelo apoio constante e por me permitirem ir trilhando o meu caminho; por nos terem educado, a mim e ao meu irmão, num espaço de liberdade, pensamento crítico e diálogo com o outro. Ao meu irmão, por ser o amigo mais antigo, e o mais fiel.

Ao João, por ser o meu maior conselheiro e motivador. Por me escutar e não me deixar cair nunca. Por me desafiar sempre, com amor e paciência infinitos.

Abstract

The aim of this study is to propose a full-body skeletal model of the human body including a detailed representation of the shoulder complex for the biomechanical analysis and assessment of swimming activities. Considering multibody dynamics, a three-dimensional biomechanical model using Cartesian coordinates is proposed. The anatomical articulations are approximated by ideal kinematic joints, which are controlled by rotational driver actuators.

Kinematic data were collected at the LABIOMEP-UP for a male swimmer performing a six-beat front crawl swimming technique and the shoulder rhythm was estimated using state of the art regression equations. External forces describing the interaction between the human body and the surrounding environment were estimated using a computer simulation method available in the literature. A determinate inverse dynamic analysis is performed considering the full body biomechanical model actuated upon by driver actuators to evaluate the joint torques and intersegmental joint forces acting on the upper extremity, particularly on the glenohumeral, sternoclavicular and acromioclavicular joints.

The results of the determinate problem are presented and discussed for the anatomical joints of the human upper limbs. The intersegmental forces and joint torques were evaluated for a left-stroke cycle, presenting higher absolute peaks in the most propulsive stages, the insweep and upsweep. The results obtained with a detailed model of the shoulder, considering the clavicle and the scapula, were also compared with a classic model of the shoulder, in which the shoulder joint was modelled as a simple ball-and-socket joint connecting the humerus to the thorax. Overall, the results of the intersegmental forces and joint torques have little or no effect of this increased level of shoulder discretization.

Keywords: Multibody dynamics, Front Crawl Swimming, Hydrodynamic forces, Shoulder complex

Resumo

O objectivo do presente trabalho é propor um modelo completo do corpo humano, incluindo uma representação detalhada do complexo do ombro, para análise e avaliação de um movimento de natação. O modelo biomecânico tridimensional proposto utiliza coordenadas cartesianas e é baseado numa abordagem de dinâmica de sistemas multicorpo. As articulações do corpo humano são modeladas enquanto juntas cinemáticas ideais e são controladas por actuadores de junta.

A aquisição de dados cinemáticos da natação de estilo crawl foi feita no LABIOMEP-UP para um nadador do sexo masculino e o ritmo do ombro foi estimado de acordo com equações preditivas disponíveis na literatura. As forças hidrodinâmicas que actuam sobre o corpo do nadador foram calculadas através da utilização de um programa computacional de simulação. Após obtenção de uma cinemática consistente e posterior aplicação das forças externas, uma análise dinâmica inversa é conduzida considerando que as articulações do modelo biomecânico são accionadas por actuadores de junta. Os momentos articulares e forças intersegmentares são analisados e avaliados para o membro superior, em particular nas articulações da glenohumeral, esternoclavicular e acromioclavicular.

Os resultados do problema de dinâmica inversa determinista são apresentados e discutidos para um ciclo esquerdo de natação, apresentando globalmente picos com valor absoluto mais elevado nas etapas mais propulsivas do ciclo, insweep e upsweep. Os resultados obtidos utilizando um modelo detalhado do ombro, incluindo clavícula e omoplata, foram também comparados com um modelo clássico do ombro, que modela esta articulação como uma junta esférica simples que liga o úmero ao tórax. Globalmente, as forças intersegmentares e os momentos articulares demostram pouca a nenhuma diferença entre os modelos com diferentes níveis de discretização.

Palavras-chave: Dinâmica de sistemas multicorpo, Natação de Estilos Livres, Forças Hidrodinâmicas, Complexo do Ombro

Table of contents

List of Figures

List of Tables

Abbreviations

AC	Most dorsal point on the acromioclavicular joint
APW	Anterior pelvic width
ARP	Anatomical reference position
ASIS	Anterior superior iliac spine
BSIP	Body segment inertial parameter
C7	Processus Spinosus of the 7th cervical vertebrae
CFD	Computational Fluid Dynamics
CJC	Cervical joint centre
COM	Centre of mass
DOF	Degrees of freedom
FD	Finite Differences
FEM	Finite Element Method
GUI	Graphical User Interface
HJC	Hip joint centre
ISB	International Society of Biomechanics
LABIOMEP-UP	Porto Biomechanics Laboratory (University of Porto)
LHBM	Lisbon Human Body Model
LJC	Lumbar joint centre
LL	Leg length
MA	Tip of the medial malleolus
MK	Medial epicondyle of the femur
OJC	Atlanto-occipital joint centre
PD	Pelvic depth
PSIS	Posterior superior iliac spine
SJC	Shoulder joint centre
SPH	Smoothed-Particle Hydrodynamics
ST1	Sternum cluster marker 1
SWUM	Swimming Human Model
Swumsuit	Swimming Human Model with Synthetic User Interface Tools

Symbols

Convention

a, A, α	Scalar
$\mathbf{a}$	Vector
$\mathbf{A}$	Matrix

Over script

$\dot{\mathbf{a}}$	First time derivative
$\ddot{\mathbf{a}}$	Second time derivative
$\tilde{\mathbf{a}}$	3×3 skew-symmetric matrix

Superscript

$\mathbf{a}^{\mathrm{T}}, \mathbf{A}^{\mathrm{T}}$	Transpose of a vector or matrix
$\mathbf{a}'$	Quantity expressed in the body-fixed (or local) reference frame

Latin Symbols

$\mathbf{A}_i$	Rotation matrix for body *i*
C_a	Added mass coefficient
C_D	Drag coefficient
C_L	Lift coefficient
C_m	Inertial coefficient
$\mathbf{G}_i$	3×4 global transformation matrix for body *i*
$\mathbf{I}$	Identity matrix
$\mathbf{L}_i$	3×4 local transformation matrix for body *i*
$\mathbf{M}$	Mass matrix for a system
$\mathbf{q}, \dot{\mathbf{q}}, \ddot{\mathbf{q}}$	Vector of generalised coordinates, velocities, and accelerations
X, Y, Z	Global Cartesian coordinates (LHBM)
x, y, z	Absolute coordinate system (SWUM)
x_b, y_b, z_b	Body coordinate system (SWUM)

Greek Symbols

$\boldsymbol{\gamma}$	Right-hand side vector of the acceleration constraint equations
$\boldsymbol{\lambda}$	Vector of Lagrange multipliers

$\boldsymbol{\nu}$	Right-hand side vector of the velocity constraint equations
ρ	Density of the fluid
$\boldsymbol{\Phi}$	Generalised vector of constraints
$\boldsymbol{\Phi}_{\mathbf{q}}$	Jacobian matrix of the constraints
$\boldsymbol{\omega}$	Angular velocity vector
$\dot{\boldsymbol{\omega}}$	Angular acceleration vector
ξ, η, ζ	Body-fixed (or local) coordinates (LHBM)

1. Introduction

1.1. Motivation and Objectives

Sports Biomechanics is defined by Bartlett (2007) as the study, analysis and assessment of human movement patterns in sport with the purpose of enhancing the athletes' performance and decreasing the risk of injuries. From this point of view, competitive swimming evaluation poses a number of challenges. The fact that the swimming motion occurs in an aquatic environment makes this study intrinsically multidisciplinary (Barbosa et al., 2011), inheriting the shortcomings in experimental kinematic and kinetic data acquisition in the water, required to build biomechanical models, necessary to assess the behaviour of the human body.

In the context of swimming motion, current biomechanical models are largely oversimplified, and often cover a specific region of the human body (Cohen et al., 2015; Lauer et al., 2016). Experimental methods also limit the evaluation of the internal forces in the human body since they provide the external forces acting on the human body during swimming with insufficient accuracy due to to the restrictions of measuring devices (Sato & Hino, 2013).

During the front crawl swimming motion, the upper body plays a significant role in thrusting, accounting for almost 85% – 90% of total propulsive activity of the swimmer (Guignard et al., 2019; Toussaint & Beek, 1992). However, all biomechanical models applied for swimming activities to the present date neglect the shoulder girdle, probably limited by the experimental protocols an aquatic environment, which limits their ability to simulate and study the complex shoulder mechanism. The wide range of motion required to perform the front crawl swimming technique is a result of the coordinated interplay between all components of the shoulder complex, including the sternoclavicular, acromioclavicular, glenohumeral and scapulothoracic joints, all of which are critical for an accurate description of the shoulder biomechanics.

This study proposes a three-dimensional full-body skeletal model of the human body with a detailed representation of the shoulder, based on Quental et al. (2012) to address the shortcomings of current biomechanical models for swimming activities, namely in the evaluation of the internal forces of the upper limbs through inverse dynamics. The shoulder rhythm was estimated using regression equations proposed by Xu et al. (2014) and the external forces acting on the human body during swimming, herein referred to as hydrodynamic forces, were determined using a simulation software available in the literature, the Swimming Human Model with Synthetic User Interface Tools (Swumsuit) (Nakashima et al., 2007).

1.2. State of the Art

Biomechanics is the field of science that describes, analyses and assesses human motion considering the laws of physics and engineering concept (Nordin & Frankel, 2013; Winter, 2009). Whereas some aspects of the human movement evaluation can be measured experimentally, such as body kinematics, ground reaction forces or muscle activity, others, such as joint contact forces, cannot (Rajagopal et al.,

2016). Biomechanical models provide a non-invasive alternative to determine these quantities. To realistically predict the behaviour of the human body during motion, these models should mirror biological and physical principles that favour and constrain movement. Together with the growing computational power, these models are getting increasingly complex and accurate, leading to considerable breakthroughs over the last decades. Several fields took advantage from this evolution, including medical rehabilitation, ergonomics and sport science, but much work remains to be done regarding motion optimization, performance enhancement or injury prevention (Xiao & Fu, 2016).

1.2.1. Multibody Biomechanical Modelling

Simulating the human motion using computational tools requires mathematical models to accurately reproduce the biomechanical system and its interactions with the surrounding environment. Modelling skeletal systems using a multibody dynamics approach has been shown to be effective, providing quality results without compromising computational efficiency. The level of anatomical discretization in the biomechanical model, as well as the mathematical formulation used depend on many factors such as the application, object of analysis or even the field of research (Silva, 2003). Accordingly, biomechanical models can focus on a single body region, such as the Twente Lower Extremity Model (Klein Horsman et al., 2007) or the Lisbon Shoulder Model (Quental et al., 2012), or on the entire body (Rajagopal et al., 2016; Silva & Ambrósio, 2003).

In a multibody model, each anatomical segment is assumed to behave like a rigid body with known mass and inertia, and each joint is characterized according to its type (related with the way it constrains the mechanical system) and location. These data are more important than the body's geometries, which are only relevant if contact detection is required. Intersegmental joint reaction forces can be determined either by a forward or an inverse dynamic analysis and provide valuable information about the mechanical interaction of each anatomical segment. The difference between these two types of analyses is that the inverse dynamics problem determines internal forces and joint torques from known movements and external forces, whereas the forward dynamics reconstructs motion from known applied forces and torques (Otten, 2003). The inverse dynamics requires a lot less computational power and is commonly adopted if the aim of the analysis is exclusively to calculate joint reaction forces and joint torques (Silva, 2003), which suits the purpose of the current work.

Although the upper limbs are required for all sorts of activities of the everyday life, biomechanical models of the upper extremities are still in an early stage of development (Quental et al., 2012). The majority of tasks performed by the human shoulder rely on its perfect symbiose between mobility and stability (Veeger & van der Helm, 2007). In fact, the shoulder girdle is highly complex in terms of the movement pattern, forming a closed-loop system (a chain in which every link in the system is connected to any other link by at least two distinct paths) that drives shoulder kinematics. To describe this motion accurately, several biomechanical models with different degrees of complexity have been proposed in the literature over the last decades.

According to Yang et al. (2010), Dempster (1965) was the first author to propose a physical model of the shoulder mechanism, introducing the concept of linkages to explain the relative motions of the

clavicle, scapula and humerus. Almost thirteen years later, a qualitative model for the shoulder in elevation was suggested by Dvir & Berme (1978). This approach contemplated two interconnected mechanisms and aimed to assess the loads transmitted by the glenohumeral joint, discussing its stability and mobility.

Later, and also based on the previously mentioned linkage mechanism, Engin & Chen (1986a,1986b) and Engin & Tümer (1989) introduced and worked on the concept of the joint sinus cone, which is a conical surface that envelopes the total range of angular motion permitted by a moving member of a joint when the other member is rigidly fixed, centred at the functional joint centre. In these new biomechanical approaches, articulations were assumed to behave as ideal mechanical joints and were constrained by the cones of motion.

Shortly after, the Göteborg Shoulder Model was presented by Högfors et al. (1987, 1991). This model represented the shoulder complex as a system of three rigid bodies, interconnected by spherical joints, with a total of twelve degrees of freedom. External loads were predicted in static or quasi-static situations without considering the effects of inertia and its redistribution during the movement.

The Delft Elbow and Shoulder Model (van der Helm, 1994, 1997) arrived as a substantial improvement to the shoulder modelling universe, presenting the most comprehensive alternative until then. This model used a Finite Element approach that could perform both inverse and forward dynamic analyses. Bones were modelled as rigid segments and were linked to one another through spherical joints; the scapula was assumed to slide over the thorax surface, modelled as an ellipsoid.

Most recent models appeared on the XXI century, namely the shoulder model inbuilt in the AnyBody software (Lindsay, 2001), based on the Dutch shoulder model, and the models in the Simtk OpenSim (Holzbaur et al., 2005; Seth et al., 2019); the Newcastle shoulder model (Charlton & Johnson, 2006), consisting of six rigid bony segments interconnected by three ball-and-socket joints – the sternoclavicular, acromioclavicular and glenohumeral joints – two hinge joints at the elbow and a pair of prismatic joints to model the sliding behaviour of the scapula over the thorax.

Quental et al. (2012) also proposed a robust musculoskeletal model alternative, the Lisbon Shoulder Model (LSM). This biomechanical model is defined by seven rigid bodies, with the sternoclavicular, acromioclavicular and glenohumeral articulations being represented as spherical joints, the humeroulnar and radioulnar articulations represented as hinge joints and the scapulothoracic joint modelled has two holonomic constraints (Quental et al., 2012). An adapted version of this model will be implemented to fulfil the purpose of this dissertation.

1.2.2. Swimming Analysis

Competitive swimming has changed drastically since 1896, the year it was first introduced as a sport in the Olympic Games. Until 1912, only male swimmers were allowed to compete in the Olympics. Women were only able to participate since the Stockholm Olympics, and even then, they only had the chance to prove themselves in the 100 m freestyle and 4 x 100 m freestyle relay. Nowadays, swimming is still

one of the most record-breaking sports, with the longest-standing world record in any swimming discipline hardly being more than 10 years old (Silver, 2012).

In swimming activities, performance enhancement can be analysed, at least, within a physiological, biomechanical and fluid dynamics framework. The success of a swimmer is based on several inter-related factors, making it a very complex and challenging field of study for researchers (Barbosa et al., 2011). To realistically analyse and understand the swimming motion, active drag forces, effective propulsive forces, propelling efficiency and power output should be considered (Toussaint & Beek, 1992). These aspects, highly influenced by factors such as the swimming technique, body position, breathing pattern, wall turns and finger spacing, are key to optimize the swimming stroke. Nonetheless, these are very difficult to measure experimentally and in a non-invasive way (Cohen et al., 2010; Lauer et al., 2016)

Asides from the motion capture difficulties in an aquatic environment, modelling the front crawl swimming technique has some particular challenges, for instance, the sudden and high deformations of the swimmer body shape, the complex fluid problem (Cohen et al., 2020) and the asymmetric behaviour of the right and left sides of the human body, either due to the inherently out of phase stroke movement or by the uneven breathing patterns (Psycharakis & Sanders, 2008). Consequently, most studies in the biomechanics of swimming have focused on a single region of the human body (Cohen et al., 2015; J. Lauer et al., 2016).

Over the last decades, computational fluid dynamics (CFD) has offered a consistent way to answer these problems, providing a way of solving the Navier-Stokes fluid flow field. This type of numerical simulation has the advantage of dealing well with the large water displacements, deformable bodies and transient and complex movements (Takagi et al., 2016). However, its low computational efficiency makes it more useful to assess small body regions. The first known CFD approach applied to the swimming context was conducted in a delimited body zone with fixed bodies and under steady-state conditions (Bixler & Riewald, 2002). Other studies followed using CFD: Von Loebbecke et al. (2009) proposed an unsteady computational fluid dynamics approach to simulate and inspect the hydrodynamics of the dolphin kick; Keys (2010) made an extensive investigation on several swimming movements, namely the dolphin kick in front crawl, breaststroke and underwater plus a simulation of the complete freestyle stroke considering a superficial full body model obtained via a complete body scan. Marinho et al. (2011) also used the CFD approach to analyse the hydrodynamic characteristics of a realistic model of an elite swimmer hand and forearm. Later, Lauer et al. (2016) and Samson et al. (2017) analysed the role of the upper limbs in the context of the swimming motion: the first studied the joint forces and moments induced by underwater sculling movements, integrating the use of CFD and inverse dynamics; the second evaluated the propulsive forces generated by the hand and the forearm, relating them with hand kinematic parameters.

Lately, a new trend has been identified in the swimming analysis. Smoothed particle hydrodynamics (SPH), a computational meshless and particle-based methodology, has demonstrated strong advantages over grid-based approaches: they robustly handle large deformations and have the ability to solve complex fluid free surfaces. Topological fluctuations on the media do not affect the solution

speed or stability, with events like splashing or refractions on the pool surface having close to zero impact in results (Cleary et al., 2013; Cohen et al., 2009; Cohen et al., 2015).

Unfortunatelly, both CFD and SPH have proven to be unsuitable for studies involving large scale parameters due to their computational cost (Takagi et al., 2016). To answer this struggle, an analytical alternative to these time consuming methods was proposed by Nakashima et al. (2007). The open source Swumsuit simulation software estimates the hydrodynamic forces without solving the flow field and considering unsteady effects. Besides solving several swimming techniques and other aquatic activities such as lifting motions in artistic swimming or even shooting in water polo, it provides its user the possibility of manipulating several swimming parameters to improve perfomance while offering real time visualization. Considering these benefits, the present work uses the Swumsuit interface proposed by Sequeira (2021) to compute hydrodynamic forces, essential for an inverse dynamic analysis.

1.3. Application Case: The Role of the Upper Limb in Front Crawl

Swimmers perform complex and cyclical movements. The front crawl technique, the most common swimming stroke (Cohen et al., 2015), requires a tremendous level of coordination between upper and lower extremities, conciliating the alternating motion of the upper limbs above and below the water surface with the interchanging lower limb pendular movement (Guignard et al., 2019). Additionally, the swimming breathing patterns influence the fluid resistance acting on the body, directly affecting the swimmer’s performance (Toussaint & Beek, 1992).

The body anthropometry also influences performance. From a physioanatomical point of view, successful athletes are predominantly lean and tall, with elongated limbs and wide shoulders, with relatively high muscular mass, especially in middle and upper bodies, and excellent aerobic and anaerobic capacity (Rejman et al., 2018; Troup, 1999). To reach an elite level, these professional swimmers swim up to 80.000 meters per week, which is equivalent to approximately 30.000 strokes per arm (Matzkin et al., 2016). Additionally, and regardless of the swimmer's technique specialty, 80% of practice time is spent performing the front crawl stroke (Beach et al., 1992). The demanding training of these athletes, together with the repetitive nature of the front crawl stroke, places enormous stress in the glenohumeral joint (Heinlein & Cosgarea, 2010), increasing the risk of a shoulder injury (Thielbar, 2020).

During the swimming motion, the upper extremity plays a determinant role in thrusting, accounting for almost 85% - 90% of total body propulsion (Guignard et al., 2019; Pink & Tibone, 2000). In fact, much of the forward propulsion created during the pull-through phase of the front crawl results from the lift forces generated by the motion of the upper limb, namely the hand and forearm (Richardson, 1986). The wide mobility and flexibility of the shoulder provides a major advantage to enhance performance since an increased range of motion allows for a greater stroke length, which is directly linked to higher swimming speeds (Chollet et al., 1997).

To partially evaluate the role of the upper limb in the context of swimming, several studies focusing on this extremity have been conducted over the years (Cohen et al., 2015; Gonjo et al., 2016; Harrison et

al., 2014; Sanders & Psycharakis, 2009; Serenza et al., 2018), but none of them contemplated a full body model with a detailed representation of the shoulder girdle. The current dissertation aims to fill that gap by presenting an open-chain shoulder model to analyse the intersegmental forces and joint moments on the human upper body.

1.4. Novel Aspects of the Work

The current work presents a full body biomechanical model for the analysis of the human swimming motion during a front crawl swimming stroke. The proposed model advances the computational modelling of the upper extremity in swimming activities by including a detailed shoulder model, composed of the clavicle, scapula, and humerus, for a more realistic simulation of the shoulder motion in an aquatic environment. To surpass the shortcomings of the kinematic and kinetic acquisitions in water settings, an integrated approach is suggested considering the shoulder rhythm predictive equations developed by Xu et al. (2014), kinematic data processing, and subsequential estimation of the hydrodynamic forces using the simulation software Swumsuit (Nakashima et al., 2007). Jointly with the determinate inverse dynamics problem, these aspects contribute to a more comprehensive and close to reality biomechanical model for swimmers.

1.5. Thesis Outline

The current work is structured in seven main chapters. Chapter 1 states the aims and motivation behind this dissertation and revises current developments in biomechanical modelling, especially those concerning the shoulder complex, and in biomechanical modelling studies conducted to date in the context of swimming. Chapter 2 briefly introduces some key concepts related to the anatomy and physiology of the upper limb with the purpose of better understanding its behaviour in the aquatic environment. Chapter 3 makes a concise overview on the methods behind the multibody dynamics approach. Chapter 4 describes the topology of the full-body biomechanical model discriminating all the necessary anthropometry data required for the development of the biomechanical model of the human subject under analysis. Chapter 5 describes the experimental data collection process; the motion reconstruction process, including the prediction of the shoulder rhythm following the regression equations of Xu et al. (2014); and the hydrodynamic forces estimation using the simulation software Swumsuit developed by Nakashima et al. (2007), including the improvement of the joint motion reconstruction procedure. Chapter 6 addresses the determinate inverse dynamic analysis of the swimming motion using driving joint actuators. Focusing particularly on the upper limb, the obtained results are compared with the literature and with a simplified model of the shoulder girdle. Results regarding the intersegmental forces and joint torques obtained for the upper body are discussed here. Finally, Chapter 7 pinpoints the major developments of the current work and identifies its limitations, suggesting future improvements regarding biomechanical modelling and swimming analysis.

2. Anatomy and Physiology of the Upper Limb

The human body is a highly complex mechanism with different functional units, one of them being the upper body - which comprehends four major sections, from proximal to distal: the shoulder, the arm, the forearm, and the hand. The shoulder is the segment overlapping part of the trunk and the lower lateral neck. The arm is the segment connecting the shoulder and elbow joints, including the anterior and posterior regions of the arm, centred around the humerus bony segment. The forearm links the elbow and wrist joints and consists of the anterior and posterior parts of the forearm, wrapping around the radius and ulna bones. Finally, the hand is the extremity of the upper limb and is located distally to the forearm. It is formed by the carpi, metacarpi and phalanges (Moore et al., 2010).

The front crawl swimming technique is greatly influenced by the motion of the upper limb, that contributes largely to the total body propulsion (Guignard et al., 2019). The present Section will address the anatomy and physiology of the upper limb to better understand the role of this extremity in the considered motion.

2.1. The Shoulder Complex

The shoulder complex enables a wide range of motion to the upper limb, clearly exceeding that of any other joint mechanism in the human body (Peat, 1986). It is the most determinant and intricate apparatus in the human body, being capable of complex kinematics (Terrier et al., 2010), and is constituted by four skeletal segments – thorax, clavicle, scapula, humerus – all interconnected by three anatomical joints – sternoclavicular (SC), acromioclavicular (AC) and glenohumeral (GH) (Hamill & Knutzen, 2013). A fourth pseudo-joint is often mentioned in the literature, the scapulothoracic joint, describing the interaction between the thorax and the scapula, even though there is no true connection between them. Because this joint was disregarded in this study, it is neglected hereafter.

2.1.1. Skeletal System

For a better understanding of the functional role of the shoulder complex, a brief definition of its anatomical constitution is presented in the following Subsections.

2.1.1.1. Thorax

The thorax, which can be seen in Figure 2-1, is a cage aimed to contain and protect the principal respiratory and circulatory organs. It is constituted by twelve pairs of ribs, including costal cartilages, which connect anteriorly to the sternum and posteriorly to twelve thoracic vertebrae and corresponding intervertebral discs.

2.1.1.2. Clavicle

The clavicle, or the collar bone, is an elongated bone that connects the upper limb to the trunk. Horizontally placed, this bony segment presents itself medially articulated with the manubrium at the SC joint and, laterally, with the acromion of the scapula at the AC joint. The curvature of the clavicle – the first two thirds of its shaft are convex, while the last third is slightly flat and concave, making it to look

like an “S” – has an important role in the resilience of this bone, helping it to support part of the upper limb’s weight. This rigid structure is movable and allows the scapula to move on the thoracic wall, increasing the range of motion of the extremity (Hamill & Knutzen, 2013; Moore et al., 2010). Figure 2-2 illustrates the posterior and anterior clavicle views:

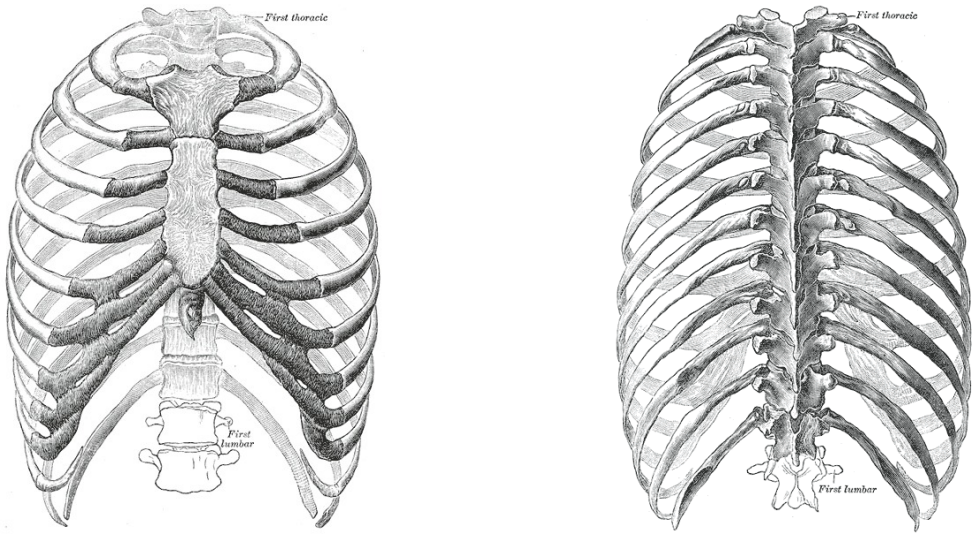

(a) (b)

Figure 2-1: Anterior (a) and posterior (b) views of the thorax (Gray & Lewis, 1918)

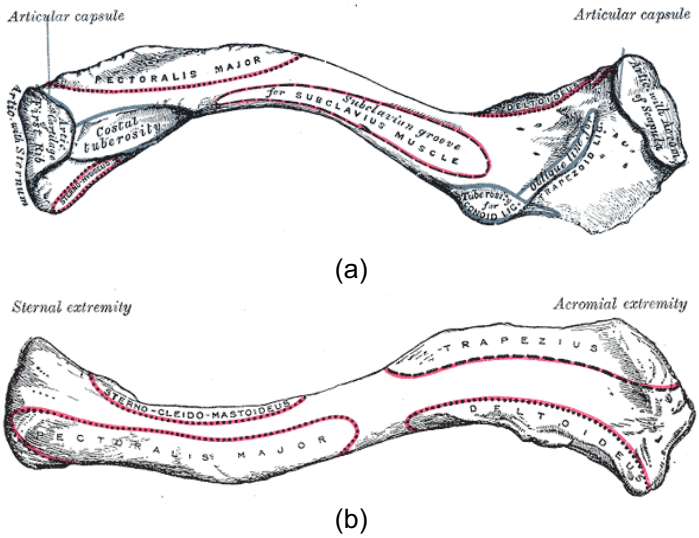

(a)

(b)

Figure 2-2: Anterior (a) and posterior (b) views of the left clavicle (Gray & Lewis, 1918)

2.1.1.3. Scapula

The scapula, or shoulder blade, is a triangular flat bone positioned on the surface of the posterolateral side of the thorax. The lateral extension of the scapula permits the interface with the clavicle, forming the AC joint. The lateral surface of the scapula includes also the glenoid cavity (see Figure 2-3), which is a shallow and concave cavity that accommodates the head of the humerus. This articulation is called the glenohumeral joint (GH) and operates just below the AC joint. The shoulder blade also describes a

movement over the thoracic wall, which despite not being a classic bone-to-bone joint, it is considered a physiological joint called scapulothoracic joint (ST). The scapula bone is depicted in Figure 2-3:

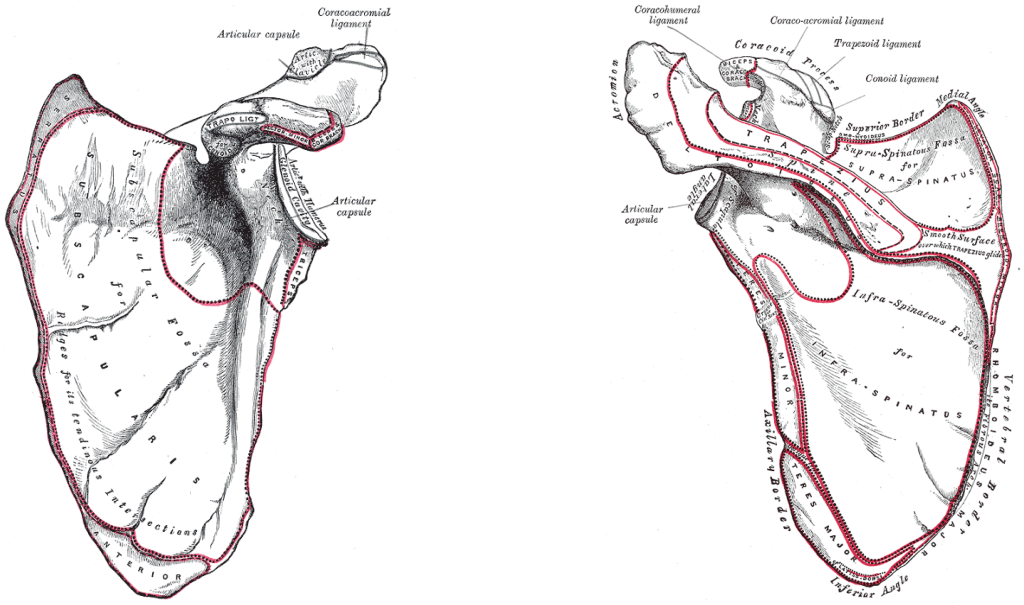

(a) (b)

Figure 2-3: Anterior (a) and posterior (b) views of the surface of the left scapula (Gray & Lewis, 1918)

2.1.1.4. Humerus

The humerus is the longest bone of the upper limb. The humerus head connects proximally with the scapula, forming the GH joint. The distal end of this segment articulates with both the ulna and the radius bones, constituting the elbow joint, considered a compound joint because it includes the connection between the humerus and the ulna (humeroulnar joint, HU) and the humerus and the radius (humeroradial joint, RU). The anterior and posterior views of the left humerus are presented in Figure 2-4.

2.1.2. Articular System

From a structural perspective, human body articulations can be classified into synovial, cartilaginous, or fibrous joints. The synovial joint is the most frequent type, allowing a wide range of motion, connecting limbs through an existent joint cavity and allowing a wide range of motion. The interconnected bones do not interface directly, having a hyaline cartilage medium between themselves. Most of the upper limb articulations are synovial joints. The cartilaginous joints, in which bones are linked by hyaline cartilage or fibrocartilage, concede very little or no motion at all. Fibrous joints result from the connection of bones by a connective tissue rich in collagen. They have almost no movement (Quental, 2013a).

Synovial joints, the predominant type when it comes to the upper extremity, can be classified according to the arrangement of the articular surfaces and the types of movement they allow. According to Hamill & Knutzen (2013), six types of synovial joints can be identified:

- **Plane or gliding joint:** The movement is nonaxial because the two opposed surfaces are almost flat, leading them to slide over each other (Hamill & Knutzen, 2013; Snell, 2012)
- **Hinge joint:** The movement is described in one plane only, allowing only the angular motion of flexion/extension. The knee joint is an example of this type of articulation (Lippert, 2006; Snell, 2012).
- **Pivot joint:** Uniaxial joint that revolves around its own longitudinal axis. It has a central bony pivot surrounded by a bony ligamentous ring (Lippert, 2006; Snell, 2012)
- **Condyloid joint**: It is a biaxial joint, allowing movement in two different planes (flexion/extension, abduction/adduction) (Lippert, 2006).
- **Saddle joint**: Biaxial joint where the articular surfaces are reciprocally concavo-convex, permitting flexion/extension, abduction/adduction and small rotation movements (Lippert, 2006; Snell, 2012).
- **Ball-and-socket joint**: In this type of joint, a ball-shaped head of one bone fits into a spherical shaped cavity of another bone. This configuration allows three rotational movements, allowing flexion/extension about the frontal axis, abduction/adduction about the sagittal axis, and axial rotation about the vertical axis. The hip and GH joints are good examples of ball-and-socket joints (Lippert, 2006; Snell, 2012).

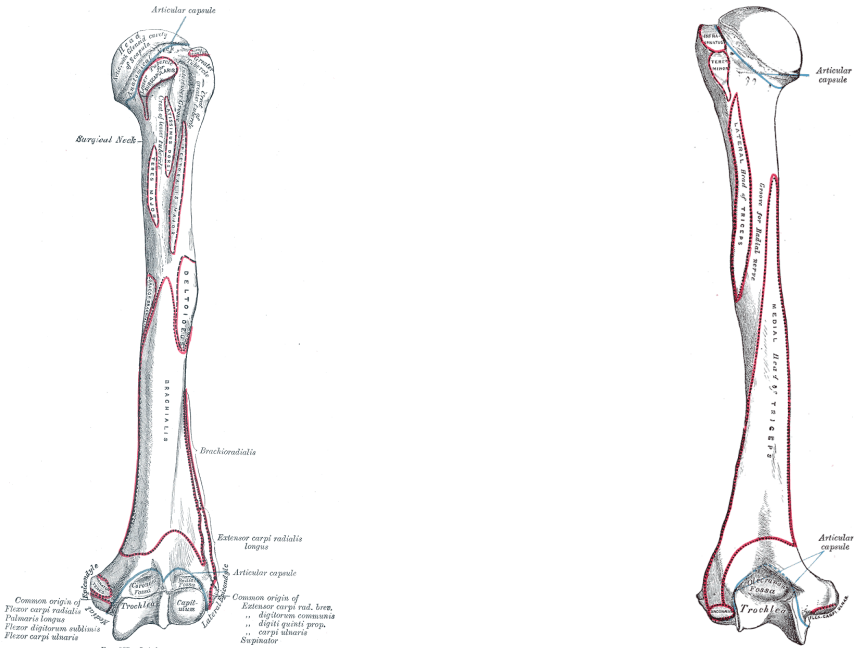

(a) (b)

Figure 2-4: Anterior (a) and posterior (b) views of the left humerus (Gray & Lewis, 1918)

The intricate articular system of the shoulder complex is a result of four interconnected joints: SC, AC, GH, and ST. All of them are briefly described in the following Subsections, except for the ST joint, which was not taken into consideration in this work.

2.1.2.1. Sternoclavicular Joint

The sternoclavicular joint is a saddle type synovial joint functioning as a ball-and-socket joint. Linking the sternal end of the clavicle and the manubrium and the first costal cartilages, it functions as the only connection between the upper limb and the shoulder girdle.

Given the incongruency between the articular surfaces, the SC joint stability is only achieved through the contribution of the surrounding structures, which include a joint capsule, an articular disk, and three ligaments: sternoclavicular, costoclavicular and interclavicular ligaments (Moore et al., 2010)

The motions of the SC articulation include elevation and depression, protraction and retraction, and axial rotation. The anterior view of the SC joint is illustrated in Figure 2-5:

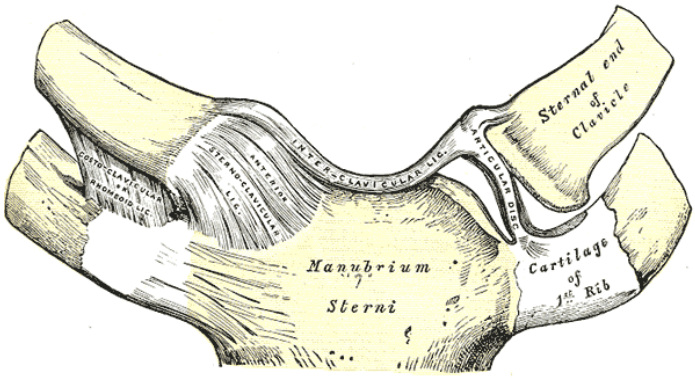

Figure 2-5: Anterior view of the sternoclavicular joint (Gray & Lewis, 1918)

2.1.2.2. Acromioclavicular Joint

The AC joint is a plane type of synovial joint connecting the acromial extremity of the clavicle and the acromion process of the scapula. The articulation is stabilized by the contribution of several mechanisms, such as the coracoclavicular ligament and the joint capsule surrounding the articular margins, and strengthened by fibres of the trapezius muscle and by the superior and inferior acromioclavicular ligaments. When present, the intra-articular disc, which is a thin oval plate of fibrocartilage, also increases the congruence of the AC joint (Moore et al., 2010; Quental, 2013a).

The movements of this joint, which has three rotational DOF, are associated with motion at the physiological scapulothoracic joint (Moore et al., 2010). These movements include: protraction/retraction about a vertical axis, elevation/depression about a sagittal axis and medial/lateral rotation about an axis that passes through the conoid ligament and the AC joint. The functional relevance of the AC joint is associated with providing extra mobility to the shoulder girdle, allowing the scapula to keep rotating when the SC joint movement reaches the limits imposed by the sternoclavicular ligaments (Palastanga & Soames, 2012). The anterior view of the AC joint is shown in Figure 2-6.

2.1.2.3. Glenohumeral Joint

The glenohumeral joint is a synovial-type joint, ball-and-socket variety that articulates the head of the humerus and the glenoid fossa of the scapula. Its wide range of motion stems from its geometric

characteristics (e.g., the glenoid cavity is only one third to one fourth of the articular surface of the humeral head), which also compromises joint stability, making it the most dislocated joint of the human body. Static and dynamic stabilizer mechanisms, such as the glenoid labrum, a strengthened joint capsule, glenohumeral, coracohumeral and transverse humeral ligaments, as well as the support of the surrounding muscular complex, in particular the rotator cuff, play a key role in joint stabilization (Moore et al., 2010; Palastanga & Soames, 2012).

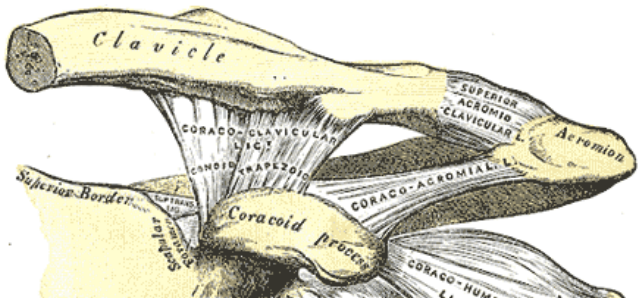

Figure 2-6: Anterior view of the acromioclavicular joint (Gray & Lewis, 1918)

The GH joint allows movements around three axes, permitting flexion/extension, abduction/adduction and medial/lateral rotation of the humerus. Except for small amplitude movements, few shoulder movements depend only on the GH joint; most of these movements are a composition of the contributions of each shoulder joint: SC, AC and GH.

The anterior view of the shoulder and its stabilizers and lateral view of the scapula showing the glenoid fossa are depicted in Figure 2-7.

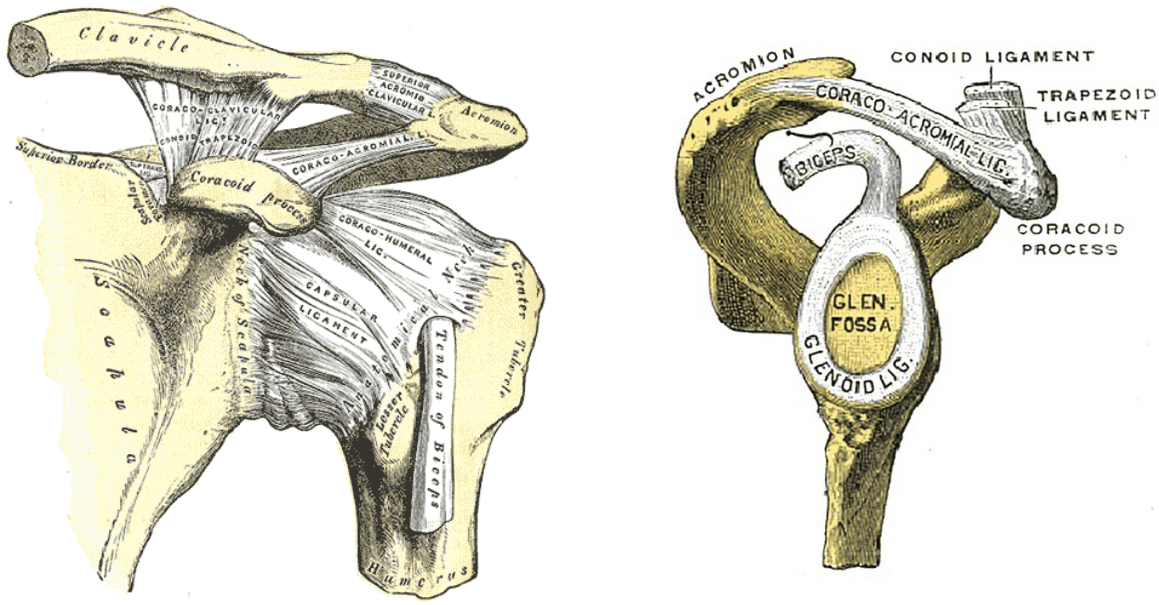

(a) (b)

Figure 2-7: Anterior view of the shoulder and its stabilizers (a) and lateral view of the scapula (b) showing the glenoid fossa (Gray & Lewis, 1918)

3. Multibody Dynamics Overview

Biomechanical models based on a multibody dynamics approach are often used to describe and study human motion characterized by large displacements (Silva, 2005). A multibody system is an assembly of interconnected bodies linked to each other by kinematic joints that constrain their relative motion (Nikravesh, 1988). Regarding the biomechanical modelling, bones are represented as rigid bodies and articulations are simplified as joints. To compute forces and torques for a known motion, this work performs an inverse dynamic analysis. Cartesian coordinates were selected for the description of the biomechanical model according to the notation followed by Nikravesh (1988).

3.1. Cartesian Coordinates

To fully describe the motion of an unconstrained three-dimensional body, six degrees of freedom (DOF) need to be defined using three translational coordinates and three rotational coordinates. Hence, position and orientation can be described with respect to a global reference frame using a body-fixed orthonormal frame where the translational coordinates locate the origin of the local frame and the rotational coordinates define the body orientation.

Although the analytic procedure behind spatial kinematics is similar to the planar situation, it requires a more complex mathematical approach, particularly to describe the angular orientation of each body. Instead of using three rotational coordinates, commonly denoted as Euler angles, the body orientation is defined by four coordinates known as Euler parameters. This alternate technique resorts to a set of four coordinates to depict rotational motion in a simpler, singularity-free, manner. Whereas Euler angles portray three sequential rotations over three different axes, Euler parameters represent one single rotation about a virtual axis, which results in a more efficient method to compute the same rotational matrix A. Since Euler parameters are not independent, they can be coupled using a single constraint $\mathbf{p}^T\mathbf{p} = 1$, where $\boldsymbol{p}$ is a vector $\boldsymbol{p} = [e_0, e_1, e_2, e_3]^T$ is a vector with all four Euler parameters (Nikravesh, 1988).
Taking into consideration this choice of coordinates, the location of a generic point P on body i in the global reference frame can be written in the global reference frame as:

$$\mathbf{r}_{\mathrm{i}}^{\mathrm{P}} = \mathbf{r}_i + \mathbf{A}_{\mathrm{i}}\, \mathbf{s}_{\mathrm{i}}'^{\mathrm{P}} \tag{3-1}$$

where $\mathbf{r}_{\mathrm{i}}$ is the vector with the location of the body-fixed frame of body i given in global coordinates, A_i is the rotational matrix accounting for the coordinate transformation from the local frame (ξ_i, η_i, ζ_i) to the global frame (x, y, z), and ${s_i}'^{P}$ is the vector that contains the local coordinates of point P with respect to the body-fixed frame.

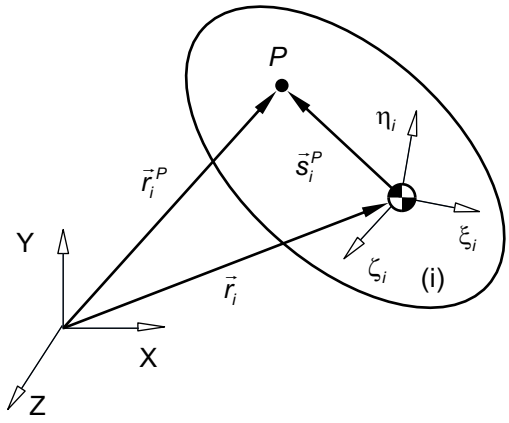

Figure 3-1: Location of point P in the global (XYZ) and local (ξ, η, ζ) reference frame.

Considering the position and orientation of *n* bodies of a given multibody system, a vector of generalized coordinates can be assembled to describe the entire system. The global position vector $\mathbf{q}$ encloses 7 coordinates per body – three translational coordinates, $\mathbf{r} = \{\mathrm{x}, \mathrm{y}, \mathrm{z}\}$, and four Euler parameters, $\mathbf{p} = \{e_0, e_1, e_2, e_3\}$ – which results in a vector of $(7 \times n)$ entries as follows:

$$\mathbf{q} = [\mathbf{q}_1^{\mathrm{T}},\ \mathbf{q}_2^{\mathrm{T}}, \dots\ \mathbf{q}_n^{\mathrm{T}}]^{\mathrm{T}}, \text{ with } \mathbf{q}_i = \left\{\mathbf{r}_i^{\mathrm{T}}, \mathbf{p}_i^{\mathrm{T}}\right\} = \{x, y, z, e_0, e_1, e_2, e_3\}_i^{\mathrm{T}} \tag{3-2}$$

In general, the coordinates in this vector are not independent. Kinematic joints constrain the relative motion of adjacent body segments, restricting the number of DOF of the multibody system. The relationship between the coordinates of the bodies can be translated into a vector of kinematic constraint algebraic equations. The number of independent equations corresponds to the number of constrained DOF. From a kinematic perspective, all constraint equations must be fulfilled for every time step, which can be written as:

$$\mathbf{\Phi}(\mathbf{q}, t) = [\mathbf{\Phi}_1(\mathbf{q}), \dots \mathbf{\Phi}_{ns}(\mathbf{q}), \dots \mathbf{\Phi}_1(\mathbf{q}, t), \dots \mathbf{\Phi}_{nr}(\mathbf{q}, t)]^{\mathrm{T}} = \mathbf{0} \tag{3-3}$$

where $\mathbf{\Phi}_i$ stands for the i^{th} kinematic constraint equation, n_s is the total number of scleronomic constraints, n_r is the total number of rheonomic constraints and **0** is the null vector. Scleronomic constraints are time independent constraints, i.e., the time variable is not explicitly declared in the algebraic equations; this type of constraint is usually associated with kinematic pairs. Rheonomic constraints are time dependent constraints that are usually related with driver actuators (Silva, 2003).

3.2. Kinematic Consistency

To achieve a fully consistent multibody system from a kinematic point of view, the prescribed motion should meet the imposed kinematic constraints. A kinematic analysis should be conducted to fulfill these requirements, namely by calculating the positions, velocities and accelerations in agreement with the topology of the mechanical system. Regardless of any external forces applied, this type of analysis only takes into consideration the motion imposed by driving constraints that guide one or several bodies of the system. Accordingly, the kinematic consistency of the positions can be calculated for every time step by solving Equation (3-3 with respect to the vector of generalized coordinates $\mathbf{q}$.

Because the kinematic constraint equations are generally non-linear in terms of the coordinates q, numerical methods, such as the Newton-Raphson procedure (Nikravesh, 1988), need to be employed to solve the non-linear system of equations. This iterative method achieves quadratic convergence by linearizing Equation (3-3). Using the first two terms of its expansion in a Taylor series, an approximate solution can be found by solving the following system of linear equations:

$$\mathbf{\Phi}(\mathbf{q}, t) \cong \mathbf{\Phi}(\mathbf{q}_i, t) + \mathbf{\Phi}_\mathbf{q}(\mathbf{q}_i)(\mathbf{q} - \mathbf{q}_i) = \mathbf{0} \tag{3-4}$$

where $\mathbf{\Phi}_\mathrm{q}(\mathbf{q}_\mathrm{i})$ is the Jacobian matrix, defined as the constraint system of partial derivatives of the system constraints with respect to the vector of generalized coordinates $\mathbf{q}$:

$$\mathbf{\Phi}_\mathbf{q}(\mathbf{q}) = \begin{bmatrix} \frac{\partial \mathbf{\Phi}_1}{\partial \mathbf{q}_1} & \cdots & \frac{\partial \mathbf{\Phi}_1}{\partial \mathbf{q}_{nc}} \\ \vdots & \ddots & \vdots \\ \frac{\partial \mathbf{\Phi}_{nh}}{\partial \mathbf{q}_1} & \cdots & \frac{\partial \mathbf{\Phi}_{nh}}{\partial \mathbf{q}_{nc}} \end{bmatrix} \tag{3-5}$$

where nc represents the number of coordinates and nh is the number of constraint equations. The approximate solution using the Newton-Raphson method is reached when the residual for the actual iteration, given by $\Delta\mathbf{q}_\mathrm{i} = \mathbf{q}_{\mathrm{i}+1} - \mathbf{q}_\mathrm{i}$, is below a predefined tolerance.

The vector of generalized velocities $\dot{\mathbf{q}}$ can be obtained after the consistency of the system positions is achieved. It can be calculated by deriving Equation (3-3) with respect to time. The first time derivative of the constraint equations, $\dot{\mathbf{\Phi}}$, comes as:

$$\dot{\mathbf{\Phi}}(\mathbf{q}, \dot{\mathbf{q}}, t) = \frac{\partial \mathbf{\Phi}(\mathbf{q}, t)}{\partial t} + \frac{\partial \mathbf{\Phi}(\mathbf{q}, t)}{\partial \mathbf{q}} \dot{\mathbf{q}} = \mathbf{0} \tag{3-6}$$

where $\frac{\partial \mathbf{\Phi}(\mathbf{q},\mathrm{t})}{\partial t}$ represents the vector of the partial derivatives of the constraints with respect to time, $\frac{\partial \mathbf{\Phi}(\mathbf{q},t)}{\partial q}$ is the Jacobian matrix and $\dot{\mathbf{q}}$ is the vector of generalized velocities. The right-hand side of the velocity equations can be characterized as the vector $\boldsymbol{\nu}(t)$, giving the following system of equations:

$$\mathbf{\Phi}_\mathbf{q}\dot{\mathbf{q}} = \boldsymbol{\nu}(t), \;\; with \;\; \boldsymbol{\nu}(t) = -\frac{\partial \mathbf{\Phi}(\mathbf{q}, t)}{\partial t} \tag{3-7}$$

Similarly, the two-time differentiation of Equation (3-3) with respect to time results in:

$$\ddot{\mathbf{\Phi}}(\mathbf{q}, \dot{\mathbf{q}}, \ddot{\mathbf{q}}, t) = \mathbf{\Phi}_\mathbf{q}\ddot{\mathbf{q}} + \left(\mathbf{\Phi}_\mathbf{q}\dot{\mathbf{q}}\right)_\mathbf{q}\dot{\mathbf{q}} - \dot{\boldsymbol{\nu}}(t) = \mathbf{0} \tag{3-8}$$

where $\ddot{\mathbf{q}}$ is the vector of generalized accelerations. The right-hand side of the acceleration equations can be depicted as the vector $\boldsymbol{\gamma}(t)$, which allows rewriting Equation (3-8) as:

$$\mathbf{\Phi}_\mathbf{q}\ddot{\mathbf{q}} = \boldsymbol{\gamma}(\mathbf{q}, \dot{\mathbf{q}}, t), \;\; with \;\; \boldsymbol{\gamma}(\mathbf{q}, \dot{\mathbf{q}}, t) = \dot{\boldsymbol{\nu}}(t) - \left(\mathbf{\Phi}_\mathbf{q}\dot{\mathbf{q}}\right)_\mathbf{q}\dot{\mathbf{q}} \tag{3-9}$$

Solving Equations (3-4), (3-7) and (3-9) enables the kinematic consistency of the multibody system, i.e., the identification of consistent positions, velocities and accelerations, respectively.

Biomechanical systems, which have more constraint equations than DOF, give rise to overdeterminate problems. This redundancy can be worked out by employing a least-squared method that minimizes the sum of the squared residual (Silva, 2003).

3.3. Kinematic Constraints

The constitutive elements of a mechanical system are frequently linked by one or several kinematic joints. These kinematic joints constrain the relative motion between two adjacent bodies and, ultimately, the overall motion of the entire system. They are portrayed as algebraic equations and must be depicted in a coherent set of coordinates, which in this case is based on cartesian coordinates.

Joint constraints restrain the motion of interconnected pairs, and, in kinematically driven systems, driver constraints prescribe motion over time. In the following subsections, the types of kinematic constraints applied for the description of the full-body skeletal model of the human body developed here are mathematically described, including the constraint equation(s) that restrict the DOF, and their contribution to the Jacobian matrix and right-hand side vectors of the velocity and acceleration equations. Spherical, universal and revolute joints, as well as prescribed motion and rotational driver constraints, are addressed.

3.3.1. Spherical Joint

A spherical joint, also called ball-and-socket, is a link between two adjacent rigid bodies *i* and *j* that allows three out of six possible DOF. The centre of the joint is located at a given point P, defined in the body-reference frame of both bodies *i* and *j*. The allowed rotational movement happens around this point and the vector of constrained positions is as follows:

$$\mathbf{\Phi}^{(s,3)} = \mathbf{r}_i + \mathbf{A}_i \mathbf{s}_i'^P - \mathbf{r}_j - \mathbf{A}_j \mathbf{s}_j'^P = \mathbf{0} \tag{3-10}$$

where the superscripts $(\boldsymbol{s}, \mathbf{3})$ indicate the type of joint and the number of constraint equations, $\mathbf{r}$ is the global position vector, $\mathbf{A}$ is the rotation matrix and $\boldsymbol{s}'^P$ is the position vector of point P in the local reference frame of bodies *i* and *j*, depending on the subscript. Figure 2-1 shows a spherical joint connecting bodies *i* and *j.*

For the sake of simplicity, both the Jacobian matrix and the right-hand side of vectors of the velocity and acceleration equations are adapted so that they can be described in terms of local angular velocities and accelerations. By differentiating Equation (3-10) with respect to time, the velocity vector of the constraint equations for the spherical joint results in:

$$\dot{\mathbf{\Phi}}^{(s,3)} = \frac{\partial \mathbf{\Phi}^{(s,3)}}{\partial \mathbf{r}_i}\dot{\mathbf{r}}_i + \frac{\partial \mathbf{\Phi}^{(s,3)}}{\partial \mathbf{p}_i}\dot{\mathbf{p}}_i + \frac{\partial \mathbf{\Phi}^{(s,3)}}{\partial \mathbf{r}_j}\dot{\mathbf{r}}_j + \frac{\partial \mathbf{\Phi}^{(s,3)}}{\partial \mathbf{p}_j}\dot{\mathbf{p}}_j = \tag{3-11}$$

$$= \frac{\partial \mathbf{\Phi}^{(s,3)}}{\partial \mathbf{r}_i}\dot{\mathbf{r}}_i + \frac{1}{2}\frac{\partial \mathbf{\Phi}^{(s,3)}}{\partial \mathbf{p}_i}\mathbf{L}_i^{\mathrm{T}}\boldsymbol{\omega}'_i + \frac{\partial \mathbf{\Phi}^{(s,3)}}{\partial \mathbf{r}_j}\dot{\mathbf{r}}_j + \frac{1}{2}\frac{\partial \mathbf{\Phi}^{(s,3)}}{\partial \mathbf{p}_j}\mathbf{L}_j^{\mathrm{T}}\boldsymbol{\omega}'_j$$

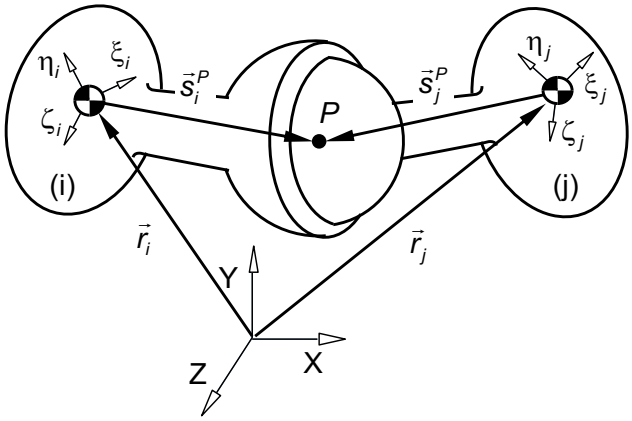

Figure 3-2: Spherical joint between bodies *i* and *j*.

where $\frac{\partial \mathbf{\Phi}^{(s,3)}}{\partial \mathbf{r}}$ and $\frac{\partial \mathbf{\Phi}^{(s,3)}}{\partial \mathbf{p}}$ represent the partial derivatives of the constraints with respect to the position $\mathbf{r}$ and the Euler parameters $\mathbf{p}$, respectively, and $\mathbf{L}$ is a local transformation matrix given by (Nikravesh 1988)

$$\mathbf{L} = \begin{bmatrix} -e_1 & e_0 & e_3 & -e_2 \\ -e_2 & -e_3 & e_0 & e_1 \\ -e_3 & e_2 & -e_1 & e_0 \end{bmatrix} \tag{3-12}$$

The spherical joint contributions to the global Jacobian matrix and to the right-hand side vector of the velocity equations can be described as (Nikravesh, 1988):

$$\begin{array}{c} \dot{\mathbf{r}}_1 \quad \boldsymbol{\omega}'_1 \quad \ldots \quad \dot{\mathbf{r}}_i \quad \boldsymbol{\omega}'_i \quad \ldots \quad \dot{\mathbf{r}}_j \quad \boldsymbol{\omega}'_j \quad \ldots \quad \dot{\mathbf{r}}_n \quad \boldsymbol{\omega}'_n \\ \mathbf{\Phi}_{\mathbf{q}}^{(s,3)} = \begin{bmatrix} \mathbf{0} & \mathbf{0} & \ldots & \mathbf{I} & -\tilde{\mathbf{s}}_i^P\mathbf{A}_i & \ldots & -\mathbf{I} & \tilde{\mathbf{s}}_j^P\mathbf{A}_j & \ldots & \mathbf{0} & \mathbf{0} \end{bmatrix} \\ \boldsymbol{\nu}^{(s,3)} = \mathbf{0} \end{array} \tag{3-13}$$

For an easier understanding of the contribution of each term, references to the corresponding translational and angular velocities were placed above the respective columns of the Jacobian matrix. In Equation(3-13), $\mathbf{I}$ represents the Identity matrix [3 x 3] and $\tilde{\mathbf{s}}^{\mathrm{P}}$ is the skew-symmetric matrix of $\mathbf{s}^{\mathrm{P}}$of bodies *i* and *j*, depending on the subscript, given by:

$$\tilde{\mathbf{s}}^{\mathrm{P}} = \begin{bmatrix} 0 & -\mathrm{s_z} & \mathrm{s_y} \\ \mathrm{s_z} & 0 & \mathrm{s_x} \\ -\mathrm{s_y} & \mathrm{s_x} & 0 \end{bmatrix} \tag{3-14}$$

The ball-and-socket input to the right-hand side vector of the acceleration equations is given by:

$$\boldsymbol{\gamma}^{(s,3)} = -\tilde{\boldsymbol{\omega}}_i \dot{\mathbf{s}}_i^P + \tilde{\boldsymbol{\omega}}_j \dot{\mathbf{s}}_j^P, \text{ with } \dot{\mathbf{s}}^P = \tilde{\boldsymbol{\omega}} \mathbf{s}^P \tag{3-15}$$

where $\tilde{\boldsymbol{\omega}}$ represents the skew-symmetric matrix of the global angular velocity and $\dot{\mathbf{s}}^{\mathrm{P}}$ is the time derivative of bodies *i* or *j*.

3.3.2. Universal Joint

The universal joint, or cardan joint, connects bodies *i* and *j* and has two rotational DOF overall. All three translational DOF are restricted, meaning that the same set of equations defined in Equation (3-10) for the spherical joint apply here as well. The axes of rotation of this joint intersect at point P, constraining one rotational DOF. Figure 3-3 depicts the universal joint.

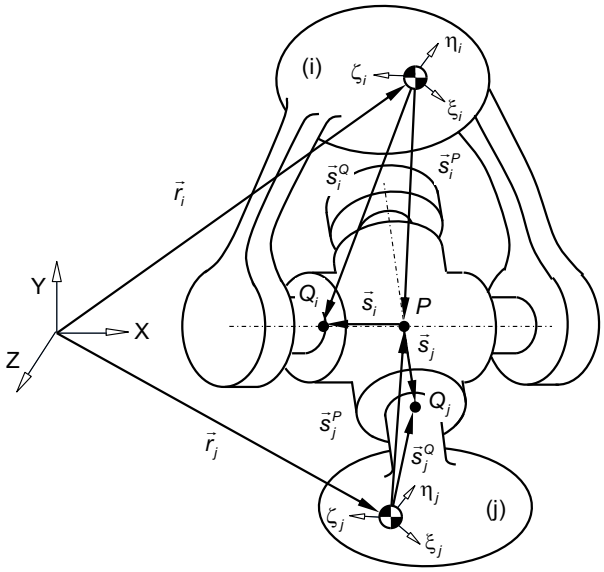

Figure 3-3: Universal joint between bodies *i* and *j*. The vector $\mathbf{s}_{\mathrm{i}}$ is perpendicular to $\mathbf{s}_{\mathrm{j}}$.

Vectors $\mathbf{s}_{\mathrm{i}}$ and $\mathbf{s}_{\mathrm{j}}$, with the same direction of the two rotational axes, must always remain perpendicular. The constraint equations of the universal joint can be represented as:

$$\boldsymbol{\Phi}^{(u,4)} = \begin{bmatrix} \boldsymbol{\Phi}^{(s,3)} \\ \mathbf{s}_i^{\mathrm{T}} \mathbf{s}_j \end{bmatrix} = \mathbf{0} \tag{3-16}$$

The contribution of the universal joint constraints to the Jacobian matrix, as well as to the right-hand side vectors of the velocity and acceleration equations, can be written as (Nikravesh, 1988):

$$\boldsymbol{\Phi}_{\mathbf{q}}^{(u,4)} = \begin{bmatrix} & & & & & \boldsymbol{\Phi}_{\mathbf{q}}^{(s,3)} & & & & & \\ \mathbf{0} & \mathbf{0} & \dots & \mathbf{0} & -\mathbf{s}_j^{\mathrm{T}} \tilde{\mathbf{s}}_i \mathbf{A}_i & \dots & \mathbf{0} & -\mathbf{s}_i^{T} \tilde{\mathbf{s}}_j \mathbf{A}_j & \dots & \mathbf{0} & \mathbf{0} \end{bmatrix} \tag{3-17}$$

$$\boldsymbol{\nu}^{(u,4)} = \mathbf{0}$$

$$\boldsymbol{\gamma}^{(u,4)} = \begin{bmatrix} \boldsymbol{\gamma}^{(s,3)} \\ -2\dot{\mathbf{s}}_i^{\mathrm{T}}\dot{\mathbf{s}}_j + \dot{\mathbf{s}}_i^{\mathrm{T}}\tilde{\boldsymbol{\omega}}_i\mathbf{s}_j + \dot{\mathbf{s}}_j^{\mathrm{T}}\tilde{\boldsymbol{\omega}}_j\mathbf{s}_i \end{bmatrix}$$

3.3.3. Revolute Joint

The revolute joint, illustrated in Figure 3-4 between bodies *i* and *j*, allows only one rotational DOF about a single axis.

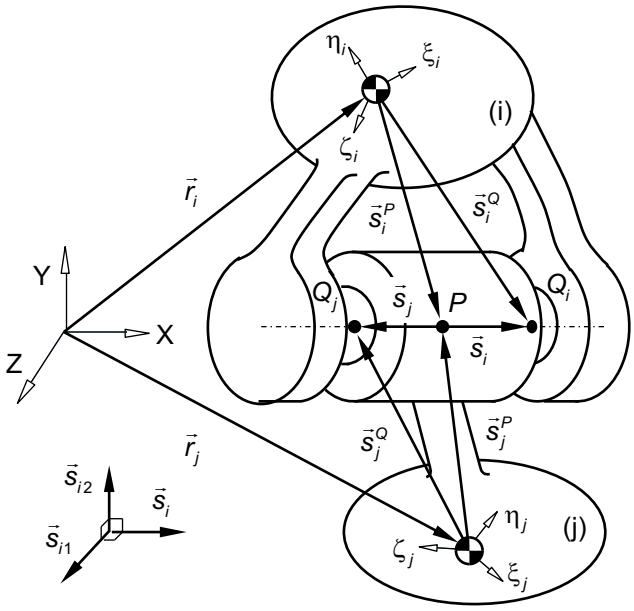

Figure 3-4: Revolute joint between bodies i and j. The vectors $\boldsymbol{s}_{i1}$ and $\boldsymbol{s}_{i2}$ represented in the left low corner are simultaneously perpendicular to $\boldsymbol{s}_i$ and to each other, and $\boldsymbol{s}_i$ is the vector defining the joint axis of rotation from the configuration of body i.

Vectors $\mathbf{s}_\mathrm{i}$ and $\mathbf{s}_\mathrm{j}$ defined in bodies *i* and *j* correspond to the joint axis of rotation. The revolute joint can be seen as an extension of the spherical joint with two additional rotational constrained DOF. These rotational constraint equations must ensure that these two vectors always remain parallel. Instead of enforcing the constraint through a single cross-product, which results in three constraint equations, two of them linearly dependent, two dot-products are considered (Quental, 2013). Figure 3-4 shows, in the left low corner, the generation of two additional vectors $s_{i1}$and s_{i2}, which are both perpendicular to s_i and to each other. The constraint equations of the revolute joint are expressed as:

$$\boldsymbol{\Phi}^{(r,5)} = \begin{bmatrix} \boldsymbol{\Phi}^{(s,3)} \\ \mathbf{s}_{i1}^{\mathrm{T}}\mathbf{s}_j \\ \mathbf{s}_{i2}^{\mathrm{T}}\mathbf{s}_j \end{bmatrix} = \mathbf{0} \tag{3-18}$$

The contribution of the revolute joint constraints to the Jacobian matrix and to the right-hand side vector of the velocity and acceleration equations is given by (Nikravesh, 1988):

$$\boldsymbol{\Phi}_{\mathbf{q}}^{(r,5)} = \begin{bmatrix} & & & & & \boldsymbol{\Phi}_{\mathbf{q}}^{(s,3)} & & & & & \\ \mathbf{0} & \mathbf{0} & \dots & \mathbf{0} & -\mathbf{s}_j^{\mathrm{T}}\tilde{\mathbf{s}}_{i1}\mathbf{A}_i & \dots & \mathbf{0} & -\mathbf{s}_{i1}^{\mathrm{T}}\tilde{\mathbf{s}}_j\mathbf{A}_j & \dots & \mathbf{0} & \mathbf{0} \\ \mathbf{0} & \mathbf{0} & \dots & \mathbf{0} & -\mathbf{s}_j^{\mathrm{T}}\tilde{\mathbf{s}}_{i2}\mathbf{A}_i & \dots & \mathbf{0} & -\mathbf{s}_{i2}^{\mathrm{T}}\tilde{\mathbf{s}}_j\mathbf{A}_j & \dots & \mathbf{0} & \mathbf{0} \end{bmatrix}$$

$$\boldsymbol{\nu}^{(r,5)} = \mathbf{0}$$

$$\boldsymbol{\gamma}^{(r,5)} = \begin{bmatrix} \boldsymbol{\gamma}^{(s,3)} \\ -2\dot{\mathbf{s}}_i^{\mathrm{T}}\dot{\mathbf{s}}_j + \dot{\mathbf{s}}_i^{\mathrm{T}}\tilde{\boldsymbol{\omega}}_i\mathbf{s}_j + \dot{\mathbf{s}}_j^{\mathrm{T}}\tilde{\boldsymbol{\omega}}_j\mathbf{s}_i \\ -2\dot{\mathbf{s}}_i^{\mathrm{T}}\dot{\mathbf{s}}_j + \dot{\mathbf{s}}_i^{\mathrm{T}}\tilde{\boldsymbol{\omega}}_i\mathbf{s}_j + \dot{\mathbf{s}}_j^{\mathrm{T}}\tilde{\boldsymbol{\omega}}_j\mathbf{s}_i \end{bmatrix}$$

3.3.4. Prescribed Motion Constraint

In the three-dimensional space, the absolute motion of a multibody system over time can be mathematically described through a driving constraint that guides the position and orientation of a given body of the multibody system. The motion of this base body can be described by a prescribed motion constraint, illustrated in Figure 3-5.

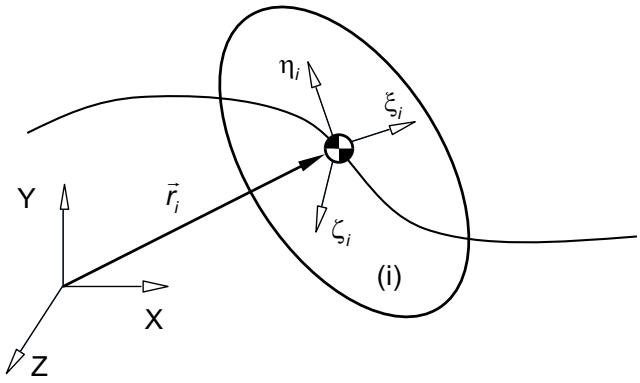

Figure 3-5: Prescribed motion constraint applied to body i.

The driving body is the reference for the whole multibody system. In the biomechanical model developed here, and described in detail later, the pelvis is the selected segment to be driven. Seven constraint equations are used to define the prescribed motion constraint:

$$\boldsymbol{\Phi}^{(pmc,7)} = \mathbf{q}_i - \mathbf{q}_i^*(t) = \mathbf{0} \tag{3-19}$$

where $\mathbf{q}^*(t)$ is the actual position vector of body i at the instant of time t.

The contribution of the prescribed motion constraint to the Jacobian matrix and to the right-hand side vectors of the velocity and acceleration constraint equations is given by:

$$\mathbf{\Phi}_{\mathbf{q}}^{(pmc,7)} = \begin{bmatrix} \mathbf{0} & \mathbf{0} & \dots & \mathbf{I} & \mathbf{0} & \dots & \mathbf{0} & \mathbf{0} \\ \mathbf{0} & \mathbf{0} & \dots & \mathbf{0} & \frac{1}{2}\mathbf{L}_i^{\mathrm{T}} & \dots & \mathbf{0} & \mathbf{0} \end{bmatrix}$$
$$\mathbf{v}^{(pmc,7)} = \dot{\mathbf{q}}_i^*(t) \tag{3-20}$$
$$\boldsymbol{\gamma}^{(pmc,7)} = \begin{bmatrix} \mathbf{r}_i^*(t) \\ \ddot{\mathbf{p}}_i^*(t) + \frac{1}{4}\left(\boldsymbol{\omega}_i'^{\mathrm{T}}\boldsymbol{\omega}'\right)\mathbf{p}_i \end{bmatrix}$$

where $\dot{\mathbf{q}}_i^*(t)$, $\ddot{\mathbf{r}}_i^*(t)$, and $\ddot{\mathbf{p}}_i^*(t)$ are the experimentally measured time dependent vectors of generalized velocities, translational accelerations, and second time derivatives of the Euler parameters of body i, respectively. These vectors are obtained by interpolating the prescribed motion vector $\mathbf{q}_i^*(t)$ and by differentiating these once and twice with respect to time to obtain, respectively, velocity and acceleration.

3.3.5. Rotational Driver Constraint

The rotational driver constraint guides a rotational DOF between bodies. For the sake of simplicity, the rotational driver constraint is explained considering the human knee, which can be described by a revolute joint and a rotational driver, as illustrated inFigure 3-6. The kinematic joint allows only knee flexion and extension, while the driver is responsible for controlling the angle variation $\theta(t)$. The vectors u and v are defined as unitary vectors and, in this situation, u is aligned with the axis η_i and v has the opposite direction of η_j. Since both vectors are unitary, their dot-product corresponds to the cosine of the angle between them. Consequently, the constraint equation is written as:

$$\mathbf{\Phi}^{(rd,1)} = \mathbf{u}^{\mathrm{T}}\mathbf{v} - \cos\left(\theta(t)\right) = 0, \text{ with } \theta(t) = \langle \mathbf{u}, \mathbf{v} \rangle(t) \tag{3-21}$$

The contribution of the driver constraints to the Jacobian matrix and the right-hand side vectors of the velocity and acceleration equations is given by:

$$\mathbf{\Phi}_{\mathbf{q}}^{(rd,1)} = \begin{bmatrix} \mathbf{0} & \mathbf{0} & \dots & \mathbf{0} & -\mathbf{v}^{\mathrm{T}}\tilde{\mathbf{u}}\mathbf{A}_i & \dots & \mathbf{0} & -\mathbf{u}^{\mathrm{T}}\tilde{\mathbf{v}}\mathbf{A}_j & \dots & \mathbf{0} & \mathbf{0} \end{bmatrix}$$
$$\mathbf{v}^{(rd,1)} = -\sin\left(\theta(t)\right) \cdot \dot{\theta}(t) \tag{3-22}$$
$$\boldsymbol{\gamma}^{(rd,1)} = -2\dot{\mathbf{u}}^{\mathrm{T}}\dot{\mathbf{v}} + \dot{\mathbf{u}}^{\mathrm{T}}\tilde{\boldsymbol{\omega}}_i\mathbf{v} + \dot{\mathbf{v}}^{\mathrm{T}}\tilde{\boldsymbol{\omega}}_j\mathbf{u} - \cos\left(\theta(t)\right) \cdot \dot{\theta}(t)^2 - \sin\left(\theta(t)\right) \cdot \ddot{\theta}(t)$$

where $\dot{\theta}(t)$ and $\ddot{\theta}(t)$ are, respectively, the first and second derivatives of a cubic spline interpolation of the rotating angle variation $\theta(t)$.

3.4. Inverse Dynamic Analysis

An inverse dynamic analysis is a methodology that allows the study of motion of a system subjected to externally applied forces that modify the dynamic behaviour of its components, according to its topology, kinematic constraints, and pre-defined motion (Silva, 2003). An inverse dynamic analysis can only be conducted after achieving full consistency between the motion under study and the kinematic constraints, i.e., if the kinematic constraint equations given by Equation (3-3) are fulfilled.

From a biomechanical point of view, the purpose of an inverse dynamic analysis is to obtain the internal forces of the biomechanical system, which may include intersegmental joint forces, joint moments-of-force, and muscle forces.

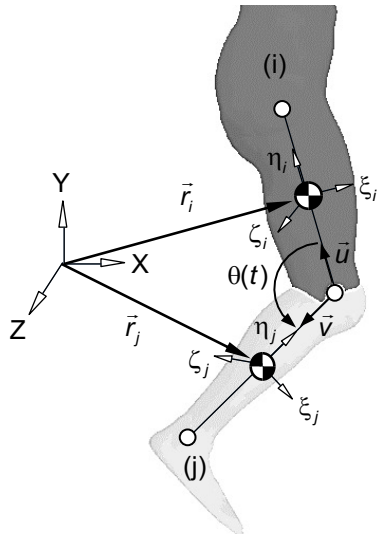

Figure 3-6: Rotational driver constraint applied between bodies i and j.

3.4.1. Joint Reaction Forces

Each kinematic joint introduces reaction forces, also known as constraint forces, between the linked body segments. Considering that these forces are defined with respect to the same coordinate system as the vector of generalised positions, $\mathbf{q}$, they can be expressed in terms of the constraint equations of the multibody system (Nikravesh, 1988). This relationship is obtained using the Lagrange multipliers method defined in Nikravesh (1988), and expressed by:

$$\mathbf{g}^{(c)} = -\mathbf{\Phi}_{\mathbf{q}}^{\mathrm{T}}\boldsymbol{\lambda} \tag{3-23}$$

where $\mathbf{g}(c)$ represents the generalised vector of internal reaction forces, and $\boldsymbol{\lambda}$ is the vector of Lagrange multipliers. From the physical point of view, the rows of the Jacobian matrix define the direction of the constraint forces while the Lagrange multipliers define their unknown magnitudes. For instance, in the case of joint rotational actuators, their meaning is associated with the net moment-of-force produced by all the muscles crossing the specified joint (Silva & Ambrósio, 2003).

3.4.2. Equations of Motion

For a general constrained multibody system, the equations of motion can be described as:

$$\mathbf{M}\ddot{\mathbf{q}} = \mathbf{g} + \mathbf{g}^{(c)} \tag{3-24}$$

where $\mathbf{M}$ is the mass matrix of the system, containing the body mass and moment of inertia all bodies, $\ddot{\mathbf{q}}$ is the vector of generalised accelerations, and $\mathbf{g}$ is the vector of external forces. Combining Equations (3-23) and (3-24), the equations of motion become:

$$\mathbf{M}\ddot{\mathbf{q}} + \boldsymbol{\Phi}_{\mathbf{q}}^{\mathrm{T}}\boldsymbol{\lambda} = \mathbf{g} \tag{3-25}$$

In an inverse dynamic analysis, in which the kinematic data are fully known, the equations of motion are solved for the unknown Lagrange multipliers, which are directly associated with the intersegmental joint forces and joint torques of the human body model (Silva and Ambrósio, 2003). This Lagrange multipliers quantify the intersegmental forces that are developed by the kinematic constraints. As stated earlier, the internal product of the vector of Lagrange multipliers by the transpose of the Jacobian matrix of the multibody system provides the intersegmental joint forces and joint torques developed by the driver actuators, which can ultimately be substituted my muscular actuation, in the case of a biomechanical system. The results concerning the inverse dynamic analysis conducted in this work are described in Chapter 6.

4. Biomechanical Model Formulation

In this chapter, a 3D multibody biomechanical model will be proposed to study and describe the front crawl swimming motion. A biomechanical model is a mathematical discretization of the highly complex human body system. The model characteristics should answer the requirements of the motion under analysis. Biomechanical models are often used to simulate the mechanical behaviour of the human body during the performance of various activities. This work focuses on a full body representation with a special emphasis on the upper limb.

4.1. Model Topology

The motion under study is highly complex involving several limbs to propel and lift the body while swimming, which makes it relevant to propose a full-body biomechanical approach. To obtain the necessary information concerning dimensional and physical properties of anatomical bodies for the development of an appropriate anthropometric model, scaling equations based on linear regression were used. Dumas et al. (2007a) established a complete dataset of scaling equations that resort to total body mass and segment length for the computation of BSIPs (body segment inertial parameters) for both male and female human subjects. These equations are based on the work of McConville et al. (1980), who studied 31 adult males (mean age 27.5 years old, mean weight 80.5 kg, mean stature 1.77 m). Dumas et al. (2007) also adapted data from McConville et al. (1980) to express BSIPs directly in the conventional segment coordinate systems (Wu et al., 2002, 2005) and without restraining the position of the centre of mass (COM) and the orientation of the principal axes of inertia. These equations provide BSIPs for all bodies in the current biomechanical model except for the neck and head – which are considered two separate bodies, following the approach proposed by Pàmies (2012) – and the shoulder girdle.

Due to its extreme anatomical complexity and high demand during the front crawl motion (Davies et al., 2009), studying in detail the role of the upper limb in the context of swimming is of the utmost importance. In this study, the shoulder girdle was modelled based on the work of Quental et al. (2012), which relied on data computed by Garner & Pandy (2001) from high-resolution medical images of the muscles and bones, obtained from the Visible Human Male (VHM) project (Spitzer et al., 1996). To ensure consistency of the shoulder girdle data with the developed biomechanical model, the anthropometric information extracted from the Lisbon Shoulder Model (LSM, Quental et al., 2012) was scaled to match the characteristics computed using the regression equations applied to the subject under analysis.

The current biomechanical model considers 20 rigid bodies including the pelvis, torso, neck, head, and right and left thighs, legs, feet, clavicles, scapulae, arms, forearms, and hands. The anatomical segments are detailed in Table 4-1 and Figure 4-1.

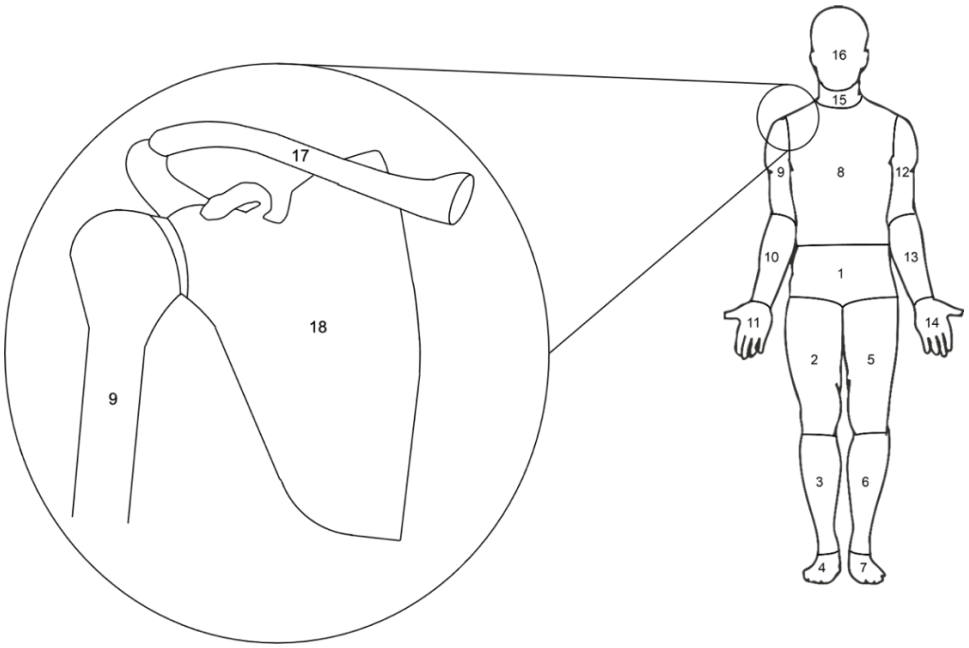

Figure 4-1: Schematic representation of the full body biomechanical model of the human body

Table 4-1: Definition of the anatomical segments of the current biomechanical model

ID	Rigid Body	Description
1	Pelvis	From the 1st lumbar vertebra to the pelvic bone
2	Right Thigh	From right hip to right knee
3	Right Leg	From right knee to right ankle
4	Right Foot	From right ankle to midpoint between 1st and 5th right metatarsals
5	Left Thigh	From left hip to left knee
6	Left Leg	From left knee to left ankle
7	Left Foot	From left ankle to midpoint between 1st and 5th left metatarsals
8	Torso	From the 1st to the 12th thoracic vertebra
9	Right Arm	From right shoulder to right elbow
10	Right Forearm	From right elbow to right wrist
11	Right Hand	From right wrist to midpoint between 2nd and 5th right metacarpals
12	Left Arm	From left shoulder to left elbow
13	Left Forearm	From left elbow to left wrist
14	Left Hand	From left wrist to midpoint between 2nd and 5th left metacarpals
15	Neck	From the 1st to the 7th cervical vertebra
16	Head	Cranium, upper and lower jaws
17	Right Clavicle	From the most ventral point on the right SC joint to the most dorsal point on the right AC joint
18	Right Scapula	Triangle connecting the most dorsal point of right AC joint, the right trigonum spinae scapulae and the right angulus inferior
19	Left Clavicle	From the most ventral point on the right SC joint to the most dorsal point on the right AC joint
20	Left Scapula	Triangle connecting the most dorsal point of left AC joint, the left trigonum spinae scapulae and the left angulus inferior

4.2. Scaling Anthropometric Data for the Shoulder Complex

To build a consistent biomechanical model for the whole human body, the anthropometric data regarding the shoulder girdle had to be adapted from Quental et al. (2012). Characteristics such as lengths, body masses and moments of inertia were scaled to fit anthropometric measurements computed using the regression equations from Dumas et al. (2007a, 2007b). Using a standard procedure adapted from Laananen (1991), the non-dimensional scaling factors relate the anthropometric characteristics based on one subject from the VHM project (male subject, 1.80m, 90.26kg, Spitzer et al., 1996) and the subject's height and weight. The applied scaling factors (for length, mass and inertia) were:

$$\chi_{Li} = \frac{L_i}{L}, \qquad \chi_{mi} = \frac{m_i}{M}, \qquad \chi_{Ii} = \frac{I_i}{M \cdot L} \tag{4-1}$$

where L_i is the length of a given segment of body *i*, L is the height of the male subject measured for the VHM project, m_i is the mass of body *i*, M is the total mass of the individual and I_i corresponds to the moments of inertia in each component for body *i*.

It is worth noting that this methodology is only applicable to male subjects whose percentile is not too far apart from the male subject from the VHM project. This means that, for individuals of different gender, with considerable differences in total height or weight, or even anatomical dissimilarities or disabilities, these scaling factors should be used with care.

4.3. Anthropometric Measurements

The subject under analysis is a 25-year-old male swimmer with 70.3 kg, and 1.80 m, fitting the target population of the scaling equations by Dumas et al. (2007a; 2007b). Except for the head, neck and segments of the shoulder girdle, all anthropometric measurements were calculated using this set of coherent scaling equations, contributing for a more comprehensive and consistent biomechanical model of the whole human body.

The anthropometric measurements for the shoulder girdle were obtained considering the method described in the previous subsection by scaling data from the Lisbon Shoulder Model (Quental et al., 2012), which relied on a comprehensive dataset obtained through *in vivo* measurements of a single male cadaver (Garner & Pandy, 2001; Spitzer et al., 1996). The resulting anthropometric data are synthetised in Table 4-2.

4.4. Articular System

The current biomechanical model followed a combination of the works of Oliveira (2016), for a description of the whole body, and Quental et al. (2012), for a more accurate discretization of the upper limb. Twenty bodies are interconnected by nineteen articulations, including twelve spherical (ball-and-socket) joints, four universal (cardan) joints, and three revolute (hinge) joints. The complete articular system comprises right and left hip, knee, ankle, SC, AC, GH, elbow, and wrist joints and the lumbar, cervical and occipital joints. For the sake of simplicity, the scapulothoracic joints were neglected and the upper extremity was modelled as an open chain.

Table 4-2: Anthropometric data scaling parameters for the twenty anatomical segments of the developed biomechanical model. The ID corresponds to the numeration in Figure 4-1. The scaling factors for the computation of COM, moments of inertia, and products of inertia are described in the respective body's local reference frame (with the origin at the proximal joint).

ID	Name	Mass scaling factor [1] (%)	Scaling factor for the COM in local reference frame[2] (%)			Scaling factor for tensor of inertia[3] (%)					
			ξ	η	ζ	$\xi\xi$	$\eta\eta$	$\zeta\zeta$	$\xi\eta$	$\xi\zeta$	$\eta\zeta$
1	Pelvis	0,142	0,336	0,149	0,003	1,010	1,060	0,950	-0,250	-0,120	-0,080
2	Right Thigh	0,123	0,041	0,429	-0,033	0,290	0,150	0,300	0,070	-0,020	-0,070
3	Right Leg	0,048	0,048	0,410	-0,007	0,280	0,100	0,280	-0,040	-0,020	0,050
4	Right Foot	0,012	-0,382	0,151	-0,026	0,170	0,370	0,360	0,130	-0,080	0,000
5	Left Thigh	0,123	-0,041	0,429	-0,033	0,290	0,150	0,300	0,070	-0,020	-0,070
6	Left Leg	0,048	-0,048	0,410	-0,007	0,280	0,100	0,280	-0,040	-0,020	0,050
7	Left Foot	0,012	0,382	0,151	-0,026	0,170	0,370	0,360	0,130	-0,080	0,000
8	Torso	0,309	0,036	0,420	0,002	0,270	0,250	0,280	0,180	0,020	-0,040
9	Right Arm	0,024	-0,017	0,452	0,026	0,310	0,140	0,320	0,060	0,050	0,020
10	Right Forearm	0,017	-0,010	0,417	-0,014	0,280	0,110	0,270	0,030	0,020	-0,080
11	Right Hand	0,006	-0,082	0,839	-0,074	0,610	0,380	0,560	0,220	0,150	-0,200
12	Left Arm	0,024	0,017	0,452	0,026	0,310	0,140	0,320	0,060	0,050	0,020
13	Left Forearm	0,017	0,010	0,417	-0,014	0,280	0,110	0,270	0,030	0,020	-0,080
14	Left Hand	0,006	0,082	0,839	-0,074	0,610	0,380	0,560	0,220	0,150	-0,200
15	Neck	0,013	0,000	-0,388	0,000	0,280	0,210	0,300	-0,070	-0,020	0,030
16	Head	0,054	-0,271	-0,104	0,000	0,280	0,210	0,300	-0,070	-0,020	0,030
17	Right Clavicle	0,001	-0,001	-0,009	-0,041	$1{,}0 \cdot 10^{-6}$	$1{,}0 \cdot 10^{-6}$	$2{,}4 \cdot 10^{-8}$	0	0	0
18	Right Scapula	0,011	0,029	0,012	0,027	$8{,}1 \cdot 10^{-6}$	$5{,}5 \cdot 10^{-6}$	$1{,}3 \cdot 10^{-6}$	0	0	0
19	Left Clavicle	0,001	0,001	-0,009	-0,041	$1{,}0 \cdot 10^{-6}$	$1{,}0 \cdot 10^{-6}$	$2{,}4 \cdot 10^{-6}$	0	0	0
20	Left Scapula	0,011	-0,029	0,012	0,027	$8{,}1 \cdot 10^{-6}$	$5{,}5 \cdot 10^{-6}$	$1{,}0 \cdot 10^{-5}$	0	0	0

[1] The scaling factor for the mass of each body refers to the subject's total weight.

[2] The scaling factors of the location of the COM in the local reference frame refer to the corresponding segment length, except for the following bodies: right and left clavicle (bodies number 17 and 19) and right and left scapula (bodies number 18 and 20). For these bodies, the indicated percentages are related with the subject's height.

[3] All scaling factors for the moments of inertia correspond to the radii of gyration, except for the right and left clavicles and right and left scapulae. The tensor of inertia can be calculated by employing the expression:

$$[I_i]_{3\,x\,3} = \begin{bmatrix} {r_{xx}}^2 & {r_{xy}}^2 & {r_{xz}}^2 \\ {r_{yx}}^2 & {r_{yy}}^2 & {r_{yz}}^2 \\ {r_{zx}}^2 & {r_{zy}}^2 & {r_{zz}}^2 \end{bmatrix} \cdot L_i \cdot M_i,$$

with L_i being the segment length and M_i the mass of the body, the mass of the body, except for the clavicle and scapulae, for which they are, respectively, the subject's height and weight (see Subsection 4.2).

The introduction of the SC and AC joints in the biomechanical model is of the utmost importance in front crawl swimming. The shoulder complex offers the greatest range of motion of any joint system in the human body. Throughout the human evolution, the development of a more laterally directed glenoid cavity of the scapula and a longer and more laterally twisted clavicle improved human capability to raise the arm when compared to other non-biped mammals (Isler, 2005; Veeger & van der Helm, 2007). This wide-range mobility is due to the simultaneous movement of the SC, AC and GH joints, counterbalanced by the stabilizing role of the musculotendinous and ligament complex of the shoulder (Tovin, 2006; Veeger & van der Helm, 2007). These features are fundamental for the development of the front crawl swimming technique, because they allow the shoulder to withstand large external forces, such as hydrodynamic forces, while granting enough freedom for the upper limb to perform complex movement patterns (Tovin, 2006).

If unconstrained, each body conveys six DOF (three translational and three rotational) to the system. Since the motion of the anatomical segments is limited by the joints connecting them, the system's total number of DOF corresponds to:

$$\begin{aligned} \mathrm{DOF}_{Total} &= (\mathrm{N}_{bodies} \times N_{DOF}) \\ &\quad - (\mathrm{N}_{SPH} \times N_{DOF\,SPH} + \mathrm{N}_{UNI} \times N_{DOF\,UNI} + \mathrm{N}_{REV} \times N_{DOF\,REV}) \end{aligned} \tag{4-2}$$

$$\mathrm{DOF}_{Total} = (20\ \mathrm{bodies} \times 6\ \mathrm{DOF}) - (12 \times 3_{SPH} + 4 \times 4_{UNIV} + 3 \times 5_{REV}) = 53\ DOF$$

where N_{bodies}, N_{SPH}, N_{UNI} and N_{REV} refer, respectively, to the total number of, spherical joints, universal joints, and revolute joints of the biomechanical system; N_{DOF}, $\mathrm{N}_{DOF\,SPH}$, $N_{DOF\,UNI}$ and $N_{DOF\,REV}$ describe, in the tri-dimensional space, the total number of DOF of an unconstrained body and total number of DOF constrained by spherical, universal and revolute joints, respectively. The 53 DOF of the system correspond to: 36 DOF allowed by the ball-and-socket joints, 8 DOF related with the universal joints, 3 DOF linked to the hinge joints, and 6 DOF describing the position and orientation of the pelvis (the body driving the motion of the human body as a whole). Comparing the current biomechanical model to that presented by Sequeira (2021), it is worth noting the impact of adding four extra bodies. Resulting in 4 extra articulations that were modelled as spherical joints - the SC and AC joints, the system gained twelve extra DOF, fundamental to understand the shoulder complex in the context of swimming.

To fully describe the anatomical joints, the joint centre of each articulation, as well as other relevant points, must be known in the local reference frame of the proximal and distal body segments. Following the Cartesian coordinates formulation described in Section 3, these local frames are positioned at the centre of mass of the bodies and are oriented according to the ISB recommendations (Wu et al., 2002, 2005). Since the ISB only normalizes the positioning and orientation for the reference frames of the right side of the body, an analogous process was followed to define those on the left-side using the left-side analogous bony landmarks.

Since a spherical joint allows all three rotational DOF, it only requires defining the local joint centre in the body-fixed frame of the two adjacent bodies. On the other hand, both universal and revolute joints demand the definition of axes of rotation about which the bodies rotate. Due to the lack of a consistent dataset, the axes of rotation of the universal and revolute joints were assumed aligned with the direction

axes of the body-fixed reference frames. All joints, their respective proximal and distal bodies, and the information about the centre of rotation are listed in Table 4-3 and pictured in Figure 4-2.

Table 4-3: Anthropometric data scaling parameters for the nineteen kinematic joints in the biomechanical model. The ID corresponds to the numeration in Figure 4-2. The scaling factors for the position of point P are represented in the body reference frame of body *i* (proximal body) and body *j* (distal body).

ID	Name	Type	Body Proximal	Body Distal	Scaling factor for position of point *P* in the body reference frame of body *i* (%)[4]			Scaling factor for position of point *P* in the body reference frame of body *j* (%)[4]		
					ξ	η	ζ	ξ	η	ζ
1	Right Hip	Spherical	Pelvis	R. Thigh	0.2366	-0.2188	0.3616	0.041	0.429	-0.033
2	Right Knee	Revolute	R. Thigh	R. Leg	0.0417	-0.5706	-0.0324	0.048	0.41	-0.007
3	Right Ankle	Spherical	R. Leg	R. Foot	0.0485	-0.5901	-0.0069	-0.382	0.151	-0.026
4	Left Hip	Spherical	Pelvis	L. Thigh	0.2366	-0.2188	-0.3616	0.041	0.429	0.033
5	Left Knee	Revolute	L. Thigh	L. Leg	-0.0417	-0.5706	-0.0324	0.048	0.41	0.007
6	Left Ankle	Spherical	L. Leg	L. Foot	-0.0485	-0.5901	-0.0069	-0.382	0.151	0.026
7	Lumbar	Spherical	Pelvis	Torso	-0.0134	0.1161	0	0.0356	-0.5807	0.0021
8	Right GH	Spherical	R. Scapula	R. Arm	0.0329	-0.0053	0.0046	-0.0029	0.0764	0.0044
9	Right Elbow	Universal	R. Arm	R. Forearm	-0.0185	-0.5277	0.0258	-0.0100	0.417	-0.014
10	Right Wrist	Universal	R. Forearm	R. Hand	-0.0106	-0.5866	-0.0141	-0.082	0.839	-0.074
11	Left GH	Spherical	L. Scapula	L. Arm	-0.0329	-0.0053	0.0046	0.0029	0.0764	0.0044
12	Left Elbow	Universal	L. Arm	L. Forearm	0.0185	-0.5277	0.0258	-0.0100	0.417	0.014
13	Left Wrist	Universal	L. Forearm	L. Hand	0.0106	-0.5866	-0.0141	-0.0820	0.839	0.074
14	Cervical	Spherical	Torso	Neck	0.036	0.42	0.002	0	-0.3944	0
15	Occipital	Revolute	Neck	Head	0	0.6056	0	-0.4563	-0.1748	0
16	Right SC	Spherical	Torso	R. Clavicle	-0.008	-0.0021	0.0181	-0.0007	-0.0094	-0.0407
17	Right AC	Spherical	R. Clavicle	R. Scapula	-0.0007	-0.0094	0.0449	0.0326	0.0189	0.0449
18	Left SC	Spherical	Torso	L. Clavicle	0.008	-0.0021	0.0181	0.0007	-0.0094	-0.0407
19	Left AC	Spherical	L. Clavicle	L. Scapula	0.0007	-0.0094	0.0449	-0.0326	0.0189	0.0449

[4] All percentages relate to the correspondent segment length, except the ones concerning the following joints: right and left glenohumeral (joints number 8 and 11), right and left scapulothoracic (joints number 16 and 18) and right and left acromioclavicular (joints number 17 and 19). In these articulations, the scaling factor for local coordinates of point *P* are related with the subject's height.

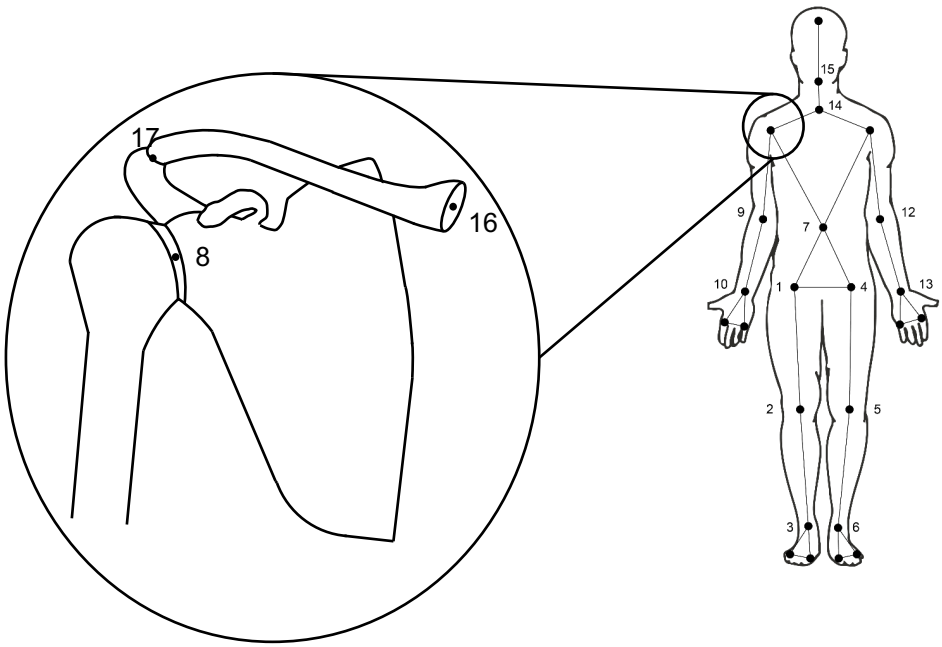

Figure 4-2: Schematic representation of kinematic joints of the full body biomechanical model. The articulations are numbered and represented with a dot.

5. Data Acquisition and Processing

To perform an inverse dynamic analysis, kinematic and kinetic data are required. The first type of data is related to the acquisition of kinematic variables such as linear and angular displacements, velocities, and accelerations, in a laboratorial environment. Displacement data relies on the tracking of a set of anatomical landmarks, from points near joint rotation, limb extremities or strategic landmarks depending on the type of acquisition. The second type of required data is associated with the external forces acting on a certain mechanical system. Both of these data must refer to a consistent spatial reference system (Winter, 2009).

The studied motion, the front crawl swimming technique, was measured experimentally by three-dimensional motion capture systems at the LABIOMEP-UP. The kinematic data were processed and used as input to the motion reconstruction procedure carried out in this work. The kinetic information, in this case, the hydrodynamic forces, was estimated following Sequeira (2021), using the computer simulation software Swumsuit (Nakashima et al., 2007).

5.1. Kinematic Data Acquisition

The experimental data collected at the LABIOMEP-UP involved a 25-year-old healthy male swimmer with a height of 1.80 m and a weight of 70.3 kg. The athlete performed a front crawl swimming stroke for the purpose of data graphic visualization in a 25m indoor swimming pool, i.e., motion was acquired to recreate the front crawl swimming motion through video imaging.

The motion was tracked using a Qualisys Track Manager system (Qualisys, Gothenburg, Sweden) at 100 Hz that relied on 12 above water cameras (3x Oqus 310+, and 9x Oqus 400) and 10 underwater cameras (4x Oqus 300+u, 4x Oqus 700+u, and 2x Oqus 310+u). The 22 cameras were disposed along the swimming pool according to the set illustrated in Figure 5-1. The system was calibrated in three phases, sequentially: the above water cameras were calibrated first; the underwater cameras were calibrated next; and, finally, the two systems were synchronized to allow adequate above and under water measurements (Andersen, 2019). The volume containing the calibrated region was about 28 m^3 (7 m x 2 m x 2 m) and corresponds to the coloured area in the centre of the pool's representation in Figure 5-1. The global reference frame origin is in the midsection of the calibrated volume, at the water surface level, i.e., Z = 0. The orthogonal axes of the global frame define X in the lateral direction, Y in the swimming direction, and Z in the vertical direction.

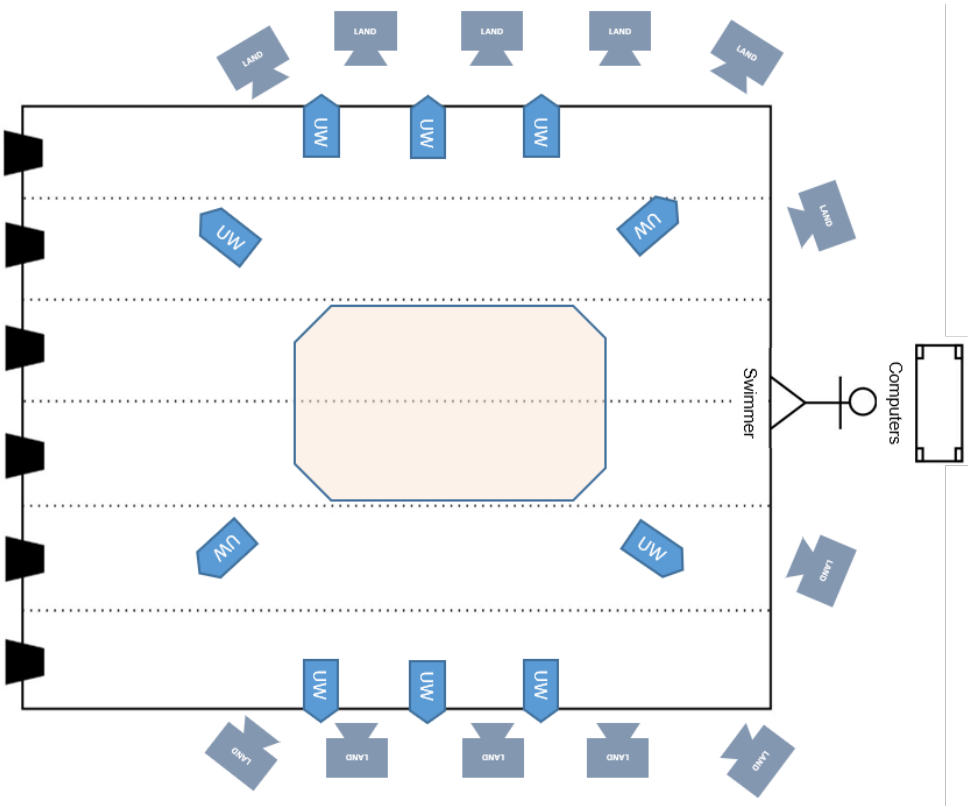

Figure 5-1: Top view configuration of the LABIOMEP-UP layout. UW stands for underwater cameras, and LAND stands for above water cameras. The coloured rectangle in the centre of the swimming pool corresponds to the calibrated volume covered by the 22 cameras.

The swimmer's motion was captured by tracking 66 reflective markers' trajectories placed on anatomical bony landmarks and the the experimental data acquisition comprised a static trial and a dynamic trial:

Static Trial: consisted of a static acquisition for every marker in a standing position, obtained inside the pool, with the pelvis and lower limbs submerged; these static data were collected in the anatomical reference position (ARP).

Dynamic Trial: consisted of trajectory information for every marker in every time step of the front crawl motion, later given as input to the kinematic analysis.

In this type of dual phase acquisitions, motion capture challenges often arise, such as the difficulty in dealing with the light refraction that occurs for underwater measurements, causing some image deformation (Kwon & Casebolt, 2006), and the existence of bubbles caused by the water turbulence, inducing markers' misreading in the air-water interface. The calibration step is vital to decrease the possible errors from the light distortion problems (Monnet et al., 2014). Additionally, due to the dynamic movements of the front crawl technique, some of the markers might be misread or even fall during the acquisition, having to be reconstructed later using spline interpolation (J. T. Andersen, 2019a). To decrease the chance of markers falling, doubled sided tape, as well as hydrophobic tape (Euroderm) and adhesive tape (Omnitape) were used to reinforce markers fixation; the swimmer was also instructed to swim slowly and carefully, considering that this acquisition was for the purpose of data visualization.

5.2. Kinematic Data Filtering

Experimental acquisitions are always subject to high-frequency noise from digital data and motion tracking inaccuracies either due to human flaws, measuring equipment or because there is some sliding of the markers on the skin surface. If these problems are not addressed with adequate post-treatment, the accuracy of output of a dynamic analysis might be compromised (Andersen et al., 2009).

The experimental data acquired in LABIOMEP-UP were provided already treated. A 5-frame Moving Average filtering technique was implemented using the Qualisys Track Manager software. However, when first and second differentiation are considered, Butterworth low pass filters have demonstrated to be more stable and efficient than Moving Average filtering (Crenna et al., 2021). For this reason, the kinematic data were additionally filtered using a 2^{nd} order Butterworth low-pass filter with cut-off frequencies determined through a residual analysis. The optimal cut-off frequency is then selected, avoiding a cut-off frequency that is too high, which allows too much noise to pass with less signal distortion, or too low, which reduces noise but with the cost of increasing signal distortion (Winter, 2009).

5.3. Motion Reconstruction

To assure the consistency between acquired motion data and the proposed biomechanical model, the scaling equations of Dumas et al. (2007a, 2007b) were applied to the anatomical measurements of the human subject described in section 5.1.

According to the experimental protocol for the kinematic acquisition, markers are placed near relevant bony landmarks, often located closely to anatomical articulations, as pictured in Figure A-1. This information, which is subject-specific, is crucial to define consistent joint centres, as well as body-fixed reference frames following ISB recommendations (Wu et al., 2002, 2005)

The LABIOMEP laboratory data set utilized in the current work was acquired for purposes other than the ones of this dissertation, which limited some aspects of the biomechanical modelling – the most relevant of them being the fact that the used protocol did not match the requirements for a proper shoulder rhythm acquisition. Even if there was a chance of conducting a specific experimental acquisition for the current work, it is uncertain how accurate it would be for the kinematics of the clavicle and scapula. In fact, measuring clavicular and scapular kinematics is challenging even on dry land acquisitions, due to soft tissue artefacts (Brochard et al., 2011; van Andel et al., 2009; Xu et al., 2014). Essential to define the anatomical segments' length, most of joint centres – for the elbow, wrist, knee, and ankle joints - were estimated as the midpoint between two reflective markers (Dumas et al., 2007a, 2007b). The joint centre of the shoulders, hips, lumbar, cervical and atlanto-occipital joints, which cannot be accessed by palpation, were calculated using predictive methods consisting in regression equations based on the human subject's anthropometry (Peng et al., 2015).

The hip joint centre (HJC) was estimated according to Hara et al. (2016) in the pelvis reference frame, considering ξ, η, and ζ as the direction axes of the pelvis coordinate system set by Wu et al. (2002), giving:

$$\begin{aligned} &\text{Posterior-anterior direction:} && HJC_{\xi} = 11 - 0.063LL \\ &\text{Inferior-superior direction:} && HJC_{\eta} = -9 - 0.078LL \\ &\text{Medial-lateral direction:} && HJC_{\zeta} = 8 + 0.086LL \end{aligned} \tag{5-1}$$

where LL, expressed in millimetres, is the leg length, defined as the distance from ASIS to the medial epicondyle of the femur (see Figure 5-2).

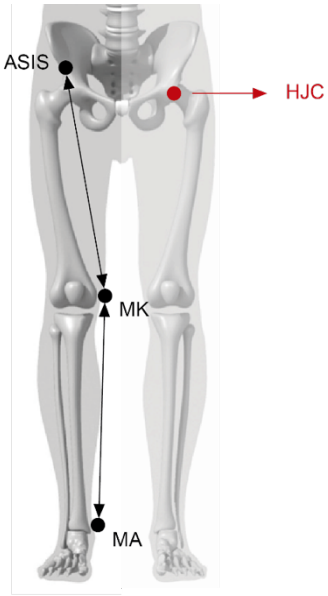

Figure 5-2: Estimation of the hip joint centre. Leg length as the distance from ASIS to medial malleolus (MA) passing through the medial epicondyle of the femur (MK). (Sequeira, 2021)

The lumbar joint centre (LJC) was calculated utilizing pelvic depth and anterior pelvic width as predictors, considering the approach of Murphy et al. (2011). The coordinates of the joint centre are described in the pelvis body-fixed frame as:

$$\begin{aligned} &\text{Posterior-anterior direction:} && LJC_{\xi} = -0.7006PD \\ &\text{Inferior-superior direction:} && LJC_{\eta} = 0.0349APW \\ &\text{Medial-lateral direction:} && LJC_{\zeta} = -0.0045PD \end{aligned} \tag{5-2}$$

where P is the pelvic depth, defined by the distance from the midpoint between RASIS and LASIS to the midpoint between RPSIS and LPSIS, and APW is the anterior pelvic width, characterized by the distance from RASIS to LASIS, both of them depicted in Figure 5-3.

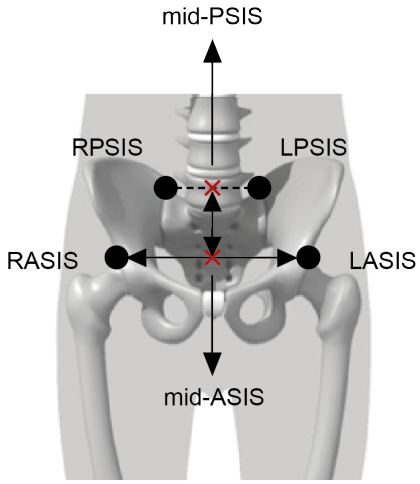

Figure 5-3: Pelvic depth and anterior pelvic width (Sequeira, 2021)

The CJC was computed according to the equations of Reed et al. (1999), using the locations of the 7th cervical vertebrae (C7) and the deepest point of incisura jugularis (ST1), both of them defined in the global reference frame, as the schematics in Figure 5-4 illustrates.

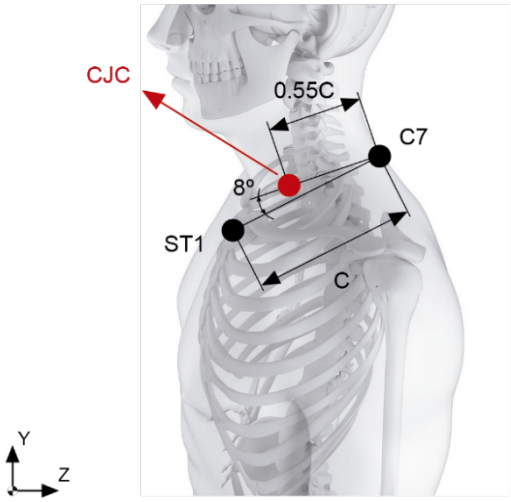

Figure 5-4: Estimation of the cervical joint centre on the sagittal plane, measured in the global reference frame. (Sequeira, 2021)

The shoulder joint centre (SJC) was estimated following the equations suggested by Pàmies-Vilà (2012), which resort to the information of the markers of the right and left acromion, RAC and LAC, and the LJC estimation (Figure 5-5). In the global reference frame, the right and left SJC are estimated as:

$$\begin{aligned} &\text{Right SJC:} && \mathbf{SJC} = \mathbf{r}_{RAC} - 0.02\mathbf{v} - 0.05\mathbf{w} \\ &\text{Left SJC:} && \mathbf{SJC} = \mathbf{r}_{LAC} + 0.02\mathbf{v} - 0.05\mathbf{w} \end{aligned} \tag{5-3}$$

where $\mathbf{r}_{RAC}$ and $\mathbf{r}_{LAC}$ correspond to the coordinates of the RAC and LAC markers, respectively, and $\mathbf{u}$, $\mathbf{v}$, and $\mathbf{w}$ are unitary vectors with the directions indicated in Figure 5-5.

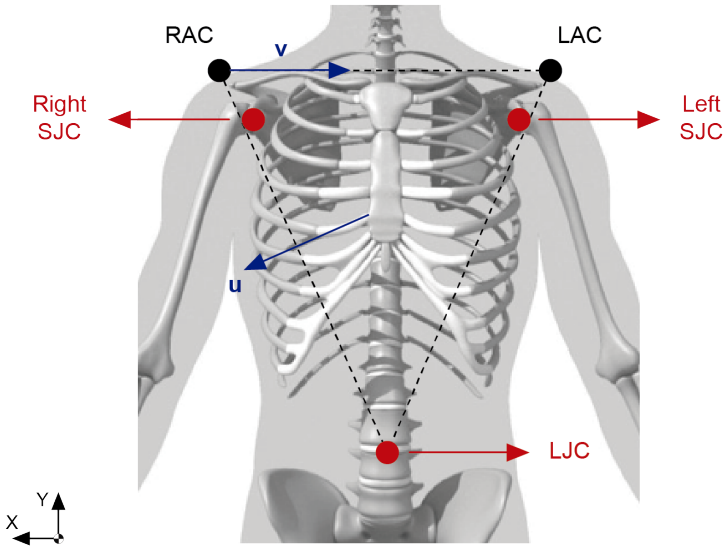

Figure 5-5: Estimation of the shoulder joint centre in the global reference frame. The vector $\mathbf{v}$ goes from RAC to LAC, and $\mathbf{u}$ is the vector perpendicular to the plane defined by LJC, LAC, and RAC. $\mathbf{u}$ and $\mathbf{v}$ are unitary vectors (Sequeira, 2021)

Finally, the OJC was computed using the markers of the top of the head, right head, and left head, according to the following expression (Pàmies-Vilà, 2012)

$$\mathbf{OJC} = 0.5(\mathbf{r}_{RHEAD} + \mathbf{r}_{LHEAD}) - 0.04\mathbf{u} - 0.1\mathbf{w} \tag{5-4}$$

where $\mathbf{r}_{RHEAD}$ and $\mathbf{r}_{LHEAD}$ represent the coordinates of the RHEAD and LHEAD markers, respectively, and $\mathbf{u}$, $\mathbf{v}$, and $\mathbf{w}$ are unitary vectors with the directions indicated in Figure 5-6. The vector $\mathbf{v}$ connects RHEAD to LHEAD, $\mathbf{u}$ is the vector perpendicular to the plane defined by HEADTOP, RHEAD, and LHEAD, and $\mathbf{w}$ is the cross product between $\mathbf{u}$ and $\mathbf{v}$.

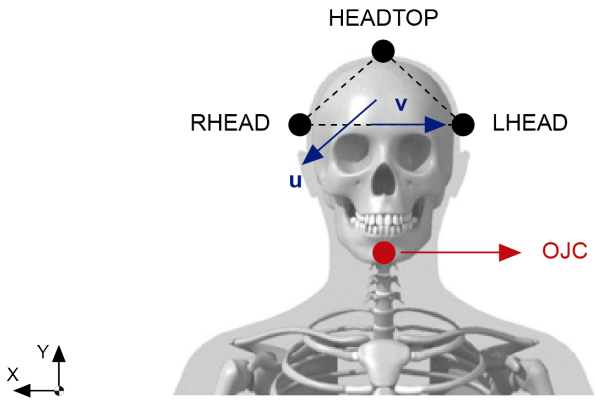

Figure 5-6: Estimation of the atlanto-occipital joint centre in the global reference frame. The vector $\mathbf{v}$ goes from RHEAD to LHEAD, and $\mathbf{u}$ is the vector perpendicular to the plane defined by HEADTOP, RHEAD, and LHEAD. $\mathbf{u}$ and $\mathbf{v}$ are unitary vectors (Sequeira, 2021).

5.3.1. Shoulder Rhythm Estimation

The dynamic tracking of the scapula and clavicle is very challenging (Grewal & Dickerson, 2013). The most common approach used to capture the shoulder rhythm considers skin markers, but even though three bony landmarks can be identified on the scapula, their tracking is limited due to the relative motion between the bony segment and the overlying soft tissue (Brochard et al., 2011; van Andel et al., 2009; Xu et al., 2014). To minimize tracking errors due to soft tissue artefacts during motion, the acromion marker cluster (AMC) method was proposed. This method considers a cluster of markers placed on the acromion, which after a calibration step, is used to reconstruct the motion of the scapula. Although the AMC method enables the dynamic tracking of the scapula, it has been shown to be applicable only up to 100º of humeral elevation, after which the tracking error increases significantly. Its application in an aquatic environment has never been reported. Excluding invasive methods, such as the placement of bone pins, drilled into the scapula, which are quite limited procedures due to their invasiveness, one feasible alternative for the definition of the shoulder girdle motion is the application of predictive statistic models. These regression models (De Groot & Brand, 2001; Grewal & Dickerson, 2013; Xu et al., 2014) are based on the consistent correlation between the orientation of the skeletal elements of the shoulder girdle (van der Helm & Pronk, 1995).

The shoulder rhythm proposed by Xu et al. (2014) uses the orientation of the humerus relatively to the thorax to predict the orientation of the clavicle and the scapula, offering not only the widest range of motion in the literature but also the greatest angular resolution of all methods to date. The considered standardized arm configurations were the following: five planes of elevation (0º, 30º, 60º, 90º, 120º), six elevation angles (0º, 30º, 60º, 90º, 120º, 150º), and seven humerus axial rotation angles (-90º, -60º, -30º, 0º, 30º, 60º, 90º) for the thoracohumeral joint, all of them with a 90º flexed elbow. This envelope of motion does not include certain swimming postures, particularly those that go beyond a plane of elevation of 120º or present negative angles of elevation. Note that during the front crawl technique the shoulder range of motion (ROM) achieves around 180º in flexion, 62º in extension, 44º in horizontal abduction and 140º in horizontal adduction (Beach et al., 1992). The chosen methodology was based on thirty-eight participants – 32.3 (10.8) years, mean height 1.72 m (0.09) and mean weight 72.0 kg (16.6) – with no upper extremity disorders and used the relative orientation of the humerus, obtained from the experimental acquisition at LABIOMEP, as the sole predictor. These regression equations are represented in generic terms as:

$$\begin{aligned} Y = {} & c_1'(\gamma_{HT1} - 46.97) + c_2'(\beta_{HT} + 66.46) + c_3'(\gamma_{HT2} + 37.64) + c_4'(\gamma_{HT1} - 46.97)^2 \\ & + c_5'(\beta_{HT} + 66.46)^2 + c_6'(\gamma_{HT2} + 37.64)^2 + c_7'(\gamma_{HT1} - 46.9)(\beta_{\mathrm{HT}} + 66.46) \\ & + c_8'(\gamma_{\mathrm{HT1}} - 46.97)(\gamma_{\mathrm{HT2}} + 37.64) + c_9'(\beta_{\mathrm{HT}} + 66.46)(\gamma_{\mathrm{HT2}} + 37.64) + \mathrm{K} \end{aligned} \tag{5-5}$$

with c_i', γ_{HT1}, β_{HT}, γ_{HT2}, and K, representing the estimated regression coefficients, the angle of the humerothoracic plane of elevation, the humerothoracic angle of elevation, the angle of axial rotation, and a given constant, respectively. The regression coefficients c_i' are detailed in Table 5-1 for the retraction/protraction of the scapula (γ_S), lateral/medial rotation of the scapula (β_S), anterior/posterior tilt

of the scapula (α_S), retraction/protraction of the clavicle (γ_C), and elevation/depression of the clavicle (β_C).

Table 5-1: Estimated regression coefficients for the predictive equations from Xu et al. (2014)

Y	c'_1	c'_2	c'_3	c'_4	c'_5	c'_6	c'_7	c'_8	c'_9	K
γ_S	0.163	-	0.039	-0.0016	-0.0018	-0,0003	-0.0023	-0.0009	0.0003	38.35
β_S	-0.065	0.322	-0.024	-	-0.0009	-	-	-0.0014	-	-23.20
α_S	0.060	-0.039	-0.011	-	-	0.0002	-	0.0005	0.0008	-7.11
γ_C	0.059	0.207	0.013	-0,0017	-0.0005	-0.0005	-0.0020	-0.0020	-	-17.42
β_C	-0.025	0.204	-0.031	-	0.0002	0.0002	-0.0007	-0.0003	0.0007	-21.04

Although necessary to extrapolate the equations provided by Xu et al. (2014) because the ROM of the swimming clearly exceeds the one predicted by the model, this method was considered the most suitable, covering the widest ROM in the literature.

The humerothoracic angles (HT) that are utilized as input to the regression model that predicts the orientation of the clavicle and scapula (Xu et al., 2014) were also filtered. Since the arm reference frame is defined using the markers of the Lateral and Medial Epicondyles of the Humerus (corresponding to R/L LELB and R/L MELB markers of Figure A-1), the axial rotation is highly sensitive to any perturbation that might occur during the experimental acquisition, justifying the filtering of the HT angles. Similarly to the kinematic data treatment, the HT angles were filtered using a 2nd order Butterworth low-pass filter with the cut-off frequencies determined through a residual analysis (Winter, 2009).

5.4. Kinematic Data Consistency

More often than not, the kinematic motion captured does not fulfil the kinematic constrains associated with the biomechanical model, resulting in constraint violations that affect the intersegmental forces and torques computed by the inverse dynamic analysis (Silva & Ambrósio, 2002). Besides the errors that inherently take part in any experimental acquisition, other factors, such as the scaling procedure applied to match the anthropometric dimensions of the subject under analysis, may lead to non-consistent positions and orientations of the anatomical segments. To prevent this from happening, a kinematic consistency procedure was imposed to the system, comprising (1) the motion reconstruction using the initially irregular positions of the anatomical markers obtained by the motion acquisition and the anatomical segment lengths; (2) the orientation description of each anatomical segment through the definition of the respective local reference frame; (3) the depiction of the time dependent joint angles for every articulation, as well as the position and orientation of the base body, the pelvis, responsible for driving the DOF of the system; (4) the kinematic analysis process to obtain the positions that satisfy the constraints imposed on the biomechanical model. The velocity and the acceleration of the joint angles, as well as the pelvis driver, are computed through direct spline differentiation. The kinematic consistent velocities and accelerations of the biomechanical system are obtained by solving Equations (3-7) and (3-8) from Chapter 3.

5.5. Hydrodynamic Forces Estimation

Swimming is considered to be a very demanding sport with enormous challenges when it comes to performance boosting. From a fluid dynamics point of view, thrust needs to be enhanced and drag cut down to allow athletes to swim faster and ultimately break records. Therefore, determining hydrodynamic forces is a major step to address performance enhancement. However, the inherently difficult task of measuring external forces in an aquatic environment hampers the process of assessing swimming motion. Other engineering applications involving fluid dynamics, such as ship hydrodynamics, commonly use computational simulations, such as computational fluid dynamics (CFD), to minimize drag and maximize thrust, optimizing hull geometries and propeller designs. When it comes to swimming, however, this approach is not linear: measuring devices are limited in aquatic environments and the movement of a flexible and articulated human body is computationally challenging to deal with (Sato & Hino, 2013). This makes computational simulations, namely CFD or smoothed particle hydrodynamics methods (SPH), too time-consuming and inefficient to operate in large-scale parameter studies (Takagi et al., 2016), which is the case of the current biomechanical model.

Nakashima et al. (2007) addressed this limitation by proposing an analytical model called Swumsuit. Their methodology considers a simplified configuration of the human body and computes the hydrodynamic forces acting on each body segment. While considering unsteady-state effects that are especially relevant in cases with high body accelerations (Honda et al., 2012), it provides a satisfying approximation of the external forces acting on the whole body with little computational effort (Nakashima et al., 2007, 2012), making it suitable for the type of analysis considered in this dissertation.

Swumsuit models the human body as a series of twenty-one body segments shaped like truncated elliptic cones, as illustrated in Figure 5-7:

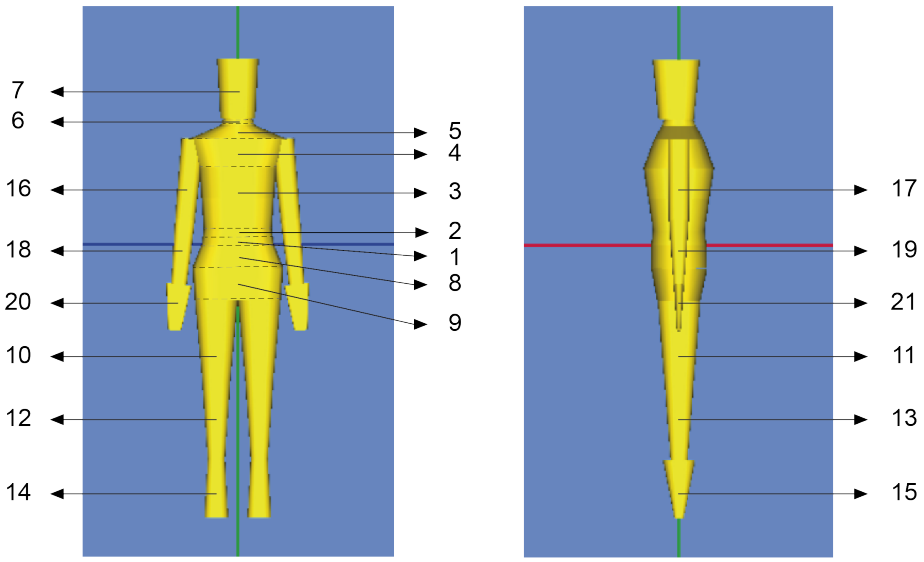

Figure 5-7: SWUM model topology: 1 – lower waist, 2 – upper waist, 3 – lower breast, 4 – upper breast, 5 – shoulder, 6 – neck, 7 – head, 8 – upper hip, 9 – lower hip, 10 – right thigh, 11 – left thigh, 12 – right shank, 13 – left shank, 14 – right foot, 15 – left foot, 16 – right upper arm, 17 – left upper arm, 18 – right forearm, 19 – left forearm, 20 – right hand, and 21 – left hand.

The unsteady fluid force components acting on each truncated elliptic cone, schematized on Figure 5-8, account for the inertial force due to added mass of fluid (Fa), normal (Fn) and tangential (Ft) drag forces, and buoyancy (Fb), which includes the gravitational forces.

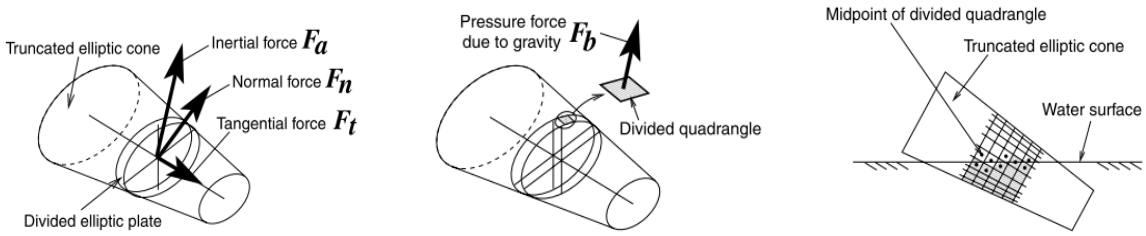

(a) (b) (c)

Figure 5-8: Analytical modelling of the fluid forces in Swumsuit (adapted from Nakashima et al. (2007)): (a) Fluid force components acting on a thin elliptic plate's centre (except buoyancy), (b) buoyancy is calculated by integrating the pressure force on divided quadrangles, and (c) decision on whether quadrangles are above or below the water surface.

To estimate inertial force, and normal and tangential drag components without solving the flow field, Swumsuit resorts to the local kinematics of each part of the human body, at each instant of time, and force coefficients, Ca, Cn, and Ct, respectively, which were estimated experimentally by the authors. Each truncated elliptic cone is divided into thin parallel elliptic plates along the longitudinal axis, and all fluid force components except buoyancy are applied at the centre of the thin elliptic plates. Buoyancy is determined by integrating the pressure force due to gravity, acting on the side surface of each thin elliptic plate, discretized into small quadrangles along the circumferential direction (see Figure 5-8 c). This information is compiled and input to the Swumsuit analysis engine in the form of nine files, each containing data of body geometry, joint motion, analysis settings, and the absolute body motion (three linear and three angular velocities of the whole-body COM) at all instants of time of the stroke cycle. Once the simulation process ends, the global forces acting on each body segment are output.

Swumsuit is a valuable tool to estimate hydrodynamic forces, but before using it, additional processing steps are required to consistently 1) create the required inputs according to the SWUM model discretization and formulation and 2) post-process the output data for the application of the obtained forces and moments in the body segments of the current model. Sequeira (2021) developed an interface that generates the coherent input for the Swumsuit software entirely based on the biomechanical model and its kinematic consistency and, after the simulation, treats the engine's outputs so that they match biomechanical body in use.

Swumsuit requires four types of input files to estimate the hydrodynamic forces: 1) the body geometry data file, with information about the swimmer's body topology and anthropometric characteristics; 2) the joint motion data file, describing the orientation of all anatomical segments during the complete stroke cycle; 3) the linear and angular velocities data file, reporting the linear and angular velocities of the

swimmer's body as a whole and 4) the analysis settings data file, with information about the analysis parameters and the system's initial conditions.

Since the SWUM model and the current biomechanical model have different discretization levels, a relationship had to be established between the two. Sequeira (2021) defined a relationship between a biomechanical model composed of 16 rigid bodies (with a direct correspondence to the current model except for bodies 17-20, right and left clavicles and right and left scapulae) and the SWUM model, composed of 21 rigid bodies. For the sake of simplicity, this work follows the same equivalence defined by Sequeira (2021) and assumes the right and left clavicles and scapulae have no direct forces applied.

After running the simulation, the force data outputs are converted from SWUM model to the current biomechanical model resorting to the relationship between body segments and by applying the consistent rotation matrices to transform forces in all three components from SWUM to the biomechanical global frames. The local moments are also determined from the Swumsuit outputs.

To summarize, the interface between the full body biomechanical model and the simulation software proposed by Sequeira (2021) addresses (1) the conversion of body geometry specifications and motion data, which is given as input to the simulation, and (2) the processing of the simulation output data containing the external forces, that are addressed to the full body model. A generic overview of this interface can be found in Figure 5-9.

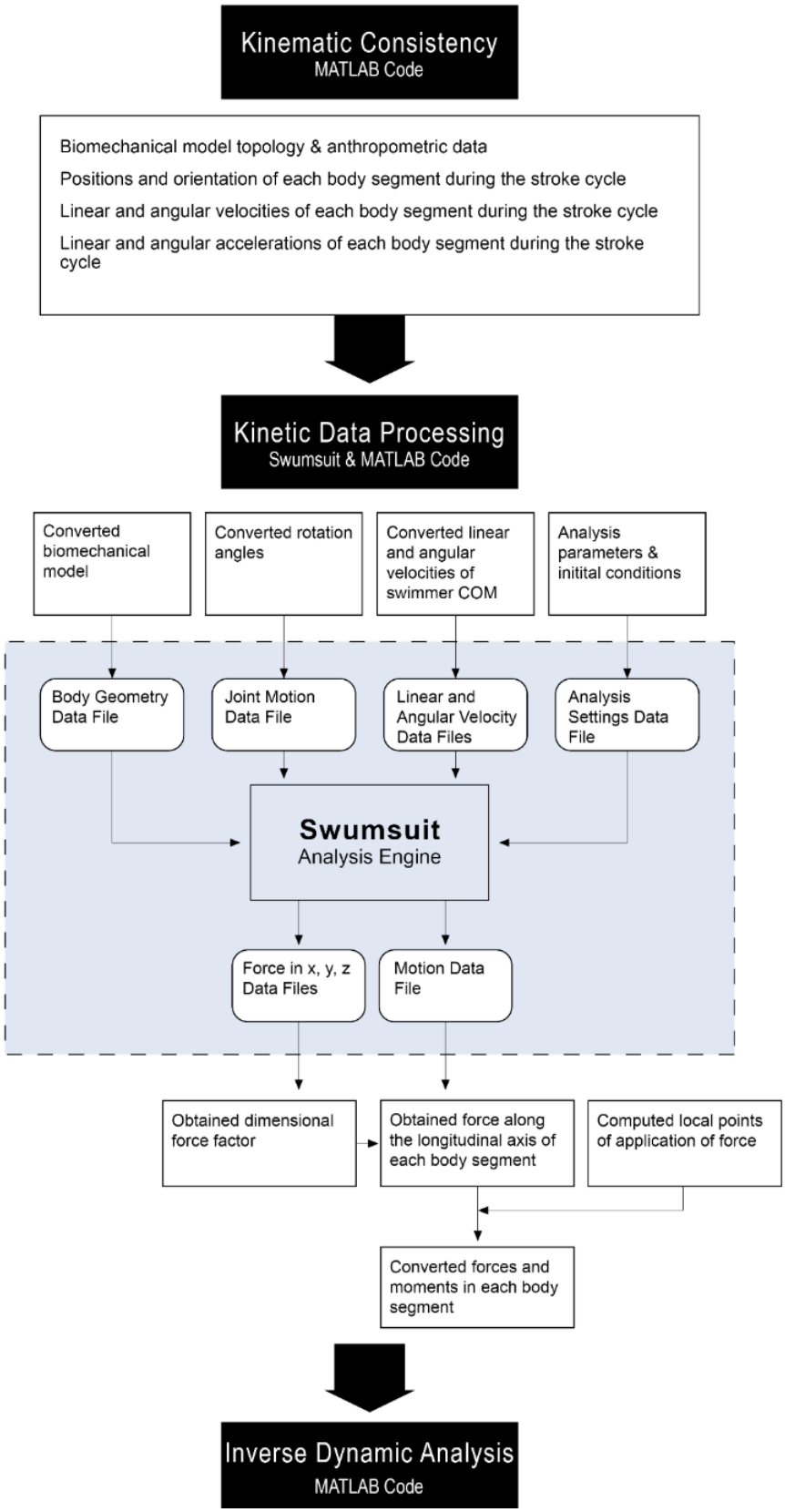

Figure 5-9: Data flow of the interface between the simulation software Swumsuit and the current biomechanical model. The blue shaded rectangle represents the simulation analysis that is performed in Swumsuit. (Sequeira, 2021)

5.5.1. Joint Motion Reconstruction Procedure

One of the limitations raised by Sequeira (2021) about the former procedure was the difficulty converting the orientation of the anatomical segments, defined in Euler parameters and obtained after the kinematic consistency procedure, into an admissible Swumsuit input file following an Euler angles approach. Given the high complexity of segmental movements during swimming and the intrinsic limitations of this formulation, discontinuities in the rotation angles are expected for some time intervals, especially on body segments with wide ROM, which might compromise the estimated hydrodynamic forces. Additionally, the angular conversion methodology proposed by Sequeira (2021) included a segment-specific approach, i.e., not all bodies considered the same rotation sequence, nor had the same number of rotations. To address these limitations, a more robust and standardized procedure to convert Euler parameters to Euler angles is proposed here.

The Swumsuit simulation software represents the relative body motion through sequential rotations of body segments about their own body coordinate system ($O_b - x_b y_b z_b$), located at the proximal joint of each body. When the reference position is set, all rotations are null and the SWUM model has the upper limbs raised upwards, the trunk and lower limbs straight, and the feet pointing downwards, as pictured in Figure 5-10.

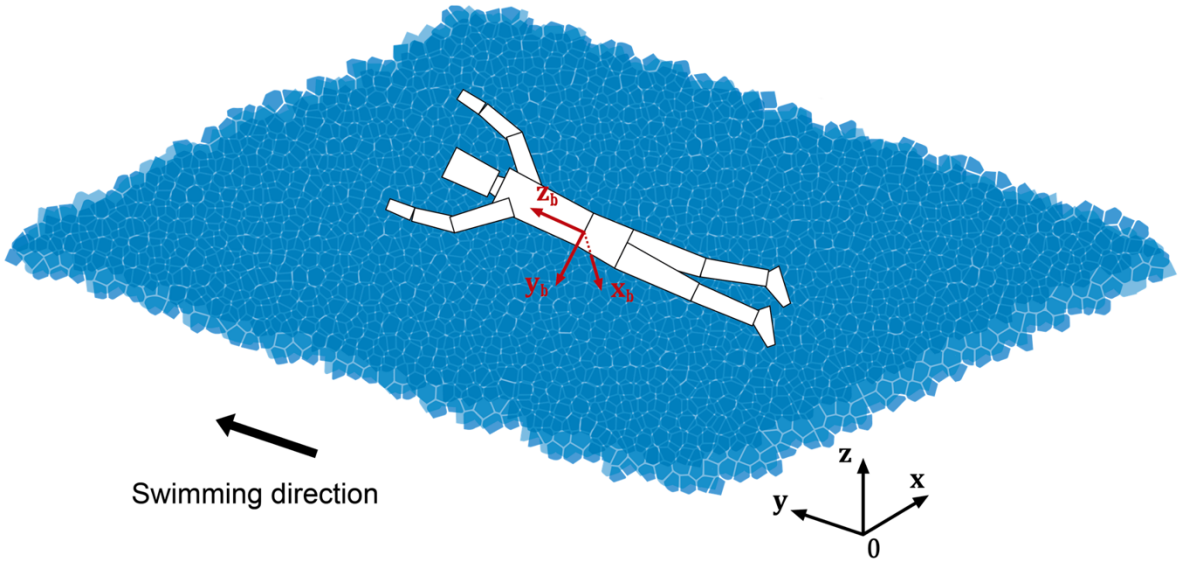

Figure 5-10: Representation of SWUM coordinate systems: absolute coordinate system ($O - xyz$) and body coordinate system ($O_b - x_b y_b z_b$). The global coordinate system in which the LHBM is defined is parallel to $O - xyz$. In this figure, one single body coordinate system is represented in red, although in SWUM each body has its own reference frame fixated at the proximal joint. (Sequeira, 2021)

The sequence of rotations employed to describe the rotation of each body segment matters. Swumsuit defines each rotation relatively to a reference frame that is fixed on the proximal joint before the movement starts. Moreover, SWUM rotations are defined sequentially, based on two chains: the upper

and the lower chains. These two chains are ordered from proximal to distal segments and are linked to one another at the whole-body centre of mass (COM), which is located at the lower tip of the lower waist segment (Nakashima et al., 2007). The upper chain (UC) begins at the lower waist segment and connects all bodies until the extremities of the upper body – head and right and left hands. Analogously, the lower chain (LC) is defined from the upper hip all the way down to the feet. Both UC and LC are shown in Figure 5-11. This consecutive mechanism necessarily implies that the motion of a given body depends on the orientation of the body linked upstream.

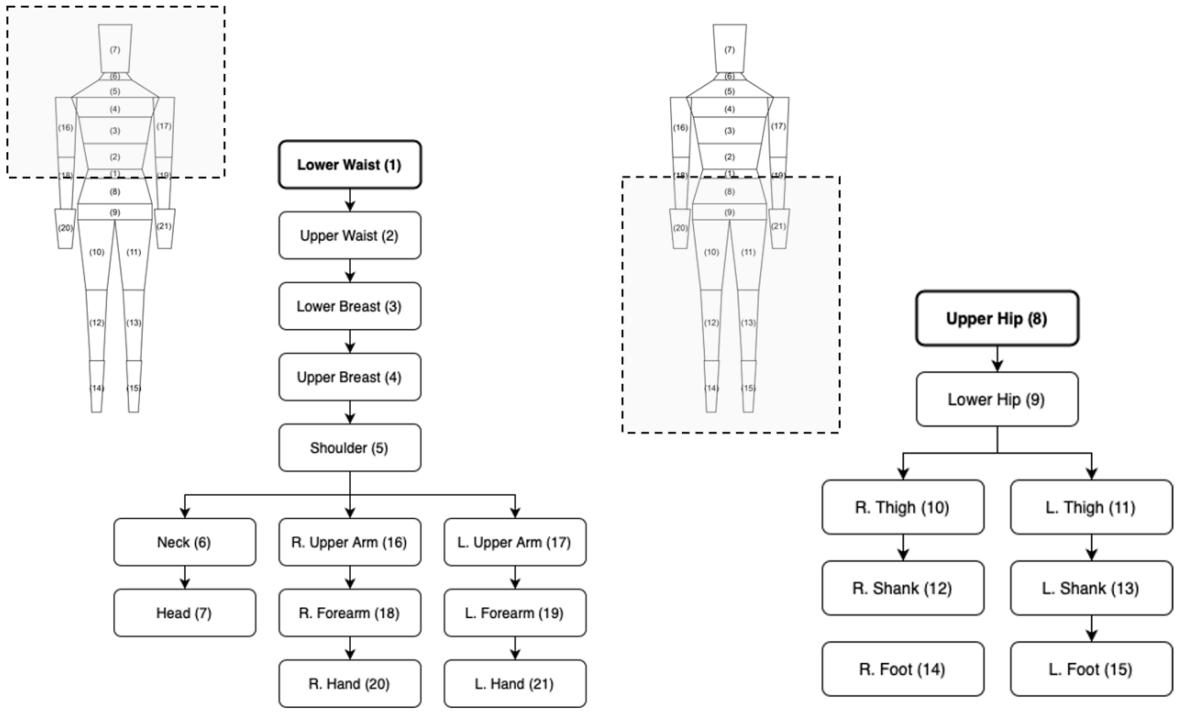

Figure 5-11: Schematic representation of upper and lower chains in Swumsuit. Each chain is ordered from proximal to distal segments. The numbers of the body segment in the SWUM model are indicated in between curly brackets. The shaded area represents, from left to right, the upper and lower body regions which are covered by the sequence.

To define a robust and systematic transformation of the four Euler parameters, obtained after ensuring kinematic consistency, into rotation angles, the following procedure was developed. The orientation of each SWUM body segment is calculated in the global reference frame of Swumsuit, $\mathbf{R}_{\mathrm{SWUM}}$:

$$(\mathbf{R}_{\mathrm{SWUM}})_i = (\mathbf{R}_{\mathrm{Model}})_j \times (\mathbf{R}_{\mathrm{SWUM2Model}})_i \tag{5-6}$$

where $\mathbf{R}_{\mathrm{Model}}$ represents the orientation of each body j in the global reference frame of the current model, calculated by directly converting Euler parameters into their corresponding rotation matrix, and $\mathbf{R}_{\mathrm{SWUM2Model}}$ represents the orientation of the SWUM body j defined in the body-fixed reference frame of the corresponding body in the current model. These matrices are computed by establishing an initial rotation matrix that relates the orientation of each body-fixed coordinate system $O_b - x_b y_b z_b$ in SWUM

with the local frame of each corresponding body j in the current model, both of them in the reference position depicted in Figure 5-10.

Each SWUM joint allows 3 rotational DOF defined relatively to its predecessor body, bearing in mind the above defined UC and LC. For the purpose of this joint motion reconstruction methodology, all rotations are assumed to occur sequentially and in the same order ZYX.

For every body of the chain except for the root, the orientation of the body downstream, $\mathbf{R}_{\text{Child Body}}$, is defined relatively to the orientation of the body upstream, $\mathbf{R}_{\text{Parent Body}}$, i.e., the difference between the configuration of the parent body (proximal) and child body (distal) is a transformation representing a sequence of three consecutive rotations $(\theta_3, \theta_2, \theta_1)$ about ZYX. This transformation can be computed through the following objective problem:

$$\min f\,(\theta_1, \theta_2, \theta_3) = \sum_{\substack{i=1,3 \\ j=1,3}} \mathbf{B}_{\text{ij}}{}^2$$

$$subject\ to \quad \begin{cases} -\pi \leq \boldsymbol{\theta_1} \leq \pi \\ -\dfrac{\pi}{2} \leq \boldsymbol{\theta_2} \leq \dfrac{\pi}{2} \\ -\pi \leq \boldsymbol{\theta_3} \leq \pi \end{cases} \tag{5-7}$$

where $\mathbf{B}_{\text{ij}}$ represents the relationship between the orientation of the child body and the parent body, given by:

$$\mathbf{B}_{\text{ij}} = \mathbf{R}_{\text{Child Body}} - \mathbf{R}_{\text{Parent Body}} \times \left[\mathbf{R}_{\text{x}} \times \mathbf{R}_{\text{y}} \times \mathbf{R}_{\text{z}}\right] \tag{5-8}$$

with $\mathbf{R}_{\text{x}}$, $\mathbf{R}_{\text{y}}$ and $\mathbf{R}_{\text{z}}$ representing the rotation matrices that characterize elemental rotations by θ_1, θ_2 and θ_3 around X, Y and Z axes, respectively:

$$R_x(\theta_1) = \begin{bmatrix} 1 & 0 & 0 \\ 0 & \cos\,\theta_1 & -\sin\,\theta_1 \\ 0 & \sin\,\theta_1 & \cos\,\theta_1 \end{bmatrix},\ R_y(\theta_2) = \begin{bmatrix} \cos\,\theta_2 & 0 & \sin\,\theta_2 \\ 0 & 1 & 0 \\ -\sin\,\theta_2 & 0 & \cos\,\theta_2 \end{bmatrix},$$

$$R_z(\theta_3) = \begin{bmatrix} \cos\,\theta_3 & -\sin\,\theta_3 & 0 \\ \sin\,\theta_3 & \cos\,\theta_3 & 0 \\ 0 & 0 & 1 \end{bmatrix} \tag{5-9}$$

The optimization problem was solved in MATLAB using the *fmincon* function. By default, this optimization scheme uses an interior-point algorithm to find the minimum of a constrained nonlinear multivariable function. After computing the optimized sequence of $\theta_3, \theta_2, \theta_1$ angles for each SWUM body, the input data file *joint_motion.dat* is written considering that the rotation of the parent body must also be given to the child body segment(s) to ensure an overall consistent motion. The whole methodology is summarized in Figure 5-12.

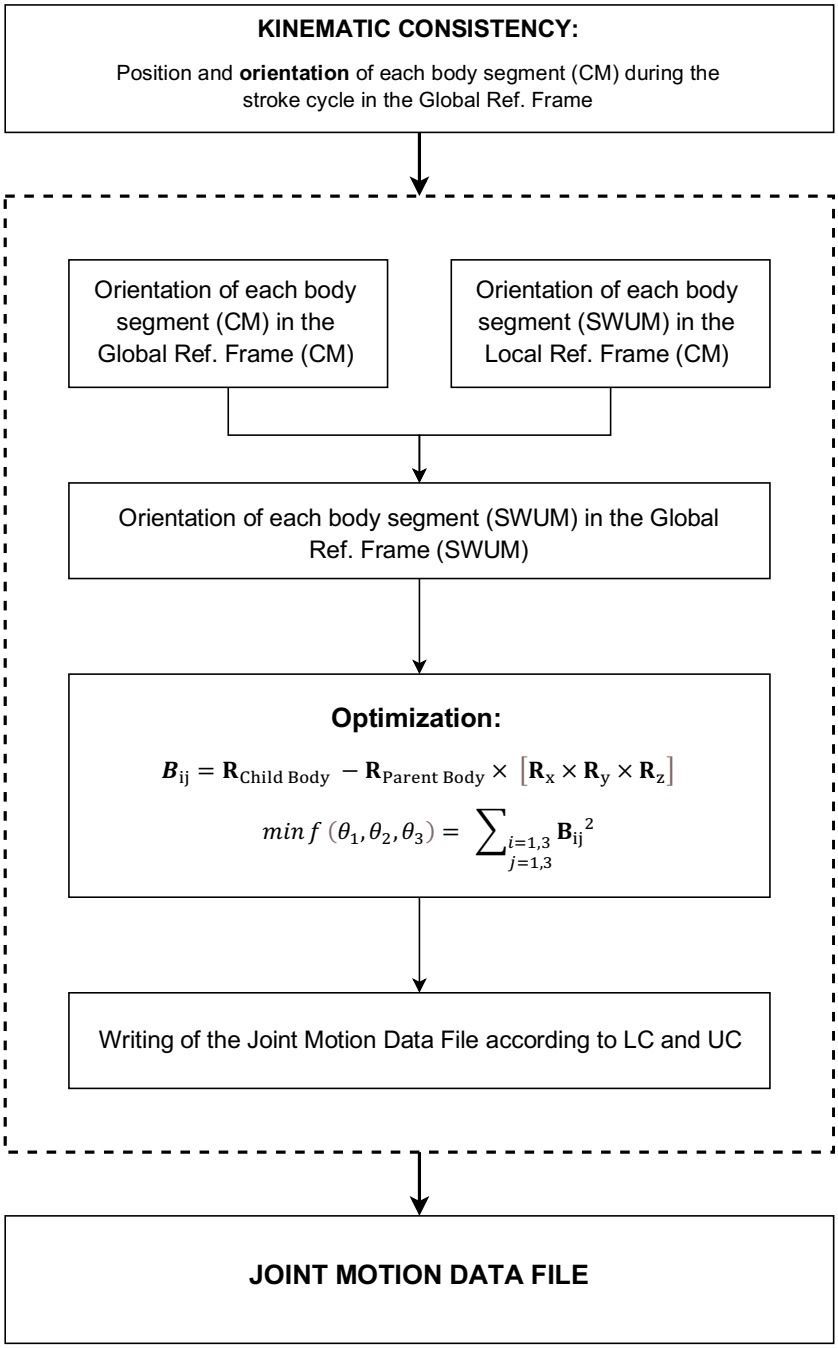

Figure 5-12: Flow Chart representing the joint motion reconstruction procedure based on the orientation of each body segment after kinematic consistency is achieved. The kinematic data from the current model (CM) functions as an input to the process.

To verify the output of this new procedure, the obtained hydrodynamic forces were compared to those found in literature (Nakashima et al., 2007; Sequeira, 2021) for a given anatomical segment, in this case, the right foot. The results, detailed in Figure 5-14, show the same overall trend shown by Sequeira (2021), but using a much more standardized and robust procedure.

(a)

(b)

(c)

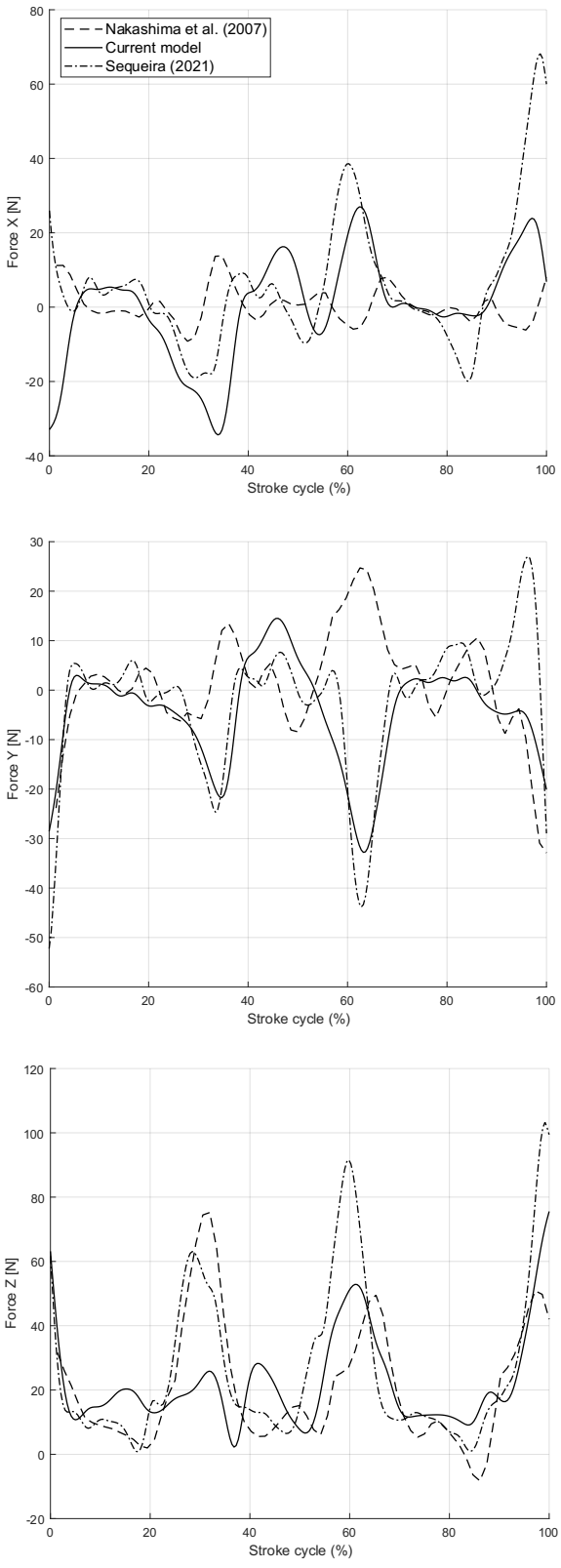

Figure 5-14: Hydrodynamic forces estimated during a left-hand six-beat front crawl swimming stroke cycle, which is defined as the period between consecutive entries of one same hand into the water. Comparison with the results obtained by Sequeira (2021) and Nakashima et al. (2007) in the X, Y, and Z components (a, b and c, respectively). The horizontal axis corresponds to the percentage of the stroke cycle.

Sequeira (2021) identified three force peaks in the vertical component Z, each acting approximately at 28%, 60%, and 99% of the stroke cycle, which are consistent with those identified in the current work, and correspond to the downbeat of the right foot, moving towards the bottom of the swimming pool a few instants before, approximately at 20%, 51%, and 90%.

The obtained forces also demonstrate overall agreement with the ones computed by Nakashima et al. (2007), with slightly increased magnitudes. A possible explanation could be the difference between the front crawl swimming techniques under evaluation. The kinematic data of the present work captured the motion of a swimmer performing the hip-driven technique, which is commonly used to take stress off the shoulders, providing additional hip rotation to increase the propulsive power whith a lower stroke rate. The propulsive forces generated during the underwater leg kick are mostly produced in the downbeat movement, which results from the combined action of the hip flexion, followed by knee extension, and ankle plantarflexion (Keys, 2010). Thus, the combined rotation of the whole swimmer's body to the left side and the downbeat movement of the right leg could result in a higher force peak, when compared to magnitudes computed by Nakashima et al. (2007).

5.5.2. Kinetic Data Filtering

Hydrodynamic forces estimated using the simulation software Swumsuit were also filtered using the same procedure described for the kinematic data filtering. Despite not being measured quantities, they were estimated based on a relationship between two different models (the current model and SWUM) and calculated by translating a series of parameters from the present model into admissible Swumsuit inputs, which could induce minor inconsistencies. The role of the 2nd order Butterworth low-pass filter, with cut-off frequencies calculated through a residual analysis (Winter, 2009), was to remove any possible noise introduced by the adopted procedure.

6. Swimming Motion Analysis

In this chapter, the overall results from the swimming analysis are presented, including a brief comparison between the impact of having a classic shoulder model versus a detailed shoulder model. The solution of the determinate inverse dynamic analysis of the six-beat front crawl swimming motion performed at LABIOMEP-UP is also presented. Being a determinate inverse dynamic analysis, the DOF of the multibody system are actuated upon by driver actuators at the joints, instead of muscles. These results are merely indicative and intend to provide some clues about the biomechanical modelling, having low physiological significance. However, they represent the combined action of the muscles about the joints during a specific human motion, thus providing clues on the biomechanical modelling requirements. The highlighted results correspond to the main joints of the upper extremity, namely the glenohumeral, sternoclavicular, acromioclavicular, elbow and wrist joints.

6.1. Application to the Front Crawl Swimming Stroke

The results of the simulation performed in Swumsuit of the six-beat front crawl swimming motion are presented in Figure 6-1 for nine sequential events of the stroke cycle with the corresponding percentage of the total stroke cycle time. The fluid forces acting on the swimmer's body segments, except buoyancy, are represented graphically as red vectors indicating magnitude and direction.

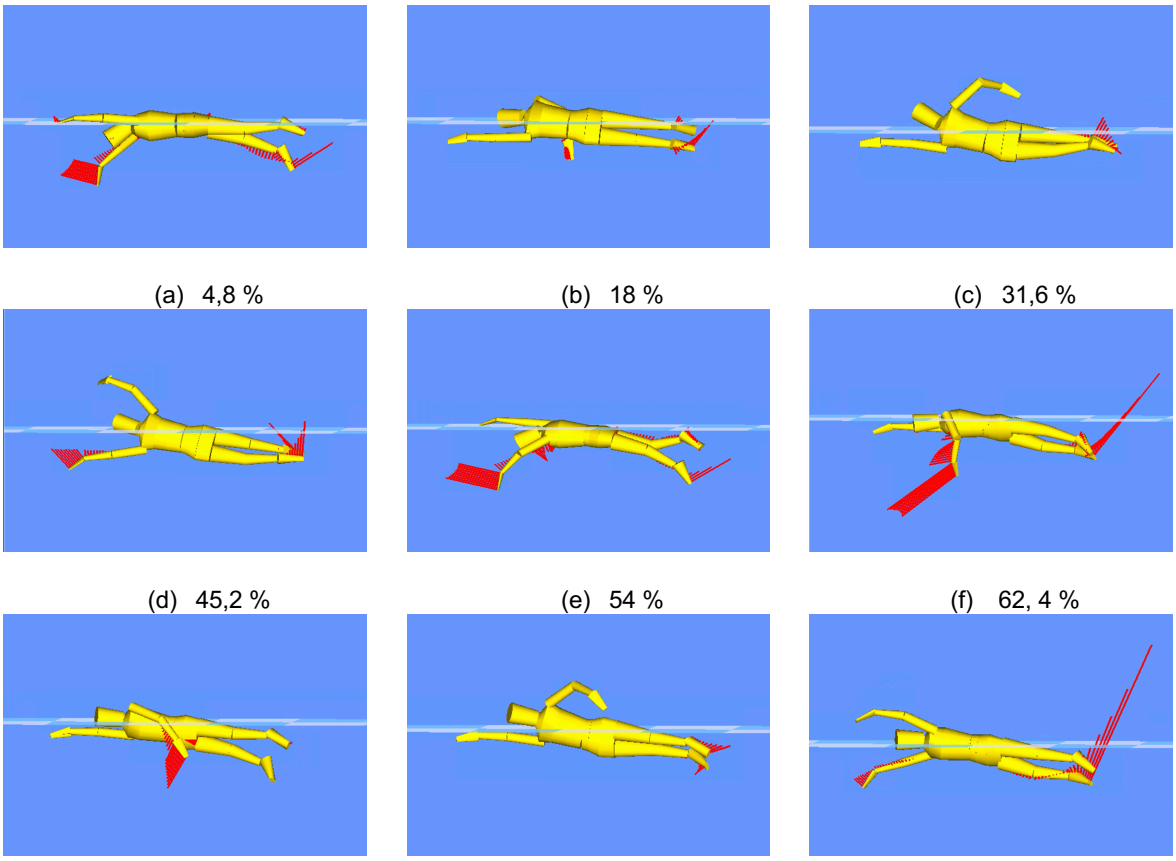

(a) 4,8 % (b) 18 % (c) 31,6 %

(d) 45,2 % (e) 54 % (f) 62, 4 %

(g) 71,2 % (h) 80,8 % (i) 98 %

Figure 6-1: Simulation results of the left-hand six-beat front crawl stroke in Swumsuit (lateral view). The nine events are identified by the corresponding percentage of the total cycle time.

The stroke cycle is characterized as the period between consecutive entries of one same hand into the water (Andersen, 2019) and, in the case of the front crawl technique, it can be divided into three phases: pull phase, push phase and recovery (Maglischo, 2003). The pull phase includes the entry and stretch and the downsweep movements and the push phase is subdivided in insweep and upsweep. The complete front crawl cycle and its segmentation is represented in Figure 6-2:

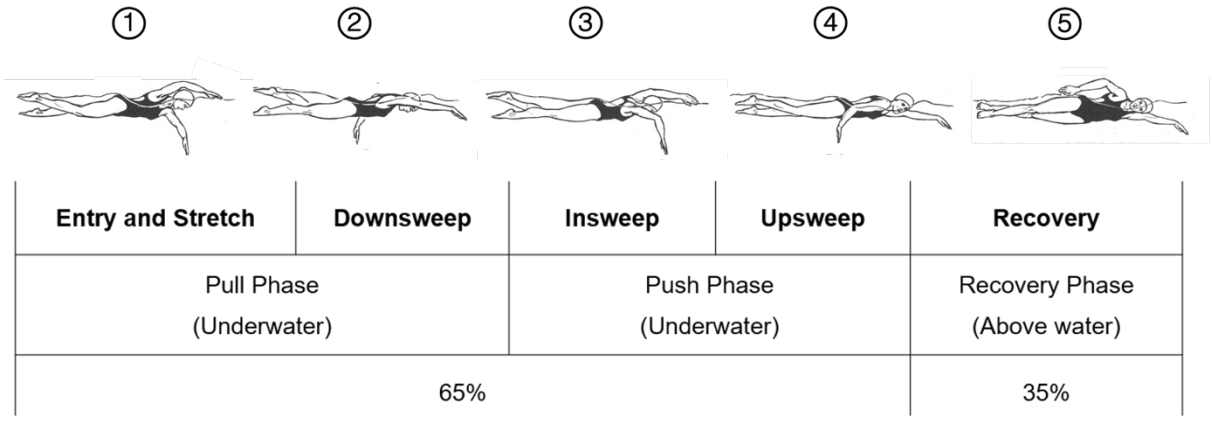

Figure 6-2: Front crawl swimming stroke phases. The figure illustrates one full stroke cycle for the right hand (adapted by Sequeira (2021) from Ceccon et al. (2013)).

In the first stage of the movement, and with the adequate technique, the hand entry demands the maximum elevation angle of the shoulder. The swimmer uses body roll to expand the normal range of motion of the shoulder, providing maximum forward reach and setting up the swimmer to attain maximum thrust. The downsweep starts right after the hand finishes water entry and ends when it reaches the deepest point, where the insweep begins. The arm and forearm are completely vertical, pointing to the bottom of the pool, and the palm of the hand faces backwards. This is one of the most propulsive stages. The second is the next phase, the upsweep, where the hand starts moving outwards and upwards, until the hand gets out of the water (a small part of this last underwater phase may be considered a recovery underwater phase). In fact, although both pull and push phases are predominantly propulsive, most of the thrust is generated in the push phase (Chollet et al., 2000; Maglischo, 2003; Samson et al., 2017; Suito et al., 2007). During these stages, the arm achieves maximum internal rotation, adduction and also abduction force, later on. The chest muscles act as major sources of propulsion in the insweep phase, whereas in the final stage, the recovery, where the hand exits the water, the muscular complex around the shoulder promotes humeral adduction, bringing the arm out. The same muscular complex promotes shoulder stabilization, namely by balancing the scapula and the humerus, during hand exit and entry stages. In the recovery stage, the shoulder abducts and externally rotates as the arm is brought forward for another stroke cycle. The maximal relative external humeral rotation is achieved with the arm out of the water and in an extended, or sometimes hyperextended, position swinging the forearm forward in preparation for hand entry at full extension.

Table 6-1: Major stroke phases, alongside with keys events, during the left stroke cycle evaluated in LABIOMEP-UP.

Stroke phase	Time [s]	Time [%]	Description
Entry and Stretch	0.00	0	Left hand enters the water
	0.06	2.5	Left foot reaches top as right foot reaches bottom of kick
	0.18	7.5	Right hand reaches the deepest point
	0.54	22.6	Left foot reaches bottom as right foot reaches top of kick
	0.78	32.6	Right hand exits the water
Downsweep	0.96	40.2	Left foot reaches top as right foot reaches bottom of kick
	1.01	42.3	Left hand starts moving downwards
	1.16	48.5	Right hand enters the water
	1.28	53.6	Left foot reaches bottom as right foot reaches top of kick
Insweep	1.37	57.3	Left hand reaches the deepest point
	1.62	67.8	Right foot reaches bottom of kick
Upsweep	1.73	72.4	Left hand moves outwards
	1.75	73.2	Left foot reaches top of kick
Recovery	1.95	81.6	Left hand exits the water
	2.18	91.2	Left foot reaches bottom as right foot reaches top of kick
	2.39	100	Left hand imminent to enter the water

6.1.1. Classic Shoulder Model and Detailed Shoulder Model Comparison

In this subsection, the results obtained for a classic shoulder model are compared with those of the detailed shoulder model proposed in this study. The classic shoulder approach models the shoulder joint simply as a spherical joint that connects the humerus to the thorax, whereas the detailed shoulder model considers the clavicle and the scapula. This second approach, despite not representing the closed loop chain, includes the AC joint, connecting the scapula and the clavicle, the SC joint, linking the clavicle and the sternum, and the glenohumeral joint (shoulder joint), here coupling the humerus to the scapula. Modelling the shoulder girdle in a more discretized manner allows a better, more accurate representation of the shoulder rhythm, which can be seen as a clear advantage to understand the shoulder behaviour in the swimming context.

The shoulder plays an important role in all these stages, particularly by providing, jointly with the elbow, the major sources of propulsion in the front crawl. In fact, 85% - 90% of total body propulsion is provided by the upper limb (Guignard et al., 2019; Pink & Tibone, 2000). The wide mobility of the shoulder complex is highly responsible for this and is a major advantage (Beach et al., 1992; Weldon & Richardson, 2001), particularly for competitive swimmers. In fact, when compared to leisure swimmers, professionals demonstrate an increased adduction and internal rotation strength (Beach et al., 1992). Besides, by granting the arm more forward elevation, the swimmer's body can be almost parallel with the water surface, minimizing the surface area and reducing drag (Troup, 1999; Weldon & Richardson, 2001). Another implication of this increased range of motion is the greater stroke length, which directly affects velocity in a positive manner, ultimately improving performance (Chollet et al., 1997). The upside

of the shoulder complex flexibility is reduced glenohumeral stability, induced by the increasing ligamentous laxity, frequently causing dislocations or shoulder pain. This situation is particularly aggravated in the case of elite swimmers, that spend 20 to 30 hours in the pool every week in endurance training (Weldon & Richardson, 2001).

The wide-range mobility of the shoulder complex is due to the combined action of the SC, AC and GH joints, counterbalanced by the stabilizing role of the musculotendinous and ligament complex of the shoulder (Tovin, 2006; Veeger & van der Helm, 2007) and, in the case of the swimming front crawl movement, is enhanced by the effect of the body roll (Psycharakis & Sanders, 2008).

The joint angles for the shoulder joint during the front crawl movement are illustrated in Figure 6-3. The plots show the influence of modelling the shoulder joint as a spherical joint that connects the humerus to the torso (classic model) and the impact of having a glenohumeral ball-and-socket type of joint, linking the arm to the glenoid cavity of the scapula (detailed shoulder model). The obtained angles were computed in sagittal, frontal, and transverse planes, corresponding to the angles that drive the joint: a positive angular variation represents the arm's withdrawal, and a negative variation characterizes the arm approximation. The shoulder ROM for each movement is systematized in Table 6-2.

Table 6-2: Shoulder ROM for the movements occurring in the sagittal, frontal and transverse planes. Comparison between the computed ROM for the Classic Shoulder Model and the Detailed Shoulder Model

		ROM (degrees)	
	Shoulder Movement	Classic Shoulder Model	Detailed Shoulder Model
Sagittal Plane	Flexion	53	71
	Extension	66	102
Frontal Plane	Adduction	75	73
	Abduction	84	73
Transverse Plane	Internal Rotation	134	107
	External Rotation	134	77

(a)

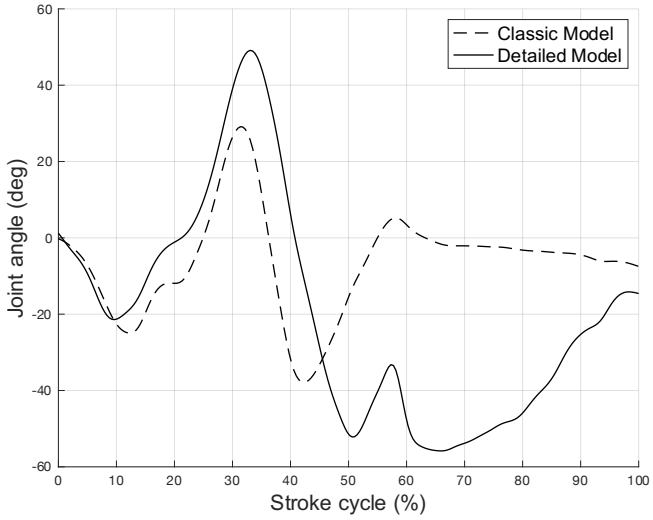

(b)

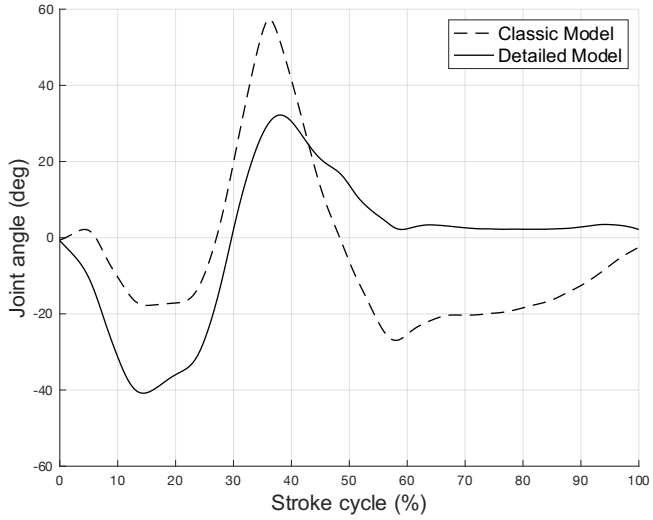

(c)

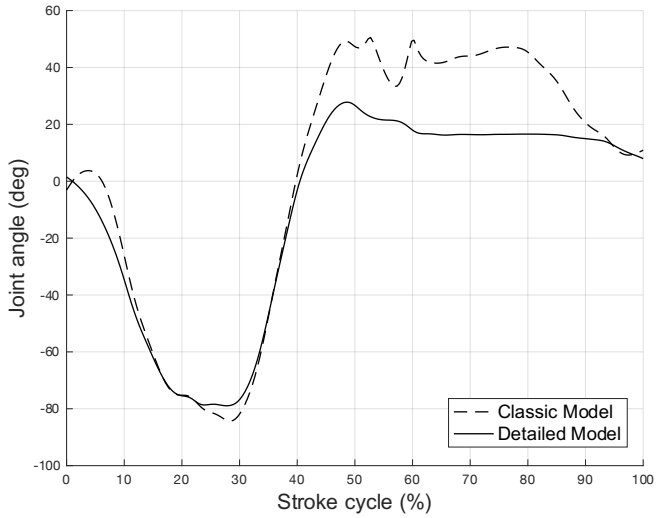

Figure 6-3: Joint angles obtained during left-hand six-beat front crawl swimming stroke cycle in the right shoulder joint for movement of a) flexion/extension b) abduction/adduction c) internal/external rotation. The dashed line represents the results obtained with a classic shoulder model, whereas the continuous line embodies the results achieved with the detailed shoulder model.

Although these angles are merely indicative, some qualitative remarks regarding the attained range of motion as well as the overall angular evolution may be relevant. The kinematic angles from both models have a matching tendency in terms of angular monotony, with the detailed shoulder model presenting globally lower ranges of motion. In the detailed model, all three shoulder complex joints (SC, AC and GH) contribute to the overall range of motion, with the glenohumeral angle contribution being only part of the shoulder joint angle from the classic model.

During the entry and stretch phase, which is about 54%-58% and marks the beginning of the pull phase, a noticeable peak on the shoulder elevation angle is evidenced in (a) in the classic model approach, having only a slightly bump in the detailed shoulder curve. At this stage, the shoulder should present its maximum elevation (Tanghuizi & Toshimasa, 2016), but the measured peak is outspanned by the one achieved during the recovery phase. From 58%-100% and until 9% of the left stroke, the downsweep movement takes place for the right upper limb. In this stage, the propulsive action starts and almost all the angles stabilize: the arm appears to remain stretched forwards but starting to move downwards to the bottom of the pool in a compound effect of shoulder extension and internal rotation movement. Then, the stage where most of the propulsive power is generated, insweep stage, starts around 9% of the left stroke cycle with the shoulder adducted and with a neutral internal rotation. At the end of the upsweep stage, from around 18% to 28%, the shoulder is internally rotated and fully adducted and is ready to get out of the water. Finally, at the recovery phase, which comprehends the period between 28%-54%, the shoulder extends and abducts and externally rotates at the end of it, promoting maximal relative external humeral rotation.

6.2. Upper Limb Velocity

Swimming velocity can be characterized by two variables: stroke length (SL) and stroke frequency (SF). SL can be described as the horizontal distance that the body travels during a full stroke cycle, whereas SF corresponds to the number of full stroke cycles performed within a unit of time ($strokes \cdot min^{-1}$) or Hertz (Hz). Changes in swimming velocity are determined by the combined effects of SF and SL, with:

$$v = SL \cdot SR \tag{6-1}$$

with v as the linear velocity of the swimmer excluding effects of the start, turns, and finish (Toussaint et al., 2006). The SF and the SL are dependent from the limb's kinematics. For instance, the increased shoulder range of motion allows for greater SL, which directly correlates with swim speed (Chollet et al., 1997). Deschodt et al. (1996) suggested that, as the upper limb's velocity increased, the horizontal velocity of the swimmers increased as well, ultimately leading to an increased performance.

Given this performance impact, it is relevant to relate the upper limb's velocity profile and to connect the obtained results with the obtained joint reaction forces and joint torques. Figure 6-4 establishes a comparison between two velocity profiles for the right hand during a left front crawl stroke upper limb action. The velocity peaks detected at around 10% and 23% of the stroke cycle correspond to the stages where most propulsion is generated during the front crawl movement (Barbosa et al., 2013) and are correlated with the generated hydrodynamic forces when the movement occurs inside the water.

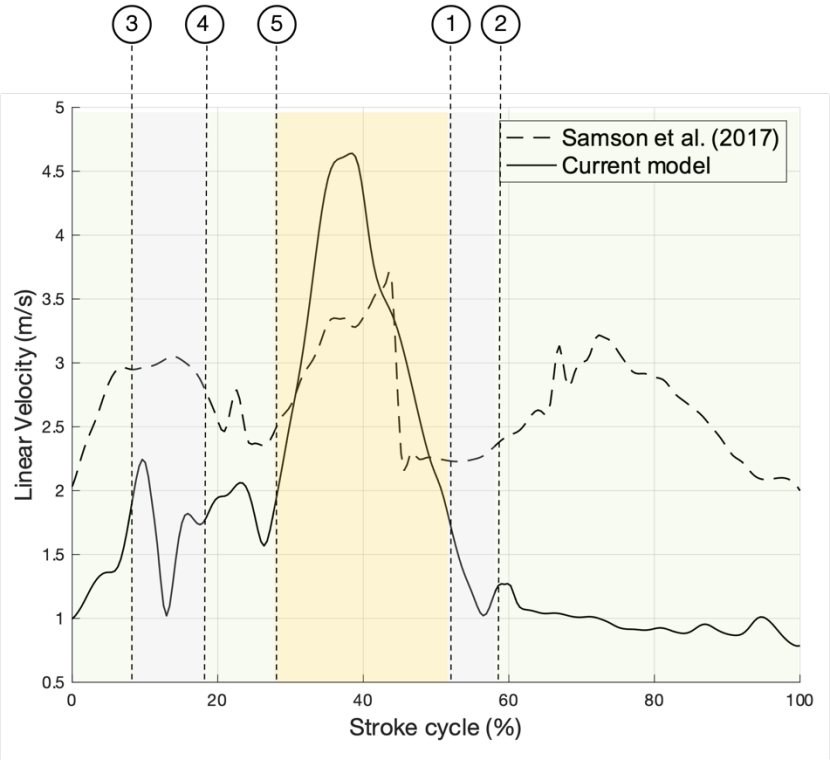

Figure 6-4: Right hand linear velocity for the right hand during the six-beat front crawl swimming motion comparison. The dashed and continuous lines represent the results obtained by Samson et al. (2017) and by the current model, respectively.

Measuring forward velocity indicates when and to what extent certain stages of the stroke cycle are propulsive (Maglischo et al., 1989). Overall, the current model shows a substantially lower instantaneous velocities than the ones computed by Samson et al. (2017). In the curve for the current model, the first two velocity peaks (10% and 23% of the stroke cycle) correspond to the most propulsive phase of each arm, namely the push phase and the third peak to the recovery phase, where the arm is out of the water. A possible explanation might be related to the different type of movement under evaluation: while Samson et al. (2017) simulated a competitive swimmer in sprint pace, the analysis using the current model was based on kinematic data from the LABIOMEP that was acquired for visualization purposes. The first two peaks correspond to the push phase (insweep and upsweep) and recovery, respectively. A third peak can be identified in the velocity profile presented by Samson et al. (2017), corresponding to the downsweep phase, having no direct correspondence on the velocity profile obtained using the current model. However, this discrepancy could be related to the difference between swimmers' technique, with the swimmer in the LABIOMEP performing the downsweep movement with possibly less vigour.

6.3. Inverse Dynamic Analysis

The solution of the determinate inverse dynamics analysis is shown and discussed here. The intersegmental forces obtained during the six-beat front crawl swimming motion are shown in Figure 6-5 for the joint reaction forces of the right wrist, elbow and shoulder for both the classic and the detailed approaches; the intersegmental forces in the sternoclavicular and acromioclavicular are also presented in Figure 6-6. The intersegmental joint torques that are responsible for the movements in the sagittal, transverse and frontal planes are depicted in Figure 6-7 for the right shoulder considering the classic and the detailed model, and in Figure 6-8 a) and Figure 6-8 b) for the right elbow joint and for the right wrist articulation, respectively. The torques acting on the SC and AC are also presented in Figure 6-10 to better understand the impact of modelling the shoulder as a simple ball-and-socket joint (classic model) versus considering a discretized shoulder complex incorporating two additional joints (detailed model).

Actual joint contact forces are often many times superior to the corresponding external forces acting on a given biomechanical segment. In fact, the joint contact joint forces depend on the combined effects of the external forces, in this case, the hydrodynamic forces, plus the active joint forces necessary for controlling joint motion (Derrick et al., 2020; Scott & Winter, 1990). Despite having no physiological significance, the intersegmental forces can be analysed from a qualitative point of view. In both classic and detailed approaches, three peaks can be identified, corresponding to the downsweep movement in the end of the entry and stretch phase, the upsweep movement in the push phase and the beginning of the entry phase, respectively. The recovery phase, approximately between 28% and 54% of the stroke, present close to zero joint reaction forces since the upper limb is out of the water in that stage. Because of the fluid density differences in the transition from the aquatic to the aerial environment, the force acting on the arm decreases by around 800 times (Keys, 2010).

(a)

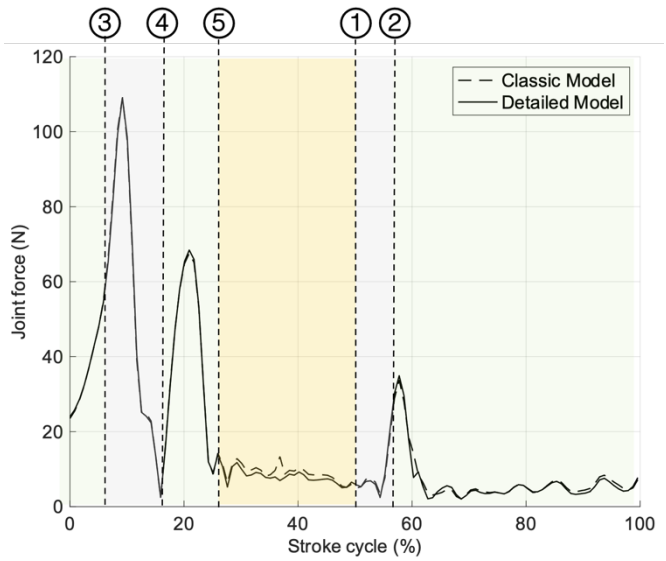

(b)

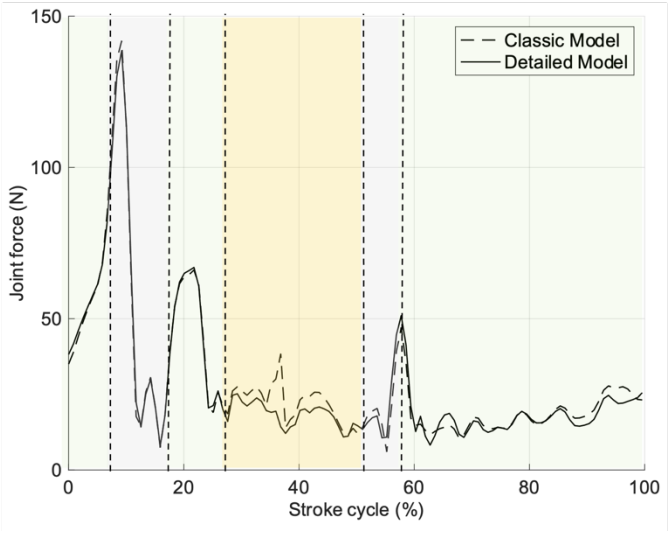

(c)

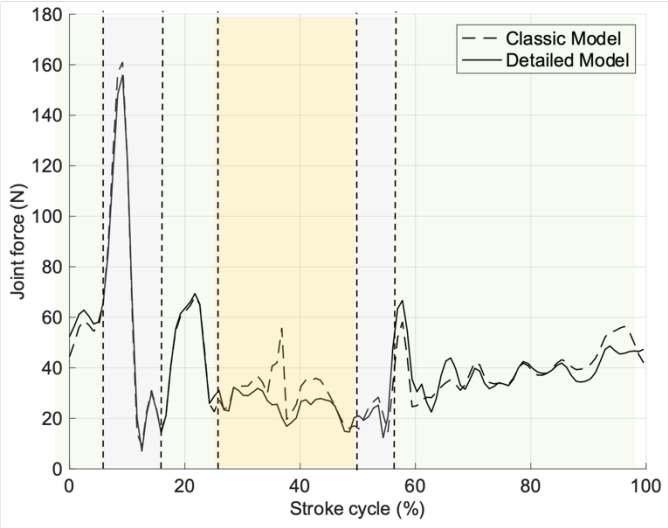

Figure 6-5: Intersegmental forces obtained during a left-hand six-beat front crawl swimming stroke cycle in the right a) wrist b) elbow and c) shoulder. The dashed and continuous lines represent the results obtained with a classic shoulder model and a detailed shoulder model, respectively.

The shoulder discretization has little or no effect on the intersegmental forces, that show minor differences between the two models. The highest force peaks are around 161 N in the shoulder joint, 142 N in the elbow joint and 109 N in the wrist joint and correspond to the insweep stage (9%-18%), the most propulsive stage. Right after, and still within the push phase, the second largest force peak is perceived, consistent with the second largest propulsive generation moment.

The AC intersegmental force, depicted in Figure 6-6, performs similarly to the previously mentioned upper limb articulations, having the largest peak of about 156 N in the insweep stage, a second one at upsweep stage and the last one happening in the entry and stretch period. With a dissimilar behaviour, the SC joint appears to have greater influence in the insweep stage but, furthermost, in the recovery period, registering the most significant peak in this stage, of 59 N.

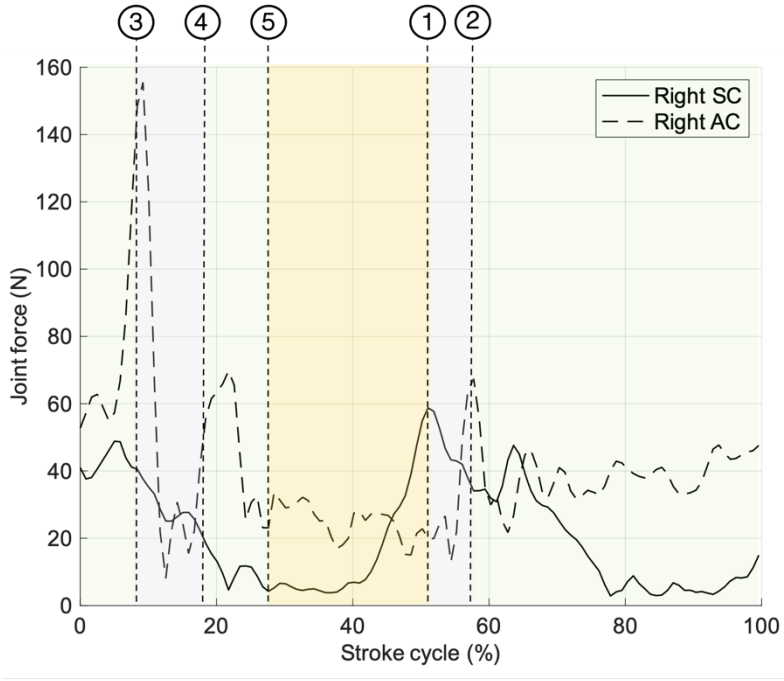

Figure 6-6: Intersegmental forces obtained during left-hand six-beat front crawl swimming stroke cycle in the right sternoclavicular (continuous line) and acromioclavicular (dashed line) joints.

For the sake of clarity, the joint toques depicted in Figure 6-7, Figure 6-8 and Figure 6-10 are represented in direct association with the biomechanical movements they induce, i.e., the joint torque around the sagittal axis promotes a movement in the frontal plane, the joint torque around the longitudinal axis stimulates a movement in the transverse plane and the joint torque around the frontal axis induces the movement in the sagittal plane. For instance, in the case of the shoulder articulation, the joint torque acting around the sagittal axis induces the movement of adduction/abduction (frontal plane), the joint torque around the longitudinal axis stimulates the movement of internal/external rotation (transverse plane) and the joint torque acting around the frontal axis motivates the movement of flexion/extension (sagittal plane).

(a)

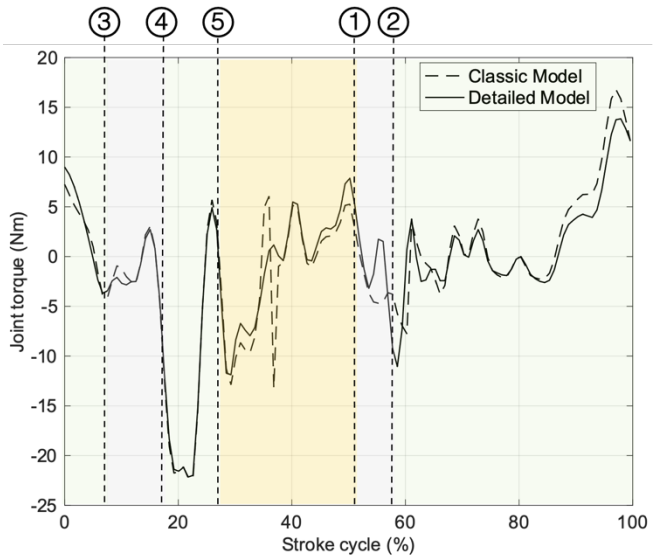

(b)

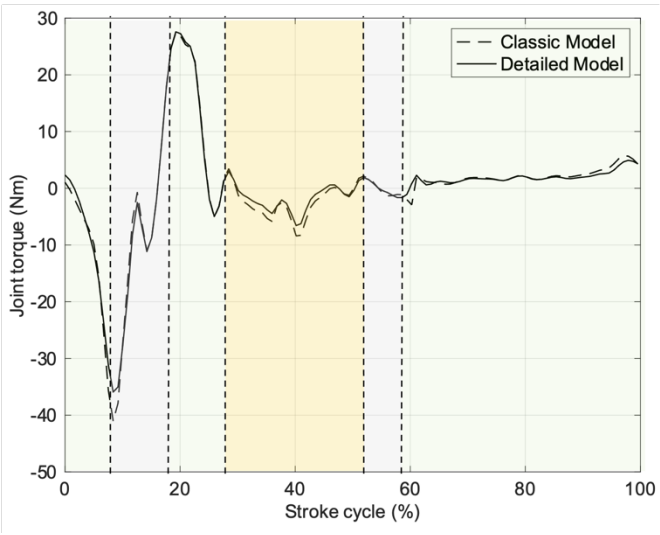

(c)

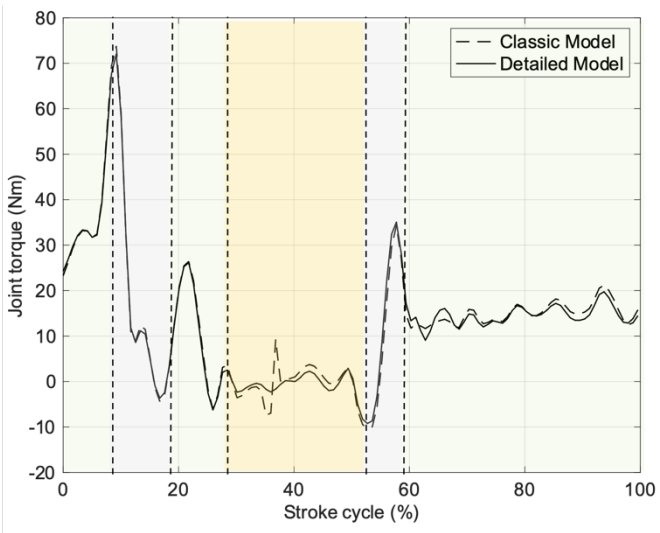

Figure 6-7: Joint torques obtained during left-hand six-beat front crawl swimming stroke cycle for the right shoulder. The represented joint torques are responsible for the right shoulder movements in the a) sagittal, b) transverse and c) frontal planes.

(a)

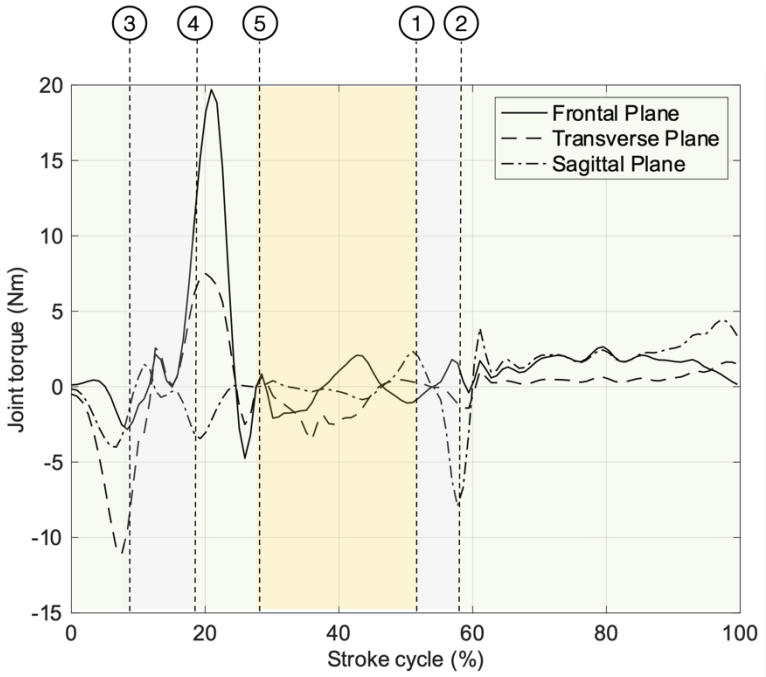

(b)

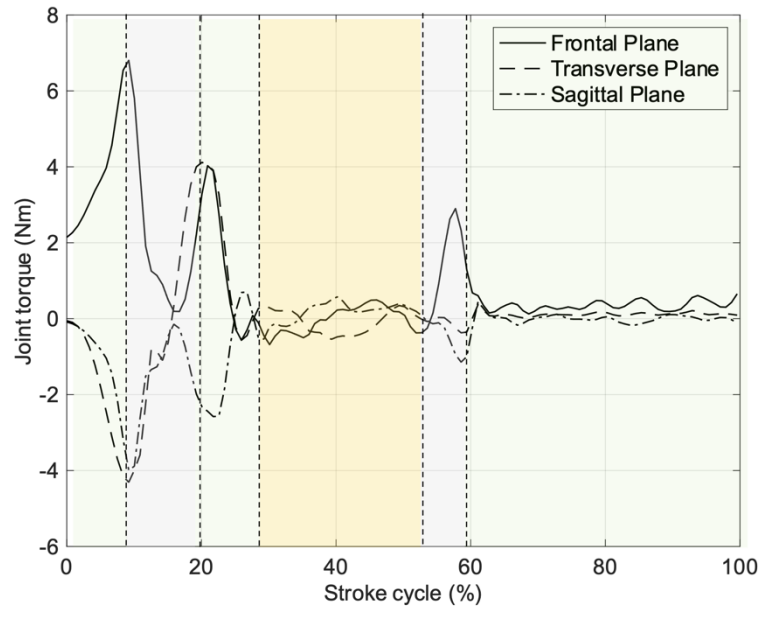

Figure 6-8: Joint torques obtained during left-hand six-beat front crawl swimming stroke cycle the right a) elbow b) wrist. The represented joint torques are responsible for the movements in the sagittal (dashed-dotted line), transverse (dashed line) and frontal (continuous line) planes.

During the entry and stretch stage (54%-58%), the swimmer sets up the arm and body to produce as much thrust as possible: the body roll begins at hand entry, the elbow achieves maximal extension, having a pronounced valley in the sagittal plane of about -8 Nm during this period. The glenohumeral joint is marginally externally rotated and abducted, which is confirmed by the negative joint torque value inducing the movement in both transverse and frontal planes (Figure 6-7). The scapula starts abducted but soon adducts and rotates downward. Throughout the downsweep (58%-100%; 0%-9%), the glenohumeral joint flexes and the body rolls, partially promoted by the shoulder roll; at the end of this phase, the glenohumeral joint starts adducting, which is supported by the valley of about -35 Nm (detailed shoulder model) found in the first instants of the left stroke cycle pictured in Figure 6-7. During the insweep phase (9%-18%), when the upper limb does most of the work in propelling the body forward using the resistance of the water, the glenohumeral joint is adducted, internally rotated, and extended, as the elbow progresses from flexion to extension (from 1.8 Nm to -3.5 Nm). The upsweep stage (18%-28%) contemplates the glenohumeral movement of extension, adduction and internal rotation in the sagittal, frontal and transverse planes; assuming that the scapular plane the scapula denotes a downward movement of rotation and adduction, confirmed by the AC joint torques that induce the motion in the transverse plane (always positive, achieving a peak at 28 Nm) and in frontal plane (predominantly positive, reaching a peak of about 28 Nm). At the end of this phase, the body progressively returns to the horizontal swimming position with the arm close to the water surface. The final stage of the stroke, the recovery phase (28%-54%), is conducted above the water. The arm movement is induced by a slight glenohumeral abduction and external rotation, as evidenced by the -5 Nm (maximum abduction moment in this period) and -9 Nm (maximum external rotation moment in recovery). In the beginning of the recovery phase, the elbow extends, and the scapula rotates downward and adducts. From mid-recovery until the end of the cycle, the glenohumeral joint continues to be externally rotated beyond the neutral position and slightly abducts, achieving its maximum relative abduction right before the hand entering the water for another cycle; the scapula protracts and rotates upward. Right at the end of the recovery, the body returns to the fully horizontal swimming position and is ready to initiate the next stroke (Davies et al., 2009; Richardson et al., 1980).

Harrison et al. (2014) used a coupled Biomechanical-Smoothed Particle Hydrodynamics (B-SPH) model to calculate the resultant joint torques for the arms of a male swimmer performing the front crawl stroke. The swimmer was modelled as a three-dimensional mesh that moved and deformed to match the video footage of the swimming stroke. The articular system of the upper limb comprised shoulders, elbows and wrists, all modelled as spherical joints with 3 DOF. This study shows that the resultant torque is approximately zero during the recovery phase and vestigial in the entry phase, which seems to support the results shown in Figure 6-9. The largest peaks are consistently detected in the wrist, elbow and shoulder joints and occur approximately at the end of the downsweep stage (during the pull) and in the mid-push phase (at the end of the insweep and in the beginning of the upsweep), overall agreeing with the results found by Harrison et al. (2014). However, a significant difference is found in the magnitude of the resultant torques when comparing the results of the present work and to those obtained by Harrison et al. (2014). As discussed in Section 6.2, the lower velocities achieved in this study by the hand, compared to the literature, likely explain this difference. The fact that the motion obtained at

LABIOMEP was intended for visualization purposes promoted a slow swimming stroke, with low overall velocities because the swimmer described open, wide movements while simultaneously trying to avoid the detachment of markers. Harrison et al. (2014) simulated a male swimmer in print pace, therefore obtaining larger peak values and overall resultant joint torques on average.

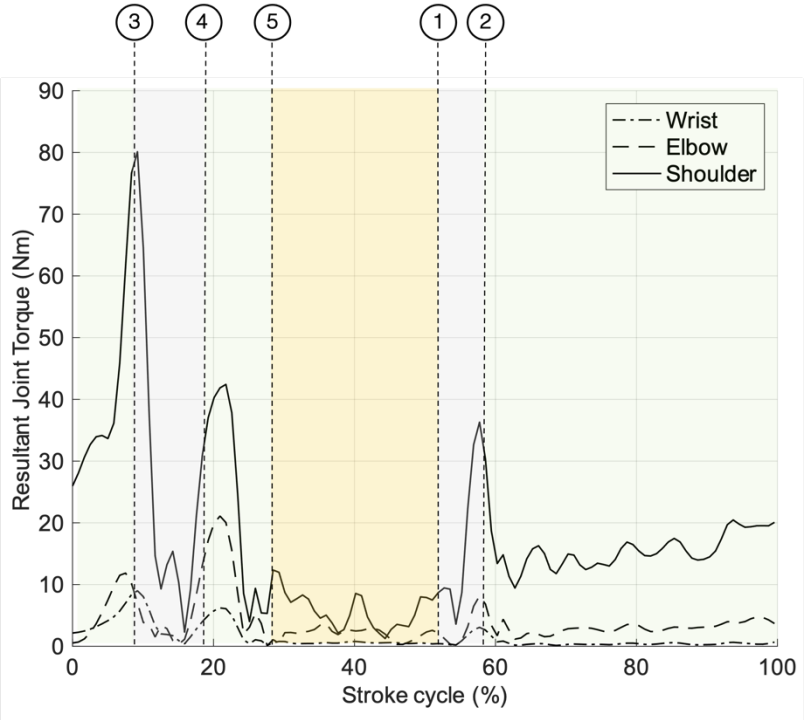

Figure 6-9: Resultant joint torques obtained during left-hand six-beat front crawl swimming stroke cycle in the right shoulder, elbow and wrist. The dot-dashed line depicts the resultant joint torque profile for the wrist joint, the dashed line represents the results obtained for the elbow, and the continuous line embodies the results achieved by the shoulder joint.

Resultant joint torques increase with joint proximity to the head, with wrist torques peaking at 9 Nm, elbow torques peaking at 21 Nm, and shoulder torques peaking at 80 Nm. The resultant torque peaks and the average resultant joint torques in the right wrist, elbow and shoulder are presented, and compared with the literature (Harrison et al. 2014), in Table 6-3:

Table 6-3: Comparison between the average and peak magnitudes of resultant joint torques of the wrist, elbow and shoulder obtained in the current work versus the results from Harrison et al. (2014).

	Average Resultant Torque (Nm)		**Peak Resultant Torque** (Nm)	
	Current model	Harrison et al. (2014)	Current model	Harrison et al. (2014)
Wrist	1.4	5	9	17
Elbow	3.9	21	21	85
Shoulder	17.4	43	80	176

(a)

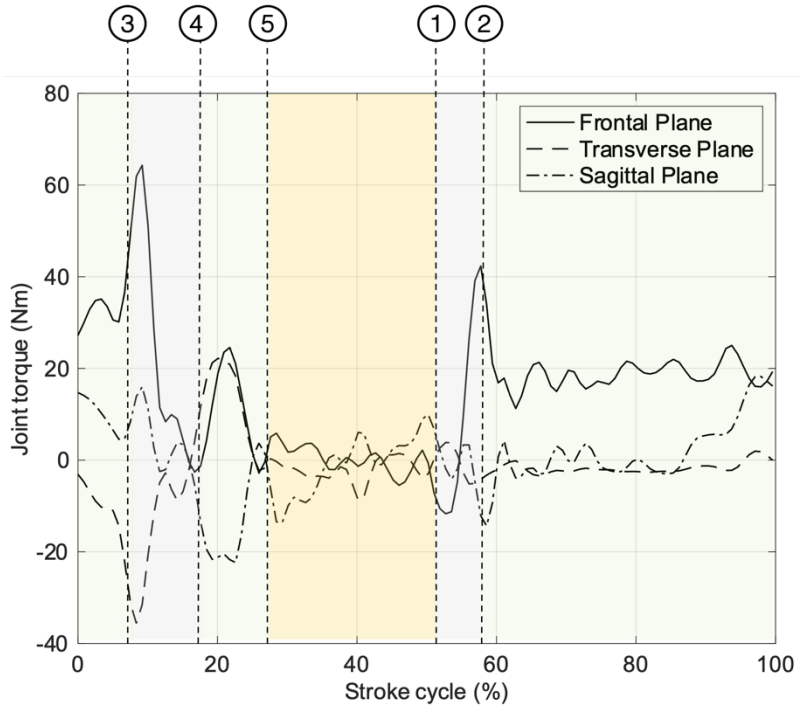

(b)

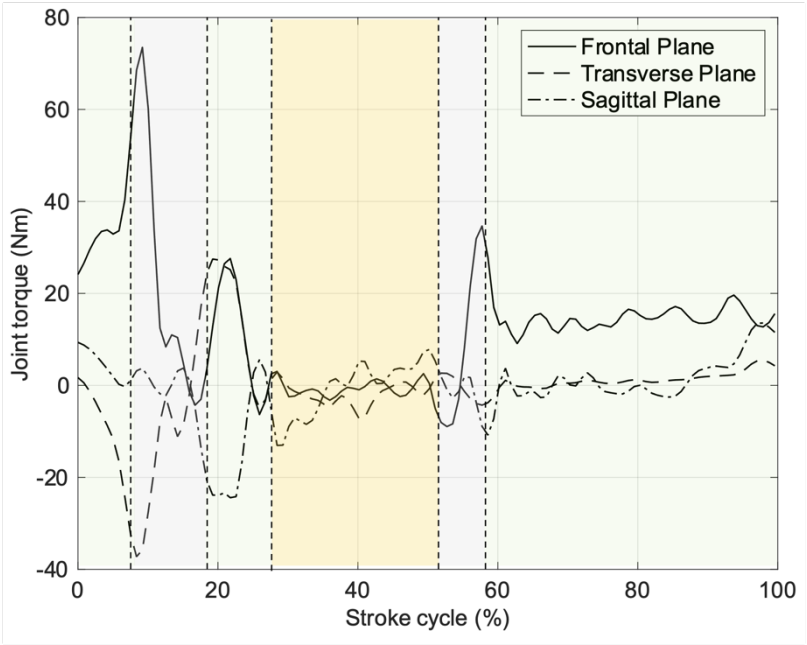

Figure 6-10: Joint torques obtained during left-hand six-beat front crawl swimming stroke cycle in the right a) sternoclavicular b) acromioclavicular.

Figure 6-10 portrays the joint torques obtained during a left-hand six-beat front crawl swimming stroke cycle in the right sternoclavicular and acromioclavicular joints. Some remarks should be made regarding the simulation of the shoulder rhythm, described as the coordinated action of the GH, SC, AC. The presence of two new articulations induces a different shoulder kinematics, with the shoulder behaviour

being directly determined by the combined action of the shoulder open chain. Consequently, a new internal force distribution acting on the shoulder might be generated due to the new force equilibrium, which ultimately would induce a different joint torque distribution, when compared to the classic shoulder model. However, when comparing the classic shoulder model versus the detailed shoulder model, the results do not show any relevant changes regarding the joint torques distribution. A possible explanation for this could be the fact that, although connecting different bodies, depending on the model, the centre of rotation of the glenohumeral/shoulder joint remains approximately in the same location. This situation, allied to the fact that the kinematics of the arm is kept unchanged between the two models and that the clavicle and scapula have no applied external forces, leads to similar joint torques. However, if an inverse dynamic analysis were to be performed considering a musculoskeletal model, requiring an optimization process considering a physiology-related cost function, this modelling choice probably would be critical for the estimation of physiological muscle and joint reaction forces. One of the key parameters for the estimation of muscle forces is their muscle length, which affects muscle contractile properties. Hence, a more accurate computation of muscle length leads to a better estimation of muscle forces (Quental et al., 2012).

The shoulder girdle, however, forms a closed-loop system - a chain in which every link in the system is connected to another by at least two distinct paths – formed by the SC joint, AC joint, and a pseudo-joint, known as scapulothoracic articulation, which was not considered in this work. Eventually, this limitation may have affected the computation of joint torques. Yet, the joint torques obtained for the GH, SC and AC joints are in good agreement with each other, with major efforts being identified consistently in the most propulsive phases of the front crawl swimming cycle: the downsweep (58%-100%; 0%-9%), the insweep (9%-18%) and the upsweep (18%-28%). From the last moments of the downsweep stage until the beginning of the insweep stage, the joint torques that promote the movement in the frontal plane achieve a peak of about 65 Nm in the SC joint and around 72 Nm in the AC joint, subjecting the clavicle to flexion stress. The same occurs during the upsweep stage, but with considerably less intensity, with joint torques of about 22 Nm and 24 Nm being achieved in the SC and AC joints, respectively. The scapula bone is also submitted to flexion efforts in the same stages: during the last instants of the downsweep through the beginning of the insweep, with the joint torques achieving around 72 Nm for the AC and GH joint; and during the upsweep, 24 Nm in the AC joint and in the GH joint. The joint torques profile identified for the GH and AC joints appear to have great similarities, which might be explained by the closeness of both joints, and the fact that none of them had hydrodynamic forces acting directly on them.

7. Conclusions

7.1. Contributions

This dissertation investigates the dynamics of a biomechanical swimmer model, with application to the front crawl swimming motion, focusing particularly on the role of the upper limbs. A three-dimensional model of the full human body, including the shoulder girdle is proposed and implemented using a multibody-based approach with cartesian coordinates. The mathematical model considered every anatomical segment as a rigid body and every articulation as an ideal kinematic joint. The acquired motion that drives the model was experimentally acquired in LABIOMEP for a subject performing a front crawl technique. Current experimental data acquisition techniques and limitations on the ability to develop experimental campaigns in a swimming pool prevented to address the shoulder rhythm acquisition in a water environment. To overcome this experimental difficulty, regression equations from the literature had to be implemented to obtain the shoulder kinematics as a function of the arm and trunk kinematics. The chosen methodology was the one proposed by Xu et al. (2014), which relies on the relative position of the humerus and torso to predict the clavicular and scapular orientations. This can be seen as the first contribution of the present work because, as far as it was possible to investigate, there was no complete study on front crawl swimming motion considering a full body biomechanical model that contemplates the influence of the shoulder rhythm. However, the predictive equations were utilized punctually outside the range of motion provided by the work of Xu et al. (2014), which might lead to some inconsistencies in particular arm positions.

The external forces that were applied on the swimmer's biomechanical model, i.e., the hydrodynamic forces, were estimated using Swumsuit, the simulation software developed by Nakashima et al. (2007). The interface developed by Sequeira (2021) was used to convert the results obtained after a kinematic consistency analysis into suitable inputs for Swumsuit and to convert the software's outputs into adequate kinetic data developed for the actual swimming motion, necessary for the inverse dynamic analysis. A secondary, but critical, accomplishment of the current work was the improvement of this interface by developing a robust joint motion reconstruction optimization-based procedure that fulfils a gap pinpointed by Sequeira (2021). This methodology described the relative angles between two consecutive bodies, connected by an anatomical joint, using Euler angles in a more robust and efficient way, from a computational point of view. To verify this new approach and understand its benefits, the simulation results for the hydrodynamic forces using this methodology were compared with the ones obtained in the work Sequeira (2021) and Nakashima et al. (2007) for the right foot.

The front crawl swimming stroke cycle was depicted, emphasizing the role of the upper limb. A left stroke cycle was highlighted, although it was the right upper limb that turned out to be evaluated. A comparison between the effect of having a detailed shoulder model over a classic model was made in terms of the kinematic angular evolution of the glenohumeral joint. The kinematic angles from both models have shown a good agreement in terms of angular monotony, with the detailed shoulder model presenting globally lower ranges of motion due to the compound contribution of the GH, SC and AC to the overall range of motion, depicted by the shoulder joint angle computed with the classic model.

The velocity of the hand was also assessed and compared to results found on the work of Samson et al. (2017). The first two velocity peaks correspond to the most propulsive phase of each arm, namely the push phase, which is supported by Barbosa et al. (2013). A third peak was registered in the recovery phase, where the arm is out of the water, which could be the result of fluid density differential at the air-water interface. Globally, their profiles present good agreement, but the current model showed significantly lower velocities. This is justified by the fact that Samson et al. (2017) simulated the front crawl of a sprinting swimmer, whereas the movement recorded in the LABIOMEP occurred at a slower pace.

The results of the inverse dynamic analysis are discussed for the principal articulations responsible for the motion of the human upper limbs, namely the right wrist, elbow and the shoulder complex joints: glenohumeral, sternoclavicular and acromioclavicular. All joints are thought to show agreement with the expected variation from positive to negative values during the different swimming stages. Predictably, the most propulsive stages, namely the insweep and upsweep, are responsible for the higher demanding efforts. Both the intersegmental forces, joint torques and resultant joint torques spike in these periods, which is justified by the necessity of pushing the water, overcoming drag and producing as much thrust as possible. The resultant joint torques obtained for the wrist, elbow and shoulder were compared to the findings of Harrison et al. (2014), with the profile of the resultant torques showing a similar behaviour but with half of the intensity registered for a sprinter swimmer.

For a determinate inverse dynamic analysis, the effect of having the shoulder rhythm described as the coordinated action of the GH, SC and AC joints shows little to no influence in the behaviour of the glenohumeral joint, when compared to the shoulder joint of the classic model. However, in the presence of a musculoskeletal model, the outcomes would have been highly affected. The computation of the muscular forces is highly dependent on the location of the bones, given that they wrap the bony segments, which constraints the muscular length, directly affecting the muscle's contractile properties. Nevertheless, the detailed model is a valuable contribution by providing insights on the dynamics of the shoulder girdle in the context of swimming, namely understanding the behaviour of the clavicle and the scapula during a front crawl swimming motion.

7.2. Future Work

Even though the current model shows generally consistent results, compared with the literature, during the front crawl swimming stroke, there are several aspects that limit the present work.

From the biomechanical modelling point of view, a more realistic discretization of the shoulder complex should be considered. The current model includes the glenohumeral, sternoclavicular and acromioclavicular joints, neglecting the effect of a fourth pseudo-joint, the scapulothoracic joint, which represents the sliding behaviour of the scapula over the thoracic wall. Often modelled by two holonomic constraints (Quental et al., 2012), this pseudo articulation closes an otherwise open-chain shoulder mechanism, being fundamental to establish a more realistic force equilibrium, naturally affecting the joint reaction torques or, in the case of a muscle force sharing problem, the muscle actuators.

The fact that the anthropometric information about the shoulder complex had to be scaled from the work of Quental et al. (2012), which is based on the measurements provided by Garner & Pandy (2001) and Spitzer et al. (1996), also presents a drawback. The anthropometric measurements were all subject specific (for a male swimmer with 1.80 m and 70.3 kg) and computed using the regression equations of Dumas et al. (2007a, 2007b), except the quantities related with the clavicle, scapula, GH, SC and AC joints, which were originally from a male subject with 1.80 m and 90.26 kg. In future works, a comprehensive full body model should be suggested to achieve full coherence with a scaling procedure.

The location of the joint centres of the HJC, LJC, SJC (only for the purpose of computing the arm's length and establishing the arm's body-fixed reference frame), CJC and OJC were computed using a set of predictive equations available in the literature. Although presenting good estimations overall, their choice was highly restricted by the available kinematic data. Since these quantities highly influence the intersegmental joint forces and joint moments (Hara et al., 2016), so further investigations should be conducted to find more accurate regression equations and eventually adequate the experimental protocols in order to provide the necessary information for state of the art regression models.

To address the shortcomings of the kinematic and kinetic acquisitions in water settings, an integrated approach considering shoulder rhythm predictive equations developed by Xu et al. (2014), kinematic data processing and subsequential estimation of the hydrodynamic forces using the simulation software Swumsuit (Nakashima et al., 2007), was considered. The regression equations proposed by Xu et al. (2014) do not cover the entire range of motion of the shoulder in the context of swimming, so they extrapolated the shoulder rhythm in this work. Therefore, future studies on the shoulder rhythm during swimming should be based on either adequate protocol to measure the shoulder kinematics or rely on regression equations that cover wider ranges of motion.

Finally, the computed intersegmental joint forces do not have physiological meaning and the joint reaction torques do not directly predict magnitudes of muscle forces. Future works should incorporate muscle models to calculate muscle, tendon, and actual joint reaction forces. Additionally, a musculoskeletal model of upper limb may be crucial to realistically analyse the impact of having a detailed versus a classic shoulder model during the study of not only the front crawl, but also of other techniques such as the breaststroke, butterfly and back strokes.

8. References

Andersen, J. T. (2019). *Movement Characteristics of Front Crawl Swimming at Sprint Pace and Middle-Distance Pace: Establishing Demands on the Torso Muscles*. PhD Thesis, Faculty of Health Sciences, University of Sydney.

Andersen, M. S., Damsgaard, M., & Rasmussen, J. (2009). Kinematic analysis of over-determinate biomechanical systems. *Computer Methods in Biomechanics and Biomedical Engineering*, *12*(4), 371–384. https://doi.org/10.1080/10255840802459412

Barbosa, T. M., Marinho, D. A., Costa, M. J., & Silva, A. J. (2011). Biomechanics of Competitive Swimming Strokes. In V. Klika (Ed.), *Biomechanics in Applications*. IntechOpen. https://doi.org/10.5772/19553

Bartlett, R. (2007). *Introduction to Sports Biomechanics* (2nd ed.). Routledge.

Beach, M. L., Whitney, S. L., & Dickoff-Hoffman, S. A. (1992). Relationship of shoulder flexibility, strength, and endurance to shoulder pain in competitive swimmers. *Journal of Orthopaedic and Sports Physical Therapy*, *16*(6), 262–268. https://doi.org/10.2519/jospt.1992.16.6.262

Bixler, B., & Riewald, S. (2002). Analysis of a swimmer's hand and arm in steady flow conditions using computational fluid dynamics. *Journal of Biomechanics*, *35*(5), 713–717. https://doi.org/10.1016/S0021-9290(01)00246-9

Brochard, S., Lempereur, M., & Rémy-Néris, O. (2011). Accuracy and reliability of three methods of recording scapular motion using reflective skin markers. *Proceedings of the Institution of Mechanical Engineers, Part H: Journal of Engineering in Medicine*, *225*(1), 100–105. https://doi.org/10.1243/09544119JEIM830

Ceccon, S., Ceseracciu, E., Sawacha, Z., Gatta, G., Cortesi, M., Cobelli, C., & Fantozzi, S. (2013). Motion analysis of front crawl swimming applying CAST technique by means of automatic tracking. *Journal of Sports Sciences*, *31*(3), 276–287. https://doi.org/10.1080/02640414.2012.729134

Charlton, I. W., & Johnson, G. R. (2006). A model for the prediction of the forces at the glenohumeral joint. *Proceedings of the Institution of Mechanical Engineers, Part H: Journal of Engineering in Medicine*, *220*(8), 801–812. https://doi.org/10.1243/09544119JEIM147

Chollet, D., Chalies, S., & Chatard, J. C. (2000). A new index of coordination for the crawl: Description and usefulness. *International Journal of Sports Medicine*, *21*(1), 54–59. https://doi.org/10.1055/s-2000-8855

Chollet, D., Delaplace, C., Tourny, C., Pelayo, P., & Sidney, M. (1997). Stroking Characteristic Variations in the 100-M Freestyle for Male Swimmers of Differing Skill. *Perceptual and Motor Skills*, *85*(5), 167–177. https://doi.org/10.2466/pms.85.5.167-177

Cleary, P. W., Cohen, R. C. Z., Harrison, S. M., Sinnott, M. D., Prakash, M., & Mead, S. (2013). Prediction of industrial, biophysical and extreme geophysical flows using particle methods. *Engineering Computations (Swansea, Wales)*, *30*(2), 157–196.

https://doi.org/10.1108/02644401311304845

Cohen, R. C. Z., Cleary, P. W., & Mason, B. R. (2009). Simulations of human swimming using Smoothed Particle Hydrodynamics. *7th International Conference on CFD in the Minerals and Process Industries*.

Cohen, R. C.Z., Cleary, P. W., & Mason, B. (2010). Improving understanding of human swimming using smoothed particle hydrodynamics. *IFMBE Proceedings*, *31 IFMBE*, 174–177. https://doi.org/10.1007/978-3-642-14515-5_45

Cohen, Raymond C.Z., Cleary, P. W., Mason, B. R., & Pease, D. L. (2015). The Role of the Hand during Freestyle Swimming. *Journal of Biomechanical Engineering*, *137*(11). https://doi.org/10.1115/1.4031586

Cohen, Raymond C.Z., Cleary, P. W., Mason, B. R., & Pease, D. L. (2020). Studying the effects of asymmetry on freestyle swimming using smoothed particle hydrodynamics. *Computer Methods in Biomechanics and Biomedical Engineering*, *23*(7), 271–284. https://doi.org/10.1080/10255842.2020.1718663

Crenna, F., Rossi, G. B., & Berardengo, M. (2021). *Filtering Biomechanical Signals in Movement Analysis*.

Davies, G. J., Matheson, J. W., Ellenbecker, T. S., & Manske, R. (2009). The Shoulder in Swimming. In *The Athlete's Shoulder* (Second Edi, Issue January). Elsevier Inc. https://doi.org/10.1016/B978-044306701-3.50039-6

De Groot, J. H., & Brand, R. (2001). A three-dimensional regression model of the shoulder rhythm. *Clinical Biomechanics*, *16*(9), 735–743. https://doi.org/10.1016/S0268-0033(01)00065-1

Dempster, W. T. (1965). Mechanisms of shoulder movement. *Archives of Physical Medicine and Rehabilitation*, *46*, 49–70.

Derrick, T. R., van den Bogert, A. J., Cereatti, A., Dumas, R., Fantozzi, S., & Leardini, A. (2020). ISB recommendations on the reporting of intersegmental forces and moments during human motion analysis. *Journal of Biomechanics*, *99*(November), 109533. https://doi.org/10.1016/j.jbiomech.2019.109533

Deschodt, V. J., Rouard, A. H., & Monteil, K. M. (1996). Relationships between the three coordinates of the upper limb joints with swimming velocity. *Biomechanics and Medicine in Swimming*, *VII*, 52–58.

Dumas, R., Chèze, L., & Verriest, J. P. (2007a). Adjustments to McConville et al. and Young et al. body segment inertial parameters. *Journal of Biomechanics*, *40*(3), 543–553. https://doi.org/10.1016/j.jbiomech.2006.02.013

Dumas, R., Chèze, L., & Verriest, J. P. (2007b). Adjustments to McConville et al. and Young et al. body segment inertial parameters. *Journal of Biomechanics*, *40*(3), 543–553. https://doi.org/10.1016/j.jbiomech.2006.02.013

Dvir, Z., & Berme, N. (1978). The shoulder complex in elevation of the arm: A mechanism approach. *Journal of Biomechanics*, *11*(5), 219–225. https://doi.org/10.1016/0021-9290(78)90047-7

Engin, A. E., & Chen, S. M. (1986a). Statistical Data Base for the Biomechanicai Properties of the Human Shoulder Complex—I: Kinematics of the Shoulder Complex. *Journal of Biomechanical Engineering*, *108*, 215–221.

Engin, A. E., & Chen, S. M. (1986b). Statistical Data Base for the Biomechanical Properties of the Human Shoulder Complex II: Passive Resistive Properties beyond the Shoulder Complex Sinus. *Journal of Biomechanical Engineering*, *108*(3), 222–227. https://doi.org/10.1115/1.3138606

Engin, A. E., & Tümer, S. T. (1989). Three-dimensional kinematic modelling of the human shoulder complex-part I: Physical model and determination of joint sinus cones. *Journal of Biomechanical Engineering*, *111*(2), 107–112. https://doi.org/10.1115/1.3168351

Garner, B. A., & Pandy, M. G. (2001). Musculoskeletal model of the upper limb based on the visible human male dataset. *Computer Methods in Biomechanics and Biomedical Engineering*, *4*(2), 93–126. https://doi.org/10.1080/10255840008908000

Gonjo, T., McCabe, C., Coleman, S., & Sanders, R. H. (2016). Magnitude of Maximum Shoulder and Hip Roll Angles in Back Crawl At Different Swimming Speeds. *34th International Conference on Biomechanics in Sports*, *August*, 605–608. http://uir.ulster.ac.uk/35774/

Gray, H., & Lewis, W. H. (1918). *Anatomy of the Human Body* (20th ed.). Lea & Febiger.

Grewal, T. J., & Dickerson, C. R. (2013). A novel three-dimensional shoulder rhythm definition that includes overhead and axially rotated humeral postures. *Journal of Biomechanics*, *46*(3), 608–611. https://doi.org/10.1016/j.jbiomech.2012.09.028

Guignard, B., Chollet, D., Vedova, D. D., Rouard, A., Bonifazi, M., Hart, J., & Seifert, L. (2019). Upper to lower limb coordination dynamics in swimming depending on swimming speed and aquatic environment manipulations. *Motor Control*, *23*(3), 418–442. https://doi.org/10.1123/mc.2018-0026

Hamill, J., & Knutzen, K. M. (2013). Biomechanical Basis of Human Movement. In *Lippincott Wiliams & Wilkins* (Vol. 53).

Hara, R., McGinley, J., Briggs, C., Baker, R., & Sangeux, M. (2016). Predicting the location of the hip joint centres, impact of age group and sex. *Scientific Reports*, *6*(November). https://doi.org/10.1038/srep37707

Harrison, S. M., Cohen, R. C. Z., Cleary, P. W., Mason, B. R., & Pease, D. L. (2014). Torque and power about the joints of the arm during the freestyle stroke. *12th International Symposium on Biomechanics and Medicine in Swimming*, *January*, 349–355.

Heinlein, S. A., & Cosgarea, A. J. (2010). Biomechanical considerations in the competitive swimmer's shoulder. *Sports Health*, *2*(6), 519–525. https://doi.org/10.1177/1941738110377611

Helm, Frans C T Van Der. (1997). A three-dimensional model of the shoulder and elbow . *Proceedings of the First Conference of the ISG*, 65–70. https://doi.org/99.1997/helm.shouldergroup

Högfors, C., Peterson, B., Sigholm, G., & Herberts, P. (1991). Biomechanical model of the human shoulder joint-II. The shoulder rhythm. *Journal of Biomechanics*, *24*(8), 699–709. https://doi.org/10.1016/0021-9290(91)90334-J

Högfors, C., Sigholm, G., & Herberts, P. (1987). Biomechanical model of the human shoulder-I. Elements. *Journal of Biomechanics*, *20*(2), 157–166. https://doi.org/10.1016/0021-9290(87)90307-1

Holzbaur, K. R. S., Murray, W. M., & Delp, S. L. (2005). A model of the upper extremity for simulating musculoskeletal surgery and analyzing neuromuscular control. *Annals of Biomedical Engineering*, *33*(6), 829–840. https://doi.org/10.1007/s10439-005-3320-7

Honda, K., Keys, M., Lyttle, A., Alderson, J., Bennamoun, M., & El-sallam, A. (2012). Freestyle swimming: an insight into propulsive and resistive mechanisms. *30th Annual Conference on Biomechanics in Sports*, *July*, 96–99.

Isler, K. (2005). 3D-kinematics of vertical climbing in hominoids. *American Journal of Physical Anthropology*, *126*(1), 66–81. https://doi.org/10.1002/ajpa.10419

Keys, M. (2010a). Establishing computational fluid dynamics models for swimming technique. In *School of Sports Science, Exercise and Health: Vol. PhD* (Issue April).

Keys, M. (2010b). *Establishing computational fluid dynamics models for swimming technique assessment*. PhD Thesis, School of Civil and Resource Engineering/School of Sports Science, Exercise and Health, The University of Western Australia.

Klein Horsman, M. D., Koopman, H. F. J. M., van der Helm, F. C. T., Prosé, L. P., & Veeger, H. E. J. (2007). Morphological muscle and joint parameters for musculoskeletal modelling of the lower extremity. *Clinical Biomechanics*, *22*(2), 239–247. https://doi.org/10.1016/j.clinbiomech.2006.10.003

Klein Horsman, Martijn D. (2007). The Twente Lower Extremity Model. In *PhD Thesis: Vol. Ph.D.* https://ris.utwente.nl/ws/portalfiles/portal/6069748%0Ahttp://doc.utwente.nl/58231/1/thesis__Klein_Horsman.pdf

Kwon, Y. H., & Casebolt, J. B. (2006). Effects of light refraction on the accuracy of camera calibration and reconstruction in underwater motion analysis. *Sports Biomechanics*, *5*(2), 315–340. https://doi.org/10.1080/14763140608522881

Laananen, D. H. (1991). *Computer Simulation of an Aircraft Seat and Occupant(s) in a Crash Environment - Program SOM-LA/SOM-TA User Manual*. 229. http://oai.dtic.mil/oai/oai?verb=getRecord&metadataPrefix=html&identifier=ADA240283%5Cnhttp://www.dtic.mil/cgi-bin/GetTRDoc?Location=U2&doc=GetTRDoc.pdf&AD=ADA240283%5Cnhttp://www.dtic.mil/dtic/tr/fulltext/u2/a240283.pdf

Lauer, J., Rouard, A. H., & Vilas-Boas, J. P. (2016). Upper limb joint forces and moments during underwater cyclical movements. *Journal of Biomechanics*, *49*(14), 3355–3361.

https://doi.org/10.1016/j.jbiomech.2016.08.027

Lauer, Jessy, Rouard, A. H., & Vilas-Boas, J. P. (2016). Upper limb joint forces and moments during underwater cyclical movements. *Journal of Biomechanics*, *49*(14), 3355–3361. https://doi.org/10.1016/j.jbiomech.2016.08.027

Lindsay, N. (2001). *Modelling of the Shoulder Mechanism: A Report Describing the Development of a Three- dimensional Biomechanical Model of the Human Shoulder Complex*. https://doi.org/10.1016/0021-9290(89)90441-7

Lippert, L. S. (2006). *Clinical Kinesiology and Anatomy* (4th ed.). F. A. Davis Company.

Maglischo, E. (2003). Swimming fastest. The essential reference on technique, training, and program design. *Hum. Kinet.*, 593–688.

Maglischo, E. W., Maglischo, C. W., & Santos, T. R. (1989). Patterns Of Forward Velocity in the Four Competitive Swimming Strokes. *Coaching and Sports Activities*.

Marinho, D. A., Silva, A. J., Reis, V. M., Barbosa, T. M., Vilas-Boas, J. P., Alves, F. B., Machado, L., & Rouboa, A. I. (2011). Three-dimensional CFD analysis of the hand and forearm in swimming. *Journal of Applied Biomechanics*, *27*(1), 74–80. https://doi.org/10.1123/jab.27.1.74

Matzkin, E., Suslavich, K., & Wes, D. (2016). Swimmer's shoulder: Painful shoulder in the competitive swimmer. *Journal of the American Academy of Orthopaedic Surgeons*, *24*(8), 527–536. https://doi.org/10.5435/JAAOS-D-15-00313

McConville, J. T., Churchill, T. D., Kaleps, I., Clauser, C. E., & Cuzzi, J. (1980). Anthropometric Relationships of Body and Body Segments Moments of Inertia. In *AFAMRL-TR-80-119, Aerospace Medical Research Laboratory* (Vol. 105, Issue 21). https://doi.org/10.1073/pnas.0710346105

Monnet, T., Samson, M., Bernard, A., David, L., & Lacouture, P. (2014). Measurement of three-dimensional hand kinematics during swimming with a motion capture system: A feasibility study. *Sports Engineering*, *17*(3), 171–181. https://doi.org/10.1007/s12283-014-0152-4

Moore, K. L., Dalley, A. F., & Agur, A. M. R. (2010). *Clinically Oriented Anatomy* (6th ed.). Lippincott Williams & Wilkins.

Murphy, A. J., Bull, A. M. J., & McGregor, A. H. (2011). Predicting the lumbosacral joint centre location from palpable anatomical landmarks. *Proceedings of the Institution of Mechanical Engineers, Part H: Journal of Engineering in Medicine*, *225*(11), 1078–1083. https://doi.org/10.1177/0954411911416859

Nakashima, M., Satou, K., & Miura, Y. (2007). Development of Swimming Human Simulation Model Considering Rigid Body Dynamics and Unsteady Fluid Force for Whole Body. *Journal of Fluid Science and Technology*, *2*(1), 56–67. https://doi.org/10.1299/jfst.2.56

Nakashima, Motomu, Maeda, S., Miwa, T., & Ichikawa, H. (2012). Optimizing simulation of the arm stroke in crawl swimming considering muscle strength characteristics of athlete swimmers. *Journal of Biomechanical Science and Engineering*, *7*(2), 102–117. https://doi.org/10.1299/jbse.7.102

Nakashima, Motomu, Satou, K., & Miura, Y. (2007). Development of Swimming Human Simulation Model Considering Rigid Body Dynamics and Unsteady Fluid Force for Whole Body. *Journal of Fluid Science and Technology*, *2*(1), 56–67. https://doi.org/10.1299/jfst.2.56

Nikravesh, P. E. (1988). *Computer Aided Analysis of Mechanical Systems*.

Nordin, M., & Frankel, V. H. (2013). *Basic Biomechanics of the Musculoskeletal System*.

Oliveira, H. (2016). *Inverse Dynamic Analysis of the Human Locomotion Apparatus for Gait Helder Jorge Carrapatoso Oliveira Thesis to obtain the Master of Science Degree in Mechanical Engineering Supervisors : Prof . Carlos Miguel Fernandes Quental Prof . João Orlando Marques* (Issue November).

Otten, E. (2003). Inverse and forward dynamics: Models of multibody systems. *Philosophical Transactions of the Royal Society B*, *358*(1437), 1493–1500. https://doi.org/10.1098/rstb.2003.1354

Palastanga, N., & Soames, R. (2012). *Anatomy and Human Movement - Structure and Function* (6th ed.). Churchill Livingstone.

Pàmies-Vilà, R. (2012). *Application of Multibody Dynamics Techniques to the Analysis of Human Gait*.

Peat, M. (1986). Functional anatomy of the shoulder complex. *Journal of Orthopaedic and Sports Physical Therapy*, *66*(12), 1855–1865. https://doi.org/10.2519/jospt.1993.18.1.342

Peng, J., Panda, J., Van Sint Jan, S., & Wang, X. (2015). Methods for determining hip and lumbosacral joint centers in a seated position from external anatomical landmarks. *Journal of Biomechanics*, *48*(2), 396–400. https://doi.org/10.1016/j.jbiomech.2014.11.040

Pink, M. M., & Tibone, J. E. (2000). The painful shoulder in the throwing athlete. *Orthopedic Clinics of North America*, *31*(2), 247–261.

Psycharakis, S. G., & Sanders, R. H. (2008). Shoulder and hip roll changes during 200-m front crawl swimming. *Medicine and Science in Sports and Exercise*, *40*(12), 2129–2136. https://doi.org/10.1249/MSS.0b013e31818160bc

Quental, C. (2013a). *Biomechanical Tools for the Analysis of the Native and Prosthetic Shoulders*. 1–310.

Quental, C. (2013b). *Biomechanical Tools for the Analysis of the Native and Prosthetic Shoulders*.

Quental, C., Folgado, J., Ambrósio, J., & Monteiro, J. (2012). A multibody biomechanical model of the upper limb including the shoulder girdle. *Multibody System Dynamics*, *28*(1–2), 83–108. https://doi.org/10.1007/s11044-011-9297-0

Rajagopal, A., Dembia, C. L., DeMers, M. S., Delp, D. D., Hicks, J. L., & Delp, S. L. (2016). Full-Body Musculoskeletal Model for Muscle-Driven Simulation of Human Gait. *IEEE Transactions on Biomedical Engineering*, *63*(10), 2068–2079. https://doi.org/10.1109/TBME.2016.2586891

Reed, M. P., Manary, M. A., & Schneider, L. W. (1999). Methods for measuring and representing

automobile occupant posture. *SAE Technical Papers*, *724*. https://doi.org/10.4271/1999-01-0959

Rejman, M., Tyc, Ł., Kociuba, M., Bornikowska, A., Rudnik, D., & Kozieł, S. (2018). Anthropometric predispositions for swimming from the perspective of biomechanics. *Acta of Bioengineering and Biomechanics*, *20*(4), 151–159. https://doi.org/10.5277/ABB-01254-2018-03

Richardson, A. B., Jobe, F. W., & Collins, H. R. (1980). The shoulder in competitive swimming. *The American Journal of Sports Medicine*, *8*(3), 159–163. https://doi.org/10.1177/036354658000800303

Richardson, A. R. (1986). The Biomechanics of Swimming: The Shoulder and Knee. *Clinics in Sports Medicine*, *5*(1), 103–113. https://doi.org/https://doi.org/10.1016/S0278-5919(20)31162-5

Samson, M., Bernard, A., Monnet, T., Lacouture, P., & David, L. (2017). Unsteady computational fluid dynamics in front crawl swimming. *Computer Methods in Biomechanics and Biomedical Engineering*, *20*(7), 783–793. https://doi.org/10.1080/10255842.2017.1302434

Sanders, R. H., & Psycharakis, S. G. (2009). Rolling rhythms in front crawl swimming with six-beat kick. *Journal of Biomechanics*, *42*(3), 273–279. https://doi.org/10.1016/j.jbiomech.2008.10.037

Sato, Y., & Hino, T. (2013). A computational fluid dynamics analysis of hydrodynamic force acting on a swimmer's hand in a swimming competition. *Journal of Sports Science and Medicine*, *12*(4), 679–689.

Scott, S. H., & Winter, D. A. (1990). Internal forces at chronic running injury sites. *Medicine and Science in Sports and Exercise*, *22*(3), 357–369. http://www.ncbi.nlm.nih.gov/pubmed/2381304

Sequeira, M. (2021). *Inverse Dynamics of a Swimmer Multibody Model : An Analysis of the Lower Limbs During Front Crawl* (Issue January). University of Lisbon.

Serenza, F. S., Oliveira, A. S., Bedo, B. L. S., Mariano, F. P., Aquino, R., Warner, M., & Santiago, P. R. P. (2018). Biomechanical analysis of the shoulder of swimmers after a maximal effort test. *Physical Therapy in Sport*, *30*(March), 14–21. https://doi.org/10.1016/j.ptsp.2017.11.002

Seth, A., Dong, M., Matias, R., & Delp, S. (2019). Muscle contributions to upper-extremity movement and work from a musculoskeletal model of the human shoulder. *Frontiers in Neurorobotics*, *13*(November), 1–9. https://doi.org/10.3389/fnbot.2019.00090

Silva, Miguel Tavares da. (2003). *Human Motion Analysis Using Multibody Dynamics and Optimization Tools*. Instituto Superior Técnico - Universidade Técnica de Lisboa.

Silva, M. P.T., & Ambrósio, J. A. C. (2002). Kinematic data consistency in the inverse dynamic analysis of biomechanical systems. *Multibody System Dynamics*, *8*(2), 219–239. https://doi.org/10.1023/A:1019545530737

Silva, Miguel P.T., & Ambrósio, J. A. C. (2003). Solution of Redundant Muscle Forces in Human Locomotion with Multibody Dynamics and Optimization Tools. *Mechanics Based Design of Structures and Machines*, *31*(3), 381–411. https://doi.org/10.1081/SME-120022856

Silva, Miguel T. (2005). Advances in Computational Multibody Systems. In *Advances in Computational*

Multibody Systems (Issue January 2005). https://doi.org/10.1007/1-4020-3393-1

Silver, N. (2012). Which Records Get Shattered? *The New York Times*.

Snell, R. S. (2012). *Clinical Anatomy by Regions* (9th ed.). Lippincott Williams & Wilkins.

Spitzer, V., Ackerman, M. J., Scherzinger, A. L., & Whitlock, D. (1996). The Visible Human Male: A Technical Report. *Emerging Infectious Diseases*, *3*(2), 118–130. https://doi.org/10.1136/jamia.1996.96236280

Suito, H., Tsujimoto, N., Shinkai, H., Sano, S., Nunome, H., & Ikegami, Y. (2007). The Effect of Fatigue on the Underwater Arm Stroke Motion in the 100 M Front Crawl. *Journal of Biomechanics*, *40*(December), S772. https://doi.org/10.1016/s0021-9290(07)70760-1

Takagi, H., Nakashima, M., Sato, Y., Matsuuchi, K., & Sanders, R. H. (2016). Numerical and experimental investigations of human swimming motions. *Journal of Sports Sciences*, *34*(16), 1564–1580. https://doi.org/10.1080/02640414.2015.1123284

Tanghuizi, D., & Toshimasa, Y. (2016). Three-dimensional motion of shoulder complex during front crawl swimming. *International Conference on Biomechanics in Sports*.

Terrier, A., Aeberhard, M., Michellod, Y., Mullhaupt, P., Gillet, D., Farron, A., & Pioletti, D. P. (2010). A musculoskeletal shoulder model based on pseudo-inverse and null-space optimization. *Medical Engineering and Physics*, *32*(9), 1050–1056. https://doi.org/10.1016/j.medengphy.2010.07.006

Thielbar, J. A. (2020). *Effect of Sport-Specific Demands on Swimmer ' S Shoulder*.

Toussaint, H. M., & Beek, P. J. (1992). Biomechanics of Competitive Front Crawl Swimming. *Sports Medicine: An International Journal of Applied Medicine and Science in Sport and Exercise*, *13*(1), 8–24. https://doi.org/10.2165/00007256-199213010-00002

Toussaint, H. M., Carol, A., Kranenborg, H., & Truijens, M. J. (2006). Effect of fatigue on stroking characteristics in an arms-only 100-m front-crawl race. *Medicine and Science in Sports and Exercise*, *38*(9), 1635–1642. https://doi.org/10.1249/01.mss.0000230209.53333.31

Tovin, B. J. (2006). The prevention and treatment of swimmer's shoulder. *North American Journal of Sports Physical Therapy*, *1*(4), 166–175.

Troup, J. P. (1999). The physiology and biomechanics of competitive swimming. *Clinics in Sports Medicine*, *18*(2), 267–285. https://doi.org/10.1016/S0278-5919(05)70143-5

van Andel, C., van Hutten, K., Eversdijk, M., Veeger, D. J., & Harlaar, J. (2009). Recording scapular motion using an acromion marker cluster. *Gait and Posture*, *29*(1), 123–128. https://doi.org/10.1016/j.gaitpost.2008.07.012

van der Helm, F. C.T. (1994). A finite element musculoskeletal model of the shoulder mechanism. *Journal of Biomechanics*, *27*(5). https://doi.org/10.1016/0021-9290(94)90065-5

van der Helm, Frank C.T., & Pronk, G. M. (1995). Three-Dimensional Recording and Description of Motions of the Shoulder Mechanism. *Journal of Biomechanical Engineering*, *117*, 27–40.

http://biomechanical.asmedigitalcollection.asme.org/

Veeger, H. E. J., & van der Helm, F. C. T. (2007). Shoulder function: The perfect compromise between mobility and stability. *Journal of Biomechanics*, *40*(10), 2119–2129. https://doi.org/10.1016/j.jbiomech.2006.10.016

Von Loebbecke, A., Mittal, R., Mark, R., & Hahn, J. (2009). A computational method for analysis of underwater dolphin kick hydrodynamics in human swimming. *Sports Biomechanics*, *8*(1), 60–77. https://doi.org/10.1080/14763140802629982

Weldon, E. J., & Richardson, A. B. (2001). Upper extremity overuse injuries in swimming: A discussion of swimmer's shoulder. *Clinics in Sports Medicine*, *20*(3), 423–438. https://doi.org/10.1016/S0278-5919(05)70260-X

Winter, D. A. (2009a). Biomechanics and Motor Control of Human Movement: Fourth Edition. In *Biomechanics and Motor Control of Human Movement: Fourth Edition* (4th ed.). https://doi.org/10.1002/9780470549148

Winter, D. A. (2009b). *Biomechanics and Motor Control of Human Movement* (Fourth Edi). John Wiley & Sons, Inc. Hoboken, New Jersey. https://doi.org/10.1002/9780470549148

Wu, G., Siegler, S., Allard, P., Kirtley, C., Leardini, A., Rosenbaum, D., Whittle, M., D'Lima, D., Christofolini, L., Witte, H., Schmid, O., & Stokes, I. (2002). ISB recommendation on definitions of joint coordinate system of various joints for the reporting of human joint motion—part I: ankle, hip, and spine. *Journal of Biomechanics*, *35*(2), 543–548.

Wu, G., Van Der Helm, F. C. T., Veeger, H. E. J., Makhsous, M., Van Roy, P., Anglin, C., Nagels, J., Karduna, A. R., McQuade, K., Wang, X., Werner, F. W., & Buchholz, B. (2005). ISB recommendation on definitions of joint coordinate systems of various joints for the reporting of human joint motion - Part II: Shoulder, elbow, wrist and hand. *Journal of Biomechanics*, *38*(5), 981–992. https://doi.org/10.1016/j.jbiomech.2004.05.042

Xiao, T., & Fu, Y. F. (2016). Biomechanical Modeling of Human Body Movement. *Journal of Biometrics & Biostatistics*, *7*(3), 5–8. https://doi.org/10.4172/2155-6180.1000309

Xu, X., Lin, J. hua, & McGorry, R. W. (2014). A regression-based 3-D shoulder rhythm. *Journal of Biomechanics*, *47*(5), 1206–1210. https://doi.org/10.1016/j.jbiomech.2014.01.043

Yang, J., Feng, X., Kim, J. H., & Rajulu, S. (2010). Review of biomechanical models for human shoulder complex. *International Journal of Human Factors Modelling and Simulation*, *1*(3), 271. https://doi.org/10.1504/ijhfms.2010.036791

Appendix A: Marker Setup Protocol

The full body anatomical markers setup protocol for swimming applications in the Porto Biomechanics Laboratory (LABIOMEP-UP) is listed in Table A-0-1 and illustrated in **Error! Reference source not found.**. These markers were placed on palpable bony landmarks. Of all the 66 markers enumerated here, only 38 were used on the course of this work.

Table A-0-1: Markers description and location on the subject's skin. The column labelled as "Used" identifies whether the marker was used to define the biomechanical model or not.

ID	Marker Name	Location	Used
1	C7	7th Cervical Vertebrae	✓
2	HEADFRONT	Forehead, above the nose	✓
3	HEADTOP	On the top of the head, vertically above the ears	✓
4	LAC	Left acromial edge of the scapula	✓
5	LASIS	Left Anterior Superior Iliac Spine	✓
6	LBACK	Left mid-distance between the scapula and pelvis	✗
7	LCA	Distal end of the posterior aspect of the left Calcaneus. Should be vertically aligned with LFM2	✓
8	LFA1	Left forearm cluster marker 1	✗
9	LFA2	Left forearm cluster marker 2	✗
10	LFA3	Left forearm cluster marker 3	✗
11	LFM1	Lateral aspect of the 1st metatarsal head of the left foot	✓
12	LFM2	Dorsal aspect of the 2nd metatarsal head of the left foot. Calcaneus marker should be vertically aligned	✗
13	LFM5	Lateral aspect of the 5th metatarsal head of the left foot	✓
14	LHEAD	Above the left ear centre	✓
15	LLA	Prominence of the left lateral Malleolus	✓
16	LLELB	Lateral Epicondyle of the Left Humerus	✓
17	LLH	Lateral portion of the 2nd metatarsal head of the left hand	✓
18	LLK	Lateral Epicondyle of the Left Femur	✓
19	LMA	Prominence of the left medial Malleolus	✓
20	LMELB	Medial Epicondyle of the Left Humerus	✓
21	LMH	Medial portion of the 5th metatarsal head of the left hand	✓
22	LMK	Lateral Epicondyle of the Left Femur	✓

23	LPSIS	Left Posterior Superior Iliac Spine	✓
24	LRAD	Left Radio-Styloid Process	✓
25	LSHIN	In front of the left shin	✗
26	LSHOULDERBACK	Over the left scapula	✗
27	LSK1	Left shank cluster marker 1	✗
28	LSK2	Left shank cluster marker 2	✗
29	LSK3	Left shank cluster marker 3	✗
30	LTH1	On the left thigh, above the kneecap	✗
31	LTROC	Left Trochanter	✗
32	LUA1	Laterally on the left arm, between the biceps and the triceps	✗
33	LULN	Left Ulna-Styloid Process	✓
34	RAC	Right acromial edge of the scapula	✓
35	RASIS	Right Anterior Superior Iliac Spine	✓
36	RBACK	Right mid-distance between the scapula and pelvis	✗
37	RCA	Distal end of the posterior aspect of the right Calcaneus. Should be vertically aligned with RFM2	✓
38	RFA1	Right forearm cluster marker 1	✗
39	RFA2	Right forearm cluster marker 2	✗
40	RFA3	Right forearm cluster marker 3	✗
41	RFM1	Lateral aspect of the 1st metatarsal head of the right foot	✓
42	RFM2	Dorsal aspect of the 2nd metatarsal head of the right foot. Calcaneus marker should be vertically aligned	✗
43	RFM5	Lateral aspect of the 5th metatarsal head of the right foot	✓
44	RHEAD	Above the right ear centre	✓
45	RLA	Prominence of the right lateral Malleolus	✓
46	RLELB	Lateral Epicondyle of the Right Humerus	✓
47	RLH	Lateral portion of the 2nd metatarsal head of the right hand	✓
48	RLK	Lateral Epicondyle of the Right Femur	✓
49	RMA	Prominence of the right medial Malleolus	✓
50	RMELB	Medial Epicondyle of the Right Humerus	✓

51	RMH	Lateral portion of the 5th metatarsal head of the right hand	✓
52	RMK	Medial Epicondyle of the Right Femur	✓
53	RPSIS	Right Posterior Superior Iliac Spine	✓
54	RRAD	Right Radio-Styloid Process	✓
55	RSHIN	In front of the right shin	✗
56	RSHOULDERBACK	Over the right scapula	✗
57	RSK1	Right shank cluster marker 1	✗
58	RSK2	Right shank cluster marker 2	✗
59	RSK3	Right shank cluster marker 3	✗
60	RTH1	On the right thigh, above the kneecap	✗
61	RTROC	Right Trochanter	✗
62	RUA1	Laterally on the right arm, between the biceps and the triceps	✗
63	RULN	Right Ulna-Styloid Process	✓
64	ST1	Sternum cluster marker 1	✓
65	ST2	Sternum cluster marker 2	✗
66	ST3	Sternum cluster marker 3	✗

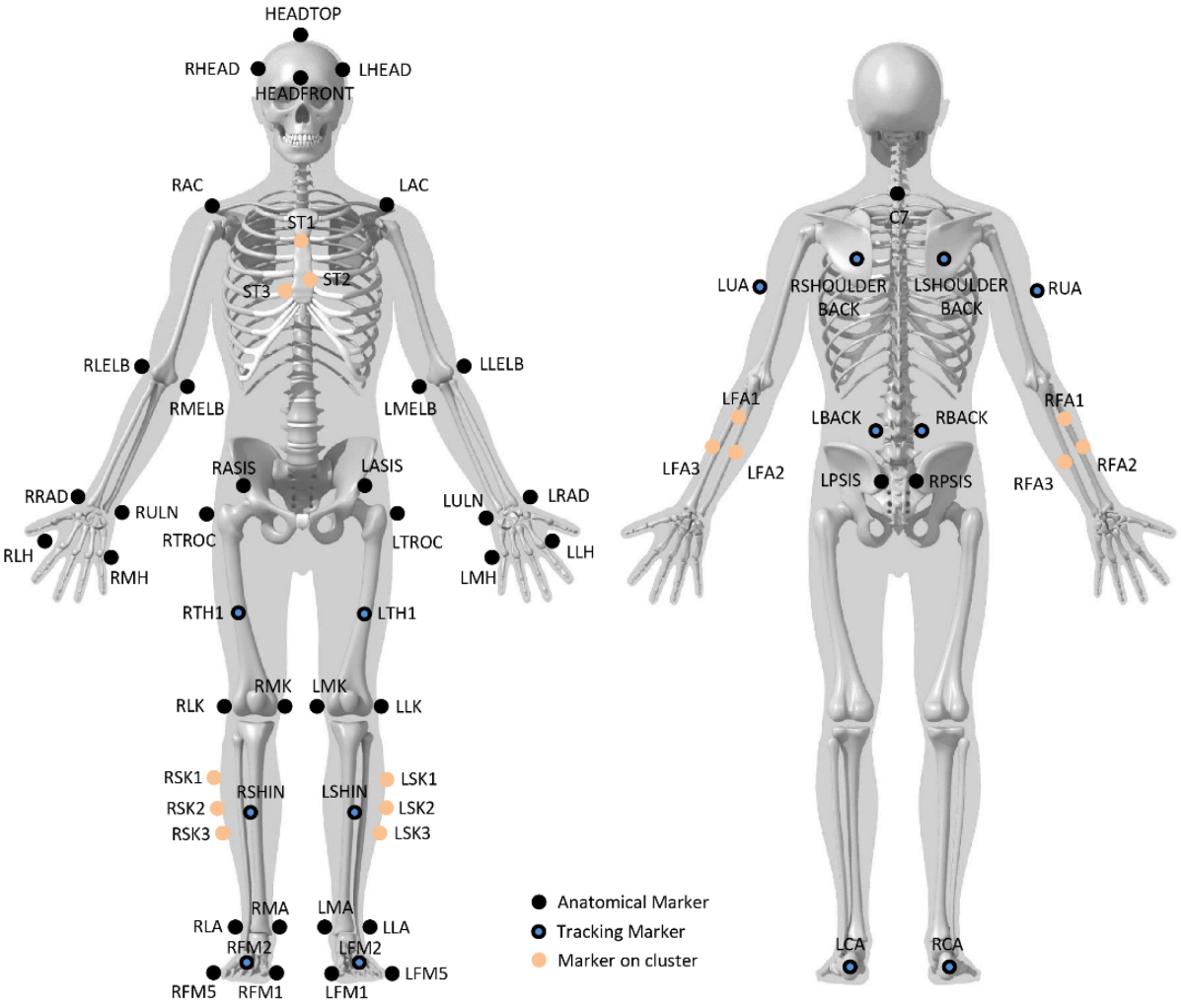

Figure A-1: Anterior and posterior view of the human skeleton. Location of the sixty-six markers placed on the subject's skin.

Appendix B: LABIOMEP Layout

The schematic of the Porto Biomechanics Laboratory (LABIOMEP-UP) layout, shown in **Figure 5-1**, is as follows.

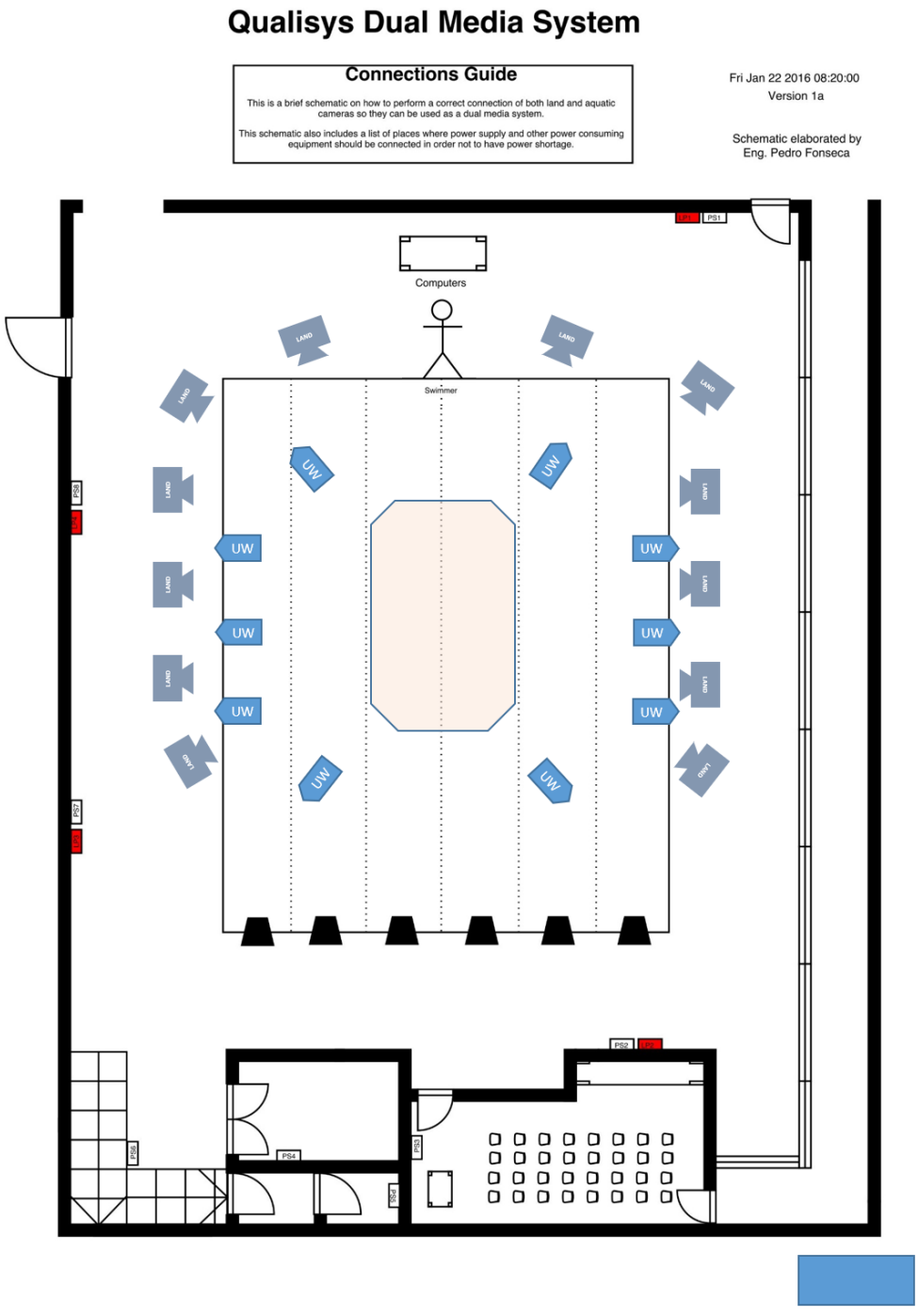

Figure B-1: Top view overall configuration of the LABIOMEP-UP layout. UW stands for underwater cameras, and LAND stands for above water cameras. The coloured rectangle in the centre of the swimming pool corresponds to the calibrated volume covered by the 22 cameras.